University of Strathclyde

Doctoral Thesis

# A Novel Titania–Silica Catalyst for Converting Methyl Lactate to Lactide towards a Circular Economy for PLA

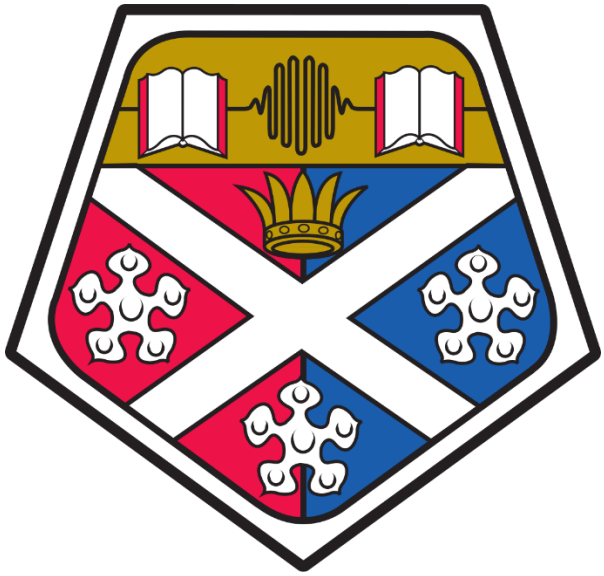


Shuya Jia

Supervisor: Dr. Xiaolei Zhang


A thesis submitted in the fulfilment of the requirements for the degree of Doctor of Philosophy in the Department of Chemical and Process Engineering

# Declaration of Authorship

This thesis is the result of the author's original research. It has been composed by the author and has not been previously submitted for examination which has led to the award of a degree.



Signed:

Shuya Jia

31/10/2025

# Abstract

In modern society, plastics have become indispensable owing to their durability, high strength, flexibility, and low production cost. Among all plastics, polylactic acid (PLA) is attractive for its biodegradable origin and favourable mechanical properties, yet the lack of efficient closed-loop recycling constrains its wider deployment. Chemical recycling of waste PLA into lactide (LD) accelerates degradation and conserves resources with its critical step is LD production from monomer methyl lactate (MLA) which is the product of PLA alcoholysis. LD production has relied on an energy-intensive one-step gas phase transesterification process, with Titania–silica catalysts identified as delivering the best performance. However, the yields remain relatively low (below 42%). Accordingly, this work focuses on developing an alternative one-step liquid-phase transesterification process of MLA to LD employing Titania–silica catalysts. This one-step LD production process was investigated from cross-material benchmarking, mechanistic understanding, experimental testing, and economic assessment aspects, and it advances a blueprint for circular PLA.

Firstly, a decision-grade dataset spanning 17 widely used polymers was compared and analysed across mechanical, thermal, chemical, and environmental metrics. The findings further confirm that PLA serves as an excellent model polymer for circular-economy studies, as it uniquely combines bio-based and biodegradable features, market relevance, strong tensile properties, and tractable recycling pathways.

A one-pot Ti-based catalytic system for the conversion of MLA to LD was experimentally investigated. It was concluded that $TiO_x/SiO_2$ outperformed anatase $TiO_2$ across 170–220 °C, reaching 62 % conversion and 49 % LD selectivity at 220 °C, whereas

anatase remained below 35 % conversion and 1 % selectivity. XPS detected ~6 % Ti(III) and STEM-EDS confirmed atomic dispersion. This supports the conclusion that Ti(III) sites and silica support govern MLA→LD efficiency, positioning $TiO_x/SiO_2$ as the preferred catalyst. Subsequently, the complete reaction pathway for the transesterification of MLA to LD over the Titania–silica catalyst was explored, accompanied by transition state searching to identify the key intermediates and activation energies. The computed free-energy profile features a feasible barrier for dimerization ($\Delta G^{\neq}$ = 0.63 eV) and a very high ring-closure barrier to LD ($\Delta G^{\neq}$ = 1.82 eV), identifying cyclisation as the rate-limiting step and predicting release of two methanol equivalents.

Based on the findings from the experiment work, the catalyst-support performance was further evaluated by investigating MLA adsorption on various catalyst surfaces adopting Density Functional Theory (DFT) modelling. The influence of catalyst metal valence states and support on the reaction was explored. It has been found that Ti(III)–O–Si sites on silica maximize MLA binding (adsorption energy around −1.69 eV) via synergistic hydrogen bonding, Ti–O σ-bonding, and π-backbonding, whereas $TiO_2$-based sites suffer electron leakage into subsurface layers and weaker adsorption (−0.77 eV).

Finally, three feasible PLA recycling routes were evaluated at plant-scale using Techno-economic Analysis (TEA) in Aspen Plus. An optimized pathway leveraging $TiO_2/SiO_2$ catalysis increased annual PLA output from $5.96 \times 10^4$ to $9.04 \times 10^4$ tonne per year (+59.87 %) while reducing production cost by 22.87 % to US $ 1773 per tonne. Sensitivity analysis identified catalyst loading, feed rate, and raw-material prices as dominant cost drivers.

Overall, this work provides a sustainable and economically viable solution for recycling waste PLA, aligning with growing demand of the plastics industry for environmentally friendly alternatives. The findings are crucial for advancing a circular plastics economy and highlight the importance of catalyst optimization in improving the efficiency and sustainability of PLA recycling processes.

# Acknowledgements

First and foremost, I am deeply grateful to my first supervisor, Dr Xiaolei Zhang, whose guidance and steady support made this dissertation possible. Throughout my doctorate she provided clear direction, patient encouragement, and opened doors that helped me enter the academic community. I also thank my second supervisor, Dr Jun Li, whose consistent support broadened my horizons and gave me invaluable teaching experience. I am grateful to the laboratory technicians for their practical assistance throughout my research.

I was fortunate to meet many kind and inspiring people at University of Strathclyde. I am especially thankful to Stuart, Fraser and Michaela, who welcomed me to the UK and shared practical tips especially during the toughest early months. I also thank my PhD colleagues, including Khadija, Robbie and Nisha, whose friendship and conversations enriched my time. I am grateful as well to Haitian and Haizi, a dear couple who were my steadfast support in Glasgow.

Our group also worked with outstanding visiting scholars: Xincheng, Chao, Feng and Rongrong. Your help advanced my work, and it was a privilege to co-author several papers with you. To my friends Jiajun, Shuang, Yin, Xinlu, Yijing, Yimeng, Yihan, Yiran, Xinxin and Lanyu, thank you for reaching out to me time and again during my hardest moments. I would not be who I am today without you.

Finally, I owe everything to my family. To my mother, the strongest woman I know, thank you for your unwavering and unconditional support. To my uncle, the sharpest mind in our family, thank you for the guidance that has carried me to this day.

To my husband, Sitan, thank you for always standing by me. To my father and my grandfather, I believe you are watching over me and are proud. This thesis is dedicated to you both. I love you forever.

# Publications

### Papers included in thesis:

### Chapter 6:

Zhang, R.[§]; **Jia, S**. [§]; Li, J.; Xu, Y.; Chen, H.; Zhang, X*. Techno-Economic Assessment of a Closed-Loop Circular Economy for Polylactic Acid. *ACS Sustain. Chem. Eng.* 2025, *13* (29), 11226–11237. https://doi.org/10.1021/acssuschemeng.5c01154.

(For this publication, I contributed approximately 50% to this work, mainly through the development of the technical process.)

### Chapter 4 and 5:

**Jia, S**.; Zhang, X*. One-Pot Liquid-Phase Conversion of Methyl Lactate to Lactide over $TiO_x/SiO_2$ Catalysts: Experimental and DFT Studies (In preparation)

### Papers not included in this thesis:

(1) Wang, H.; Qi, H.; Sun, X.; **Jia, S.**; Li, X.; Miao, T. J.; Xiong, L.; Wang, S.; Zhang, X.; Liu, X.; Wang, A.; Zhang, T.; Huang, W.; Tang, J*. High Quantum Efficiency of Hydrogen Production from Methanol Aqueous Solution with $PtCu–TiO_2$ Photocatalysts. *Nat. Mater.* 2023, *22* (5), 619–626. https://doi.org/10.1038/s41563-023-01519-y.

(2) Cao, X. [§]; **Jia, S.** [§]; Zhang, Y.; Long, F.; Chen, Y.; Liu, P.; Zhang, X.; Xu, J. *; Jiang, J*. Synergistic Effect between Oxygen Vacancy and Brønsted Acid Sites Boosting Efficient Hydrogenolysis of Esters to Alkanes. *ACS Sustain. Chem. Eng.* 2025, acssuschemeng.5c01205. https://doi.org/10.1021/acssuschemeng.5c01205.

(For this publication, I contributed approximately 50% to this work, mainly for the DFT modelling and analysis.)

(3) Qu, Y.; Xu, G.; Chen, C.; Guo, J.; Liu, D.; Jia, H.; Guo, H.; **Jia, S**.; Jia, J.; Zhang, Y. *; Yan L*. A Guideline to Optimizing the Performance of $V_2O_5–MoO_3/TiO_2$ Catalysts for Low-Temperature SCR Denitrification in Industrial Application. *Ind. Chem. Mater.* 2025.

(4) Cao, X.; Zhao, J. *; **Jia, S.**; Long, F.; Chen, Y.; Zhang, X. *; Xu, J. *; Jiang, J*. Enhanced Ruthenium Selectivity for the Conversion of FAMEs to Diesel-Range Alkanes by Surface Decoration of $FeO_x$ Species. *Chem. Eng. J.* 2024, *481*, 148345.

(5) Cao, X.; Wu, S.; Zhao, J.; Long, F.; **Jia, S.**; Zhang, X.; Xu, J. *; Jiang, J*. Synthesis of Novel Mo-Ni@$Al_2O_3$ Catalyst for Converting Fatty Acid Esters into Diesel-Range Alkanes with Enhanced Hydrodeoxygenation Selectivity. *Appl. Catal. B Environ.* 2024, *343*, 123506. https://doi.org/10.1016/j.apcatb.2023.123506.

(6) Liu, C.; Wu, Y. *; Cai, T.; Chen, Y.; **Jia, S.**; Zhang, X.; Li, Z.; Wu, Z.; Qing, Y.; Jiang, J. *; Wang, K*. Investigation into the Effect of Solvents on Lignin Hydrogenation for the Production of Phenolic Compounds. *Green Chem.* 2024, *26* (6), 3356–3367.

(7) Long, F.; Wu, S.; Chen, H.; **Jia, S.**; Cao, X.; Liu, P.; Lu, Y.; Jiang, J.; Zhang, X. *; Xu, J*. Alcohol Production from Fatty Acids via Ni3Fe/Rutile: Revealing the Role of Oxygen Vacancy and Metal-Support Electronic Density Characteristics. *J. Catal.* 2023, *428*, 115171. https://doi.org/10.1016/j.jcat.2023.115171.

(8) Shaw, A.; Zhang, X. *; **Jia, S.**; Fu, J.; Lang, L. *; Brown, R. C. Mechanistic Investigation of Char Growth from Lignin Monomers during Biomass Utilisation. *Fuel Process. Technol.* 2023, *239*, 107556.

(9) Liu, C.; Cai, T.; Yin, X.; Liang, J.; **Jia, S.**; Zhang, X.; Xu, J.; Hu, J.; Jiang, J. *; Wang, K. * A Sustainable and Profitable Biorefinery Strategy for Efficiently Converting Lignocellulose to Furfural, Glucose and Phenolic Compounds. *Green Chem.* 2022, *24* (21), 8494–8502. https://doi.org/10.1039/D2GC03231G.

# Contents

# List of Figures

# List of Tables

# List of Abbreviation

| Abbreviation | Definition | Abbreviation | Definition |
|---|---|---|---|
| **AE** | all-electron | **BET** | Brunauer–Emmett–Teller |
| **BJH** | Barrett–Joyner–Halenda | **BO** | Born–Oppenheimer |
| **CA** | cellulose acetate | **CBM** | conduction band minimum |
| **CDD** | charge density difference | **CG** | conjugate gradient |
| **CI-NEB** | climbing-image nudged elastic band | **DBU** | 1,8-diazabicyclo[5.4.0]undec-7-ene |
| **DC** | direct cost | **DCM** | dichloromethane |
| **DES** | deep eutectic solvents | **DESW** | double-ended surface walking |
| **DFT** | density functional theory | **DMAP** | 4-(dimethylamino)pyridine |
| **DOS** | density of states | **$E_a$** | activation energy |
| **EC** | equipment purchase cost | **EDS** | energy-dispersive X-ray spectroscopy |
| **ELA** | ethyl lactate | **FCI** | fixed capital investment |
| **FE** | fixed expenses | **FID** | flame ionization detector |
| **FS** | final structure(s)/state(s) | **GC-FID** | gas chromatography–flame ionization detection |
| **GC-MS** | gas chromatography–mass spectrometry | **GGA** | generalized gradient approximation |
| **HDPE** | high-density polyethylene | **HF** | Hartree–Fock |
| **HK** | Hohenberg–Kohn | **IC** | indirect cost |
| **ILs** | ionic liquids | **IS** | initial structure(s)/state(s) |
| **KS** | Kohn–Sham | **LA** | lactic acid |
| **LAPW** | linearized augmented plane wave | **LCA** | life cycle assessment |
| **LCAO** | linear combination of atomic orbitals | **LD** | lactide |

| | | | |
|---|---|---|---|
| **LDA** | local density approximation | **LDOS** | local density of states |
| **LDPE** | low-density polyethylene | **L-LD** | L-lactide |
| **M2MP** | methyl-2-methoxy propionate | **MCDA** | multi-criteria decision analysis |
| **MeOH** | methanol | **meso-LD** | meso-lactide |
| **ML2A** | methyl lactyl lactate | **MLA** | methyl lactate |
| **Mt** | million tonnes | **Mw** | molecular weight |
| **NIR** | near-infrared spectroscopy | **NRTL** | Non-Random Two-Liquid |
| **Ov** | oxygen vacancy | **PAW** | projector augmented-wave |
| **PBAT** | polybutylene adipate terephthalate | **PBE** | Perdew–Burke–Ernzerhof |
| **PBS** | polybutylene succinate | **PC** | polycarbonate |
| **PCL** | polycaprolactone | **PDOS** | projected density of states |
| **PE** | polyethylene | **PES** | potential energy surface |
| **PET** | polyethylene terephthalate | **PHBV** | poly(3-hydroxybutyrate-co-3-hydroxyvalerate) |
| **PLA** | polylactic acid | **PP** | polypropylene |
| **PS (DFT)** | pseudopotential | **PS (polymer)** | polystyrene |
| **QA/QC** | quality assurance/quality control | **QMC** | quantum Monte Carlo |
| **ROH** | alcohol | **ROP** | ring-opening polymerization |
| **SCF** | self-consistent field | **SEM** | scanning electron microscopy |
| **STEM-EDS** | scanning transmission electron microscopy with energy-dispersive X-ray spectroscopy | **TBD** | 1,5,7-triazabicyclo[4.4.0]dec-5-ene |
| **TDOS** | total density of states | **TEM** | transmission electron microscopy |
| **Tg** | glass transition temperature | **Tm** | melting temperature |
| **TOF** | turnover frequency | **TPS** | thermoplastic starch |
| **TTIP** | titanium isopropoxide | **UV** | ultraviolet |

| | | | |
|---|---|---|---|
| **VASP** | Vienna Ab initio Simulation Package | **VBM** | valence band maximum |
| **VOCs** | volatile organic compounds | **WPLA** | waste PLA |
| **XPS** | X-ray photoelectron spectroscopy | **XRD** | X-ray diffraction |

# Chapter 1

# Introduction

The vast quantities of plastic waste have become a major environmental challenge of the 21st century. Polylactic acid (PLA), the largest market bioplastic, has seen steadily increasing use, and its end-of-life management now demands urgent attention. This chapter reviews PLA recycling routes, namely biodegradation, thermal degradation, hydrolysis, and alcoholysis. Among these, an alcoholysis-centric loop emerges as especially promising for closed-loop recycling of PLA. Because lactide (LD) is the key intermediate for re-polymerizing PLA, we examine the one-step conversion of methyl lactate (MLA) to LD, identify where performance can be improved, summarize the current research gaps, and set the aim and objectives that guide the research of this thesis.

# 1.1 Background

## 1.1.1 Global plastic challenge

In the modern era, plastics have emerged as both indispensable and pivotal materials, due to their properties like durability, strength, flexibility and cost-effective production. Plastics are now widely used across many sectors, including packaging, construction and infrastructure, transportation, aerospace, electrical and electronics, agriculture, healthcare, textiles, and 3D printing[1–3]. Since 1950, plastic production has grown rapidly[4] reaching a global output of 413.8 Mt (million tonnes) by 2023[5]. It is further projected that the global plastic production will rise to between 902 and 1124 Mt by 2050.

Among all types of plastics, approximately 98% are derived from fossil-based sources, primarily driven by their low production cost[6]. Of this total, about 44% comes from coal, 40% from petroleum, 8% from natural gas, 5% from coke, and 1% from other sources, bio-based sources account for just 2% of the feedstocks used to produce plastics worldwide[6]. This reliance of fossil source comes with significant drawbacks, including the depletion of non-renewable resources and complicated recycling challanges[7]. At present, the fossil resources used for plastic production account for about 6% of global fossil resource use[8], as plastic demand rises year by year, this is increasing resource depletion.

Regrettably, by 2022, the global recycling rate was still stalled at roughly 9%[6]. Such a low recycling situation not only spends precious fossil resources but also increases environmental pollution. When non-biodegradable plastics are disposed of via landfilling, they merely occupy valuable land resources. Moreover, microplastics that enter soils can

accumulate over years in agricultural fields[10], altering soil physicochemical properties and affecting crop performance[11]. Some microplastics are also transported into rivers via surface runoff, and dispersed through the atmosphere by wet and dry deposition, forming "plastic rain"[12]. In the marine environment, existing data indicate that only in the Great Pacific Garbage Patch contains a floating mass of approximately 0.079 Mt[13]; within the ocean interior, the estimated mass of suspended microplastics composed of common polymers (polyethylene (PE)/polypropylene (PP)/polystyrene (PS)) already reaches 11.6 to 21.1 Mt[10]. Terrestrially, this relentless accumulation not only monopolizes valuable land but also persists, resisting degradation. In marine ecosystems, these tiny plastic fragments, though seemingly inconspicuous, persist indefinitely. Regrettably, they become inadvertent prey to marine life, disrupting the balance of marine biodiversity. Given the huge challenges associated with traditional plastic management, the search for viable alternatives has never been more pressing.

### 1.1.2 PLA

In the face of mounting challenges posed by fossil-based plastics, the scientific community has pivoted towards biopolymers as a potential opportunity. Figure 1.1 shows the chemical structure of PLA, which is both bio-based resource and biodegradable plastic, normally synthesis of lactic acid (LA) by microbial fermentation of sugar or starch. Notably, certain techniques have championed cellulosic substrates as feedstock[14]. The first PLA derived from LA that emerged in the 20th century. PLA was first reported in 1932 when Wallace H. Carothers, a DuPont scientist, obtained low molecular weight PLA by heating LD, high molecular weight PLA became practical after DuPont's 1954 LD purification advances[15]. Industrial-scale PLA arrived in the early 2000s via Nature Works/Cargill-Dow, achieving a production capacity of approximately $1.36 \times 10^5$ MT

annually by 2002[16]. Fast forward to 2024, the global PLA production landscape was accounted 37.1% of the bioplastics sector[17]. Projections indicate an upward trajectory, with production capacity slated to touch 42.3% by 2029[17]. Evidently, the meteoric rise of PLA underscores not only its potential but also the imperative to refine its synthesis and post-production processes.

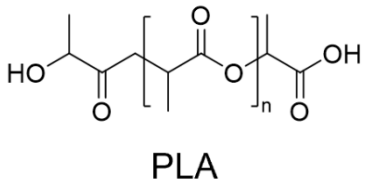


PLA

Figure 1.1 Polymeric structure of PLA[19]

PLA is from the family of poly-α-hydroxy acid, which is a type of a thermoplastic polyester[18]. Structurally, the chiral monomer of PLA leads to poly(L-lactic acid) (PLLA), poly(D-lactic acid) (PDLA), or mixed stereochemistries (meso-PLA), the properties of them are shown in Table 1.1. PLLA and PDLA are semicrystalline material, while meso-PLA is an amorphous type[19]. PDLA is most used to combined with PLLA to produce PLLA/PDLA blends[20], pure PDLA applications are relatively limited[21]. Owing to its amorphous structure, meso-PLA is commonly used in the medical field[22]. The biocompatibility, good mechanical properties (high tensile strength and modulus) of PLLA, which has helped its adoption across diverse sectors, including packaging, medical devices, biomedical, 3d printing, engineered blends/bio-composites and agriculture[23]. The commercial grade of PLA market is PLLA[19,24], the further research of PLLA in this thesis will be directly written as PLA.

Table 1.1 Physical property of PLLA/PDLA/meso-PLA

| Property | PLLA | PDLA | meso-PLA | Reference |
|---|---|---|---|---|
| Density ρ [g/cm$^3$] | 1.21-1.25 | 1.24-1.30 | 1.25-1.27 | [25–27] |
| Tensile strength σ [MPa] | 21-60 | 15.5-150 | 27.6-50 | [25–27] |
| Young's modulus E [GPa] | 3 | 2.7-4.14 | 1-3.45 | [25–27] |
| Glass transition temperature Tg [℃] | 45-60 | 55-65 | 50-60 | [25–27] |
| Melting temperature Tm [℃] | 150-162 | 170-200 | - | [25] |

### 1.1.3 PLA synthesis

Among the various routes for PLA synthesis, priority is given to approaches capable of producing high molecular weight (Mw) PLA. There are two main reasons for this. First, the mechanical properties of PLA are directly correlated with Mw, as chain scission occurs and Mw decreases, both tensile strength and modulus deteriorate[28]. Components intended for load bearing or long-term service therefore require a high initial Mw to maintain performance over time. Second, many industrial forming operations (film blowing, foaming, fibre spinning, blow moulding) demand sufficient melt strength/elasticity, which low Mw PLA cannot provide; increasing Mw (or using chain extension to raise the effective Mw) restores melt strength and markedly improves processability[29].

PLA is produced by (i) direct polycondensation of LA; (ii) prepolymerization of prepolymer first, then polymerization of PLA; or (iii) the LD route followed by ring-opening polymerization (ROP). The three routes are shown in Figure 1.2. While direct polycondensation is simple, removal of water and equilibration constraints cap the attainable Mw (1000-5000g/mol)[30] unless aided by chain extenders. For prepolymerization-polymerization route, although higher molecular weights are attainable, this route remains constrained by the equilibrium nature of polycondensation, as ester-bond hydrolysis drives the reaction backward[31]. For high-molar-mass, narrowly dispersed grades, the LD-ROP route is the most commonly used industrial method [15].

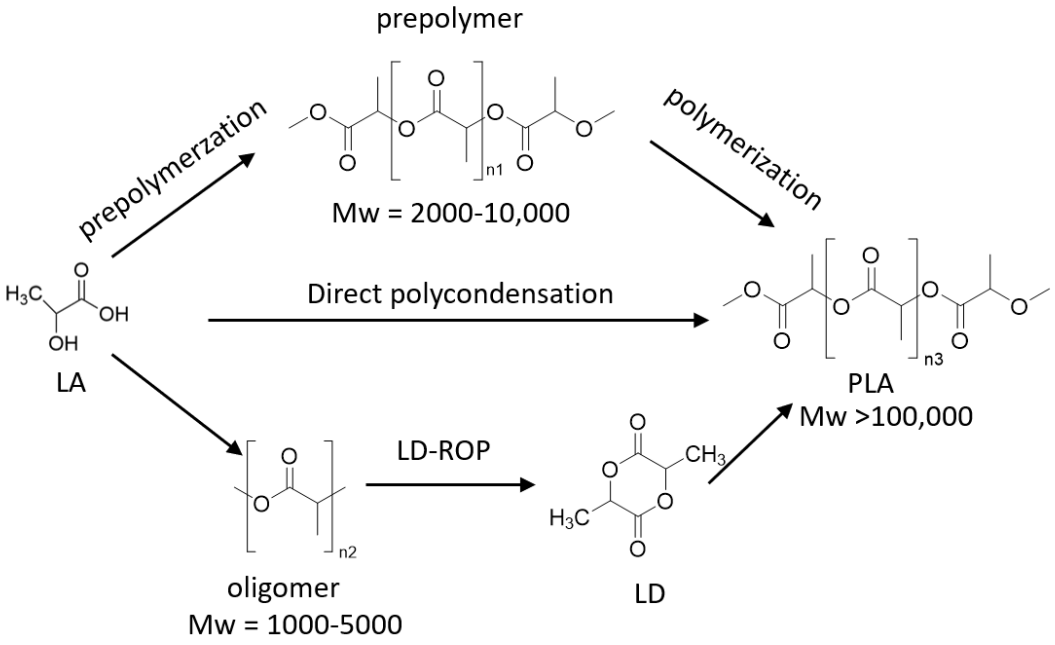


Figure 1.2 Three routes of PLA synthesis from LA

The current industrial (LD→ROP) PLA production model (Figure 1.3) begins with the fermentation of carbohydrate feedstocks (like sugar) to crude LA (usually L-LA). The crude LA is then purified through a multi-step process wherein it is first esterified to form a more volatile alkyl lactate intermediate. The alkyl lactate is subsequently purified via distillation and then hydrolysed back to purified LA. The purified LA subsequently undergoes a polycondensation reaction, yielding a low-molecular-weight oligomer PLA, with molecular weights ranging from 300 to 20,000 g/mol. In the next stage, the oligomer PLA is catalytically depolymerized under high temperature backbiting process to produce LD, the cyclic dimer of LA. Finally, the LD undergoes a controlled ROP to be converted into the high-molecular-weight PLA, typically exceeding 140,000 g/mol[32 33]. However, the synthesis of LA (including the purchase of feedstock) presents a formidable economic challenge, accounting for a 50% of the overall production cost. The transition from LA to LD further escalates costs by 30%, leaving a mere 20% for the polymerization phase[34].

Obviously, the synthesis of LA process is a key point in the PLA production. The economic burden of synthesising LA reduces the commercial viability of PLA.

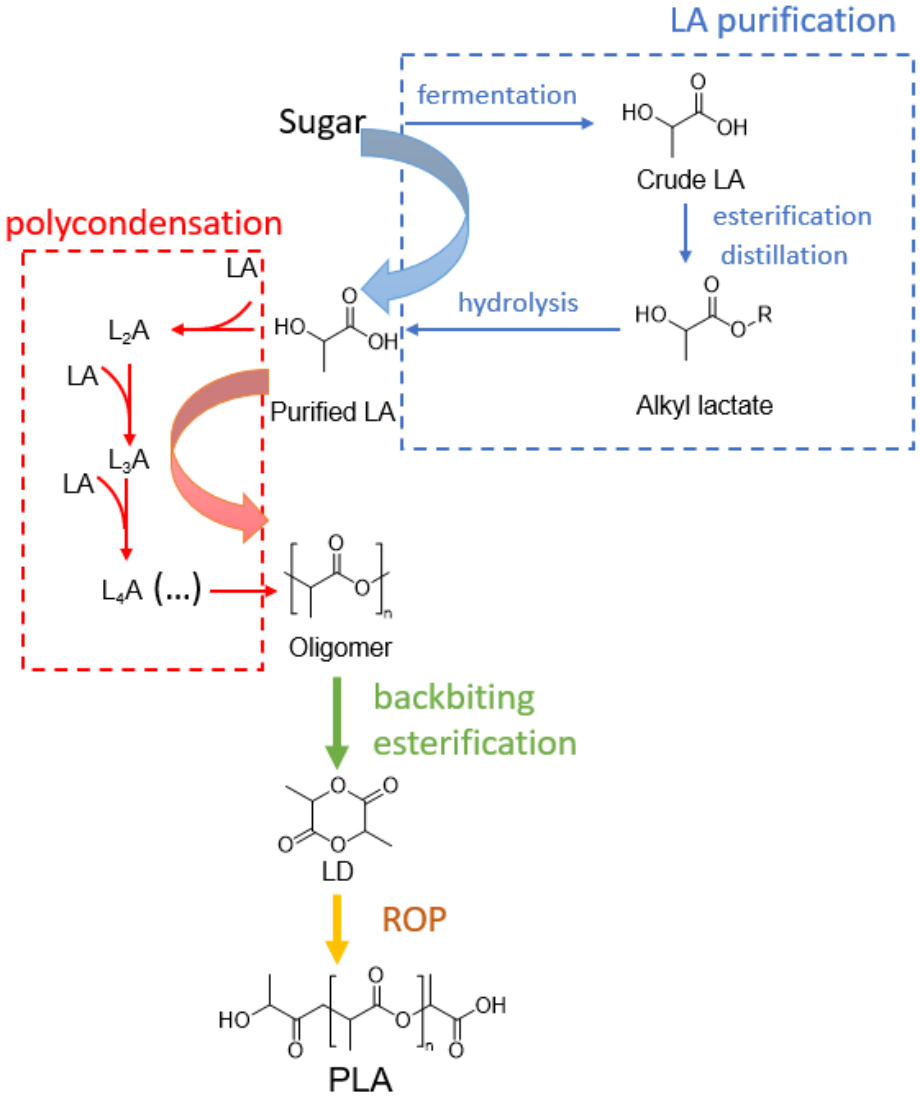


Figure 1.3 The industrial production route of PLA

## 1.1.4 End-of-life options

With the continuous progress of PLA synthesis technology and the enhancement of its properties, the production of PLA has also increased. The upward trend has raised concerns regarding the post-use management of PLA. The Waste Framework Directive,

a cornerstone of EU's waste management strategy, delineates the waste hierarchy as illustrated in Figure 1.4[35] [36]. The priority order, from most to least desirable, is: (i) prevention; (ii) preparing for re-use; (iii) recycling; (iv) other recovery (for instance, energy recovery); and (v) disposal. Within the recognized waste management hierarchy, recycling is a high-priority action second only to prevention and reuse. Consequently, the sustainability of any given polymer is fundamentally dependent upon the existence of a viable pathway for its recycling at the end of its service life.

Within this framework guiding, the sustainability of PLA hinges on recycling pathways that retain material quality. Because recycling ranks immediately below prevention and re-use in the hierarchy, long-term sustainability depends on deploying viable mechanical and chemical recycling routes at scale, with preference for options that preserve or restore high molecular weight and performance.


Figure 1.4 Waste hierarchy in Europe *(reprinted from Ref.[36]).*

## 1.1.5 Recycling methods

Before recycling, post-consumer plastics are routed through a pretreatment that comprises (i) collection and sorting; (ii) shredding; (iii) washing; and (iv)

reprocessing[37,38]. Once pretreatment is completed, the material can proceed four hierarchically ordered recovery routes[37,39]:

(i) Primary recycling returns clean, single-grade scrap to products of identical composition via simple re-extrusion, preserving virgin-grade properties. It is the simplest way to achieve closed-loop recycling by mechanical recycling method, but the requirements for products to be recycled are high, only high-quality plastics can be used for primary recycling[40]. Moreover, it is feasible only for clean, uncontaminated, single type plastics, and even the material can endure only a limited number of reprocessing cycles[39]. (ii) Secondary recycling is using mechanical methods (like screw extrusion, injection or blow moulding) to reprocess the low-quality waste plastic. The secondary recycling is still a down-grade process, the final product will have diminished properties because of the deterioration with each cycle. After limited mechanical recycling times, it cannot be further recycled by this method. (iii) Tertiary recycling (chemical) depolymerizes plastics through hydrolysis, alcoholysis, or pyrolysis to regenerate monomers or value-added chemicals. The monomers can be repolymerized to the new plastic as the feedstock, enabling true circularity. (iv) Quaternary recycling combusts otherwise unrecyclable fractions to recover heat and power; while useful as a last recovery option, it destroys embodied molecular energy and can release hazardous emissions. Optimal integration of pretreatment with these four routes maximizes resource efficiency and minimizes life-cycle greenhouse gas emissions, which is an imperative for a circular plastics economy.

For post-consumer PLA, five possible recycling routes have been reported (Figure 1.5): mechanical recycling, biodegradation, thermal degradation (chemical recycling), hydrolysis (chemical recycling), and alcoholysis (chemical recycling). As illustrated in

Figure 1.5, expect biodegradation recyling route,which degredated PLA to $CO_2$ and water, others four routes still have opputunities to achieve the closed-loop recycling for PLA. While biodegradation offers an alternative end-of-life solution, it does not facilitate a circular material economy. Nevertheless, significant practical hurdles and technical limitations are associated with each of these recycling pathways, necessitating a detailed exploration to understand their respective challenges and potential.

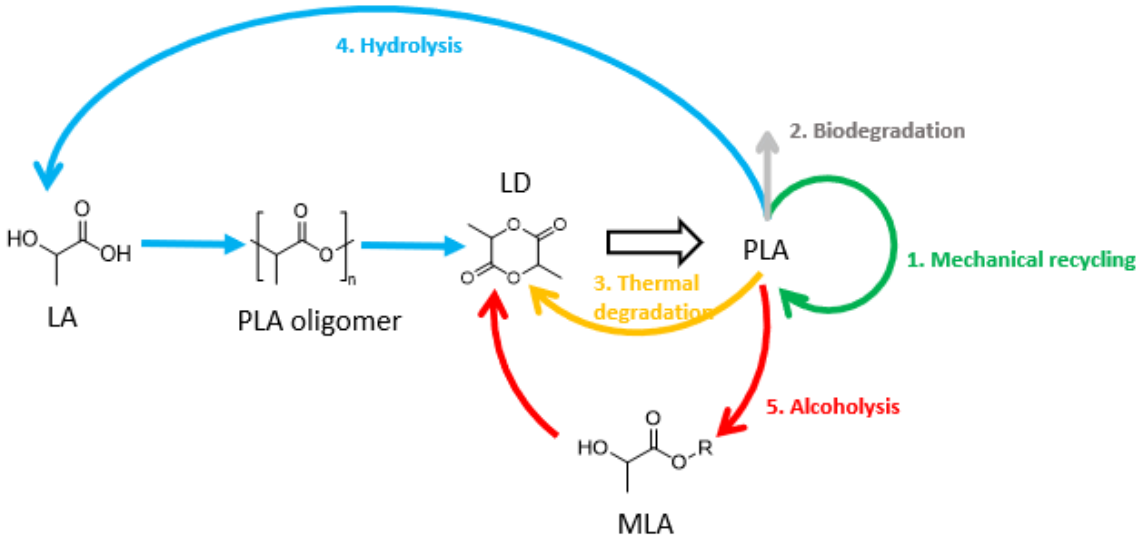


Figure 1.5 Recycling options for PLA

## *Mechanical recycling*

Mechanical recycling, as the primary or secondary recycling, involves reprocessing the post-consumer PLA into either virgin-grade or downgraded PLA. Among the five recycling routes, it demonstrates the lowest environment impact based on life cycling assessment (LCA) comparisons[41,42]. With mechanical recycling method, there is no need to break the polymer backbone into monomers. It is appealing since it can be set up with low investment and clean mono-material feedstocks, it also sidesteps the yield loss and energy-intensive steps of depolymerization.

The mechanical recycling process of PLA is shown in Figure 1.6. The recycling begins with a pretreatment stage: collection/sorting→shredding→washing→drying[41], to control reprocessing steps aimed at preserving the material's quality.

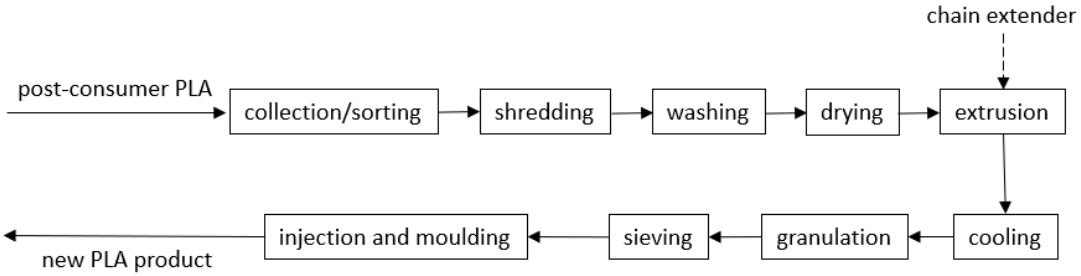


Figure 1.6 Mechanical recycling process of PLA

(i) Collection/sorting. The collection/sorting step aims to separate PLA from non-PLA polymers and obvious contaminants, thereby maintaining the material quality of downstream processes. In mixed packaging streams, PLA's density is around 1.21-1.25 g/cm³ and thus sinks in water, enabling gravity/sink-float steps to split PLA from others, like PP/PE ($\rho < 1$) that float[43]. However, PLA and PET have similar densities, so spectroscopic sorting is needed to prevent cross-contamination[44].

(ii) Shredding. After collection/sorting, items are shredded to produce flakes with a consistent size distribution, which improves washing efficiency and label/adhesive removal[45].

(iii) Washing. Washing step is to remove organics, surfactants, labels, inks, and fines, by friction washing and water polishing. Using these methods can reduce odour and yellowing while removing catalytic impurities that would otherwise accelerate chain scission during remelting[46–54]. Standard

plastics washing step uses water with detergents (sometimes hot/mildly alkaline) to lift soils and adhesives. PET-line studies document hot-wash sequences (e.g., 30 °C prewash then 85 °C hot wash) that raise cleaning efficiency[55]. For PLA, caution is necessary because its ester bonds hydrolyse more rapidly in alkaline media and at elevated temperature, especially above glass transition temperature Tg, aggressive caustic conditions or long exposures can reduce Mw before extrusion[56]. Accordingly, sources recommend effective but not overly caustic/hot washes for PLA, followed by quick dewatering and prompt drying in the next stage to suppress hydrolysis[56].

(iv) Drying. Before any melt step, PLA must be thoroughly dried to suppress hydrolytic scission, which lowers viscosity and Mw. Industrial guidance for Ingeo™ grades recommends ≤ 250 ppm moisture (Karl-Fischer) and notes that inadequate ppm-level drying is a major root cause of quality problems, in-line drying is advised for injection moulding and extrusion[57]. After pretreatment, clean PLA goes to extrusion.

(v) Extrusion. A single- or twin-screw extruder, where they are plasticized and homogenized into a uniform melt[58]. The processing temperature normally ranges from 165 to 220 ℃, though it may vary slightly depending on the grade of the original PLA[59,60]. A dedicated devolatilization (vacuum-vent) zone is used to strip residual moisture and volatile organic compounds (VOCs) from the melt, reducing odour and helping to stabilise rheology, vacuum-assisted devolatilization for recycled polymers is widely documented[61]. For PLA, the devolatilization

strips residual moisture and low Mw volatiles (like LD and cyclic oligomers)[62]. Where prior use or reprocessing reduces molecular weight, reactive extrusion with multifunctional epoxy chain extenders can reconnect or branch chains, thereby increasing the apparent Mw and enhancing melt elasticity or strength for downstream forming processes.

(vi) Cooling. The cooling step is for the easier further cut.

(vii) Granulation. Standard strand pelletisers produce "industrial size" cylindrical pellets of about 3 × 3 mm (diameter × length). Depending on the die design and take-off speed, diameters generally range from 1 to 3.5 mm and lengths from 0.8 to 5 mm, while micro-pellets as small as 1 mm in length are also feasible[63–67].

(viii) Sieving. After strand cutting, pellets are passed over one or more screens or vibratory classifiers to remove oversize longs, tails and fines, thereby narrowing the pellet-size distribution and improving flowability, dosing accuracy, and moulder stability[68].

(ix) Injection and moulding. This stage plasticises and homogenises the dried PLA, meters the melt, and fills the cavity; residence time and shear are kept moderate to limit hydrolysis and back-biting to cyclic oligomers that reduce molar mass[69]. In practice, PLA is commonly injected with a melt set around 180 to 210 °C (typical values used in injection-moulding studies), while the mould temperature governs the final morphology: cold moulds (25 to 50 °C) give largely amorphous parts, whereas heated

moulds (90 to 120 °C) plus adequate hold time enable in-mould crystallisation, raising crystallinity and stiffness[70,71].

The main challenge in mechanically recycling PLA lies in its high sensitivity to processing conditions. Elevated temperature and shear stress accelerate chain scission and thermo-oxidative, rapidly reducing the polymer's weight-average molar mass and consequently diminishing its mechanical performance. Peng Zhao et al. [72] reported that for PLA 4032D used in 3D printing applications, the molar mass decreased by 16.4% after only one extrusion cycle. The material can be reprocessed for only two 3D printing cycles, as reprocessed material cannot be further processed. Isabelle Pillin al. [73] reported for PLA L9000, after 3 injection cycles, the molar mass of PLA decreased by 50%, after 7 injection cycles, a 70% decrease of molar mass was achieved, which is a severe degradation of PLA. Marian Żenkiewicz et al. [74] reported that for PLA 2002D, 10 extrusion cycles produced a modest fall in tensile strength but a pronounced rise in melt-flow rate and gas-permeability values. While the glass transition temperature remained unchanged, both the cold-crystallization temperature and melting point shifted downward, indicating chain scission and molecular weight reduction. The resulting material properties degraded to the extent that it cannot be used for the same purposes as the virgin polymer. These findings collectively demonstrated the finite recycling window of pure PLA through mechanical recycling.

To counteract the material downgrading PLA, a chain extender (like Joncryl ADR-4368, Bioadimide® 100 – KI, MDI) was added during the extrusion process[42]. Pillin et al. championed the use of quinone stabilizers to preserve PLA's molecular integrity during the moulding phase[75].The chain extenders and stabilizers can temporarily rebuild molecular weight and recover tensile strength, which can increase the mechanical

recycling for several more cycles[76]. However, the benefit of adding extenders or stabilizers is temporary: cumulative chain scission, contaminant build-up, and colour shift still erode performance, ultimately requiring the resin to be blended with virgin PLA or diverted to other recycling pathways. Although mechanical recycling allows for closed-loop recycling, the number of achievable recycling times is limited, making it unsustainable for maintaining a fully circular economy in the long term.

## *Biodegradation*

Biodegradable recycling relies on the capacity of soil microorganisms, operating optimally under elevated temperature and humidity conditions. These natural microorganisms, endowed with enzymatic activity, in conjunction with processes like oxidation, photolysis, or radiolysis, can fragment the primary or subsidiary chains of macromolecules, facilitating degradation[77]. For PLA, the biodegradation process is after the hydrolytic degradation, then catalysed the monomer or oligomer by multiple types of microbes[78].

In modern municipal landfills, the waste is typically anaerobic and mesophilic with patchy moisture. Under these conditions for PLA, the hydrolysis of ester bonds is the rate-limiting step, which proceeds slowly because the temperature is lower than the glass transition temperature Tg (45-60°C). As a result, little soluble oligomer/monomer is produced for microbial conversion. Under ambient conditions (20°C), the natural biodegradation process of PLA can extend up to one year, at elevated temperatures (e.g., above 25°C), this degradation period can be reduced to approximately 12 weeks[79]. The biodegradation level was improved by raising temperature, moisture, adding microbes, adding enzyme in the soil. When the temperature is increased to around 55°C, this builds

thermophilic digestion conditions, PLA powders or films often achieve 60–99 % conversion within around 30-60 days. This enhanced degradation occurs because the temperature exceeds Tg, effectively removing the hydrolysis barrier[80]. Increase moisture can help hydrolysis step too, temperature still dominates outcomes. Actinomycete, bacteria, fungus can indeed accelerate PLA breakdown by secreting ester bond which is cleaving enzymes[81]. Under enzymatic catalysis, proteases, chymotrypsin, lipases, and carboxylesterases first cleave the ester bonds of PLA, reducing the polymer to soluble oligomers and monomeric LA. Subsequently, microorganisms assimilate and mineralise these small molecules: in aerobic systems, the end products are $CO_2$ and $H_2O$; in anaerobic systems, they are $CO_2$ and $CH_4$[82]. The schematic mechanism of PLA biodegradation is illustrated in Figure 1.7[129]. Proteinase K is a benchmark catalyst for PLA depolymerization: quantitative studies show rapid mass loss of PLA films and strong concentration-dependent kinetics; when proteinase K is embedded in PLA, films can lose around 78% mass in 96 h, illustrating how locally high enzyme activity bypasses diffusion limits[83].

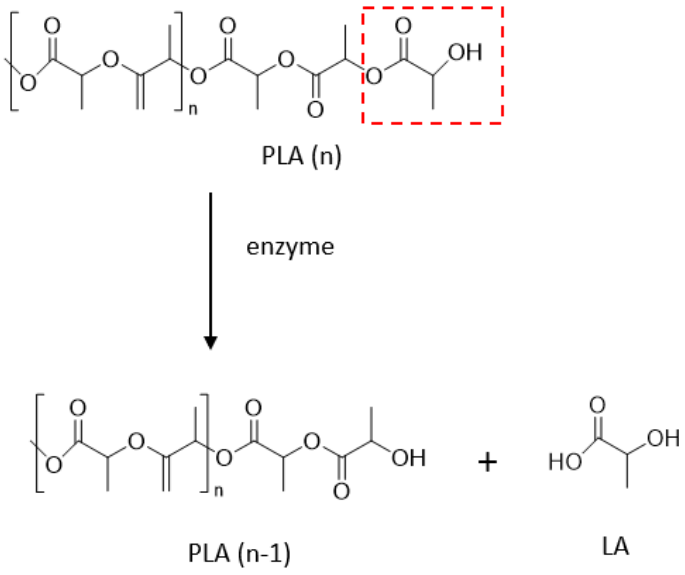


Figure 1.7 The schematic mechanism of PLA biodegradation by enzymatic process[129]

Although PLA can be biodegradable by landfill, however, the long degradation cycle primarily yields carbon dioxide and water as by-products, which cannot be efficiently reincorporated into PLA production to achieve the circular economy, resulting in resource wastage. Other methods that can shorten the biodegradation time of PLA, but the final products like $CO_2$, $CH_4$, water are still difficult to recycle.

## *Thermal degradation*

Thermal degradation, a form of chemical recycling, coordinated the decomposition of PLA through heating, with or without catalysts. The pyrolysis process is one type of the thermal degradation, which is heated in an inert environment with or without catalysts[39].

McNeill et al. [84] first demonstrated that PLA has a single mass-loss between 250 and 450 °C, producing $CO_2$ as the major volatile and over 50 wt % cyclic oligomers in

the condensate. At lower temperature (~ 230 °C) the only detectable volatile is acetaldehyde, generated by cis-elimination at hydroxyl-terminated chain ends. Increasing the temperature above 360 °C broadens the products to include $CO_2$, ethylene, propylene and methyl ketene, evidence of extensive chain scission[85]. Capping the terminal hydroxyl group suppresses the intramolecular transesterification "backbiting" that otherwise initiates degradation, thereby stabilising the polymer. Mechanistically, PLA pyrolysis can proceed through random chain scission, unzipping depolymerisation, cis-elimination, intermolecular transesterification, intramolecular transesterification "back-biting" (Figure 1.8) [86]. Below ~ 270 °C backbiting dominates, forming cyclic di- and trimers together with acetaldehyde and CO. At higher temperatures, the cleavage reaction of alkyl- and acyl-oxygen predominates, generating $CO_2$ and methyl ketene, respectively[85].

Residual or deliberately added metal species profoundly reshape the reaction pathway. Noda *et al.* ranked catalytic activity for intramolecular transesterification as Sn > Zn > Zr > Ti > Al[86]. Because Sn(II) carboxylates are widely used in commercial ring-opening polymerisation, tin residues are common in industrial PLA. Increasing Sn content from 20 to 607 ppm switches the primary product from cyclic oligomers to LD and lowers $E_a$ from 185 to 119 kJ/mol[87]. Further pyrolysis of Sn-rich PLA (≥ 689 ppm) exhibits zero-order weight loss with $E_a$ around 80–90 kJ /mol and produces L-LD almost exclusively, consistent with an unzipping depolymerisation mechanism. Alkaline-earth oxides behave similarly[88]. Calcium-end-capped PLLA is pyrolyzed at 280–370 °C followed first-order kinetics (~98 kJ/mol) and yields mainly LD through unzipping transesterification[89]. Bulk CaO and MgO additives also reduces the activation barrier and channelled the reaction toward LD, with MgO giving the highest stereochemical fidelity[90]. By contrast, low Sn (< 30 ppm) or the absence of basic oxides favours random scission,

producing a broad distribution of diastereomeric LDs and cyclic oligomers (~176 kJ/mol) [86].

Catalyst-free pyrolysis delivers appreciable LD only above 300 °C, where racemisation and side reactions complicate purification. Metal-assisted unzipping can lower the temperature window and improve LD selectivity, but requires strict control of residual catalyst level and chain-end chemistry. Even under optimised conditions, $CO_2$ evolution and overlapping boiling points (LD vs. methyl ketene, cyclic trimers) impose multi stages, deep vacuum separation. The limitations of thermal degradation motivate to explore other recycling methods.

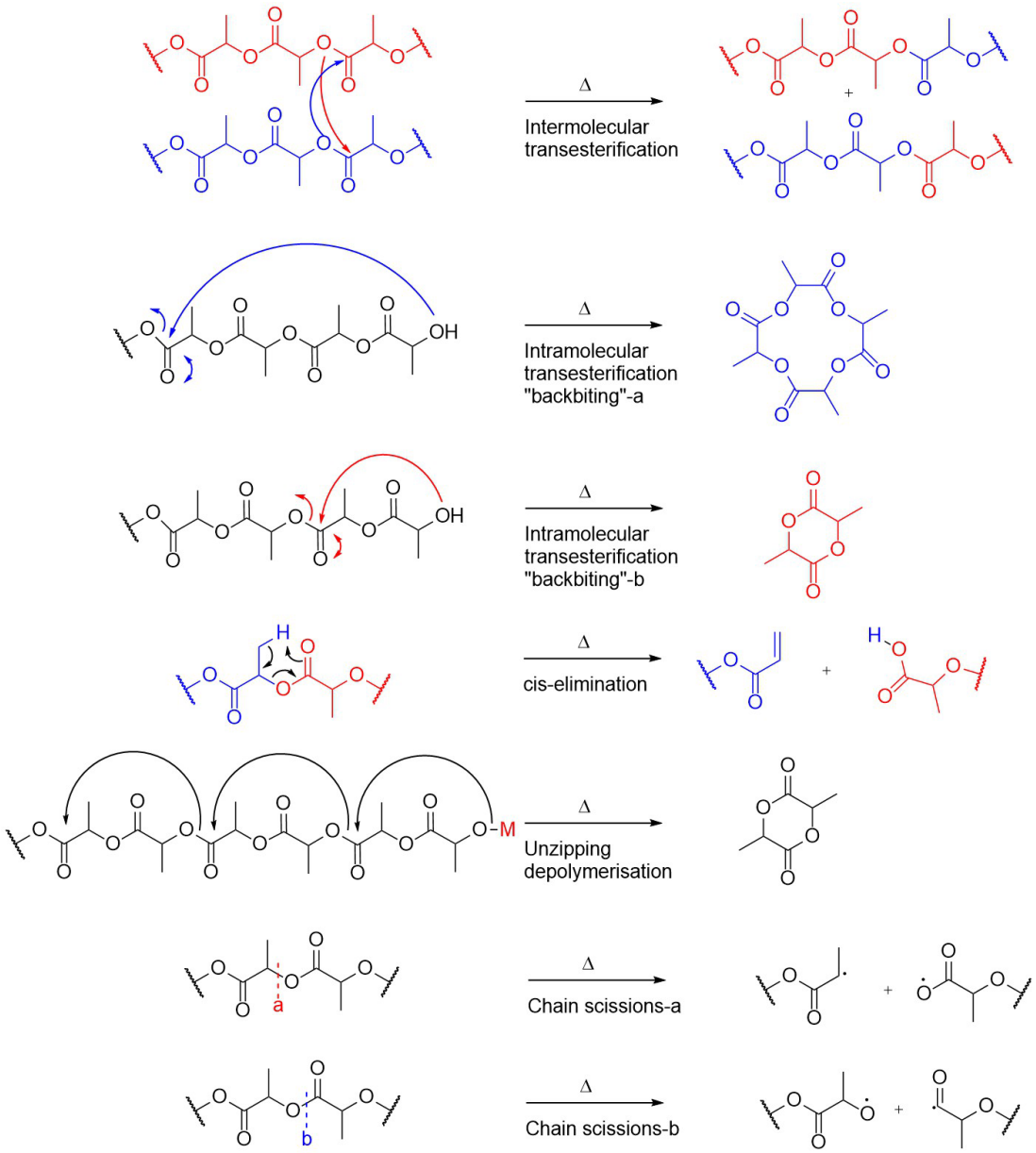


Figure 1.8 Possible thermal degradation mechanisms of PLA. M means metal salt: Sn(II), Mg(II), Zn(II), Fe(II), Al(III) [86]

## *Hydrolysis*

Because PLA is only slightly soluble in aqueous media, efficient hydrolysis generally requires elevated temperature and/or strongly acidic or basic conditions to drive water into the matrix and cleave the aliphatic ester bonds. In water-based systems where

PLA remains essentially insoluble, degradation proceeds by bulk or surface erosion. Which mechanism dominates is governed by the competition between water diffusion and bond-cleavage kinetics, and thus depends on molecular weight and end groups, part geometry/thickness, crystallinity, pH, and temperature. In bulk erosion, water penetrates faster than chains are cleaved, so molecular-weight loss and mass loss occur throughout the sample volume. In surface erosion, diffusion is slower than scission, so degradation localises at the surface, leading to gradual loss of thickness while the core remains largely intact. At the molecular level, hydrolysis produces soluble oligomers that further cleave to LA; the accumulation of carboxylic end groups can autocatalyse additional scission, especially at elevated temperatures or in confined geometries. The resultant product, LA, serves as a feedstock in PLA production, which could be achieved PLA closed-loop recycling by hydrolysis (waste PLA→ LA → Oligomer→LD →PLA).

Kinetic experiments conducted at 160–180 °C show that, even in the absence of added catalyst, over 95 % conversion to LA is achieved within two hours[91]. Because the reaction rate is proportional to the concentrations of polymer bonds, water and the carboxylic products formed during cleavage, the global rate law is third order; each cleavage step generates a –COOH group that accelerates subsequent cleavage, giving the process an intrinsically autocatalytic character[91]. The physical manifestation of hydrolysis depends on the competition between water ingress and bond rupture. When scission outpaces diffusion, the polymer erodes from the surface; when diffusion dominates, homogeneous bulk degradation ensues; and when acidic oligomers accumulate faster than they can diffuse away, an autocatalytic bulk-erosion mode develops that accelerates interior degradation[92,93]. Morphology adds a further layer of control: water penetrates

amorphous domains preferentially, and hydrolysis in highly crystalline layered structures is not detected until overall crystallinity approaches 99 %[94].

Solution pH determines the mechanistic pathway. Both acid and base conditions worked for the depolymerisation of PLA (Figure 1.9) [95,96]. Protonation of terminal hydroxyl groups in acid condition promotes unzipping depolymerisation and direct formation of LA, leading to rates that are independent of chain length[95,96]. Base solutions favour random backbiting within the chain, LD is first released and subsequently hydrolysed to LA, and under strongly basic conditions the reaction is fast enough to revert to a surface-controlled mechanism[97].

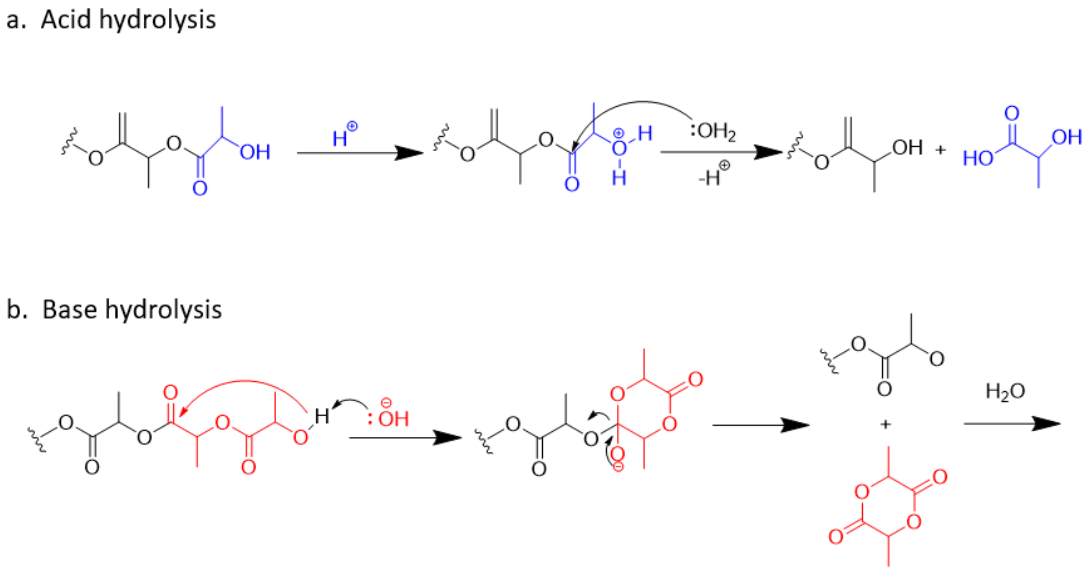


Figure 1.9 Possible hydrolysis mechanisms of PLA with acid and base conditions[95,96]

From an energy perspective, cradle-to-gate analysis assigns hydrolytic recycling an energy demand of around 14 MJ/kg LA, approximately one-quarter that of corn fermentation (55 MJ/kg LA)[98]. The principal limitations are (i) the energy-intensive conversion of LA to LD, which is usually carried out in a two-step

polycondensation/backbiting sequence under high vacuum, and (ii) the need to manage autocatalysis in inefficiently mixed reactors, which is a major obstacle to achieving cost-effective PLA.

## *Alcoholysis*

Alcoholysis is the nucleophilic cleavage of ester backbone of PLA by an alcohol (ROH), giving alkyl lactates, like methyl lactate (MLA) and ethyl lactate (ELA) via transesterification of repeat units and end groups, shows in Figure 1.10. These esters are valuable green solvents and platform molecules that can be converted back to LD and PLA or upgraded to other chemicals[99,100]. Three broad classes dominate: (i) Lewis acids (e.g., $Zn^{2+}$, $Fe^{3+}$) that polarise the C=O and activate the polyester toward nucleophilic attack[101]; (ii) Brønsted/nucleophilic organic bases (e.g., 1,5,7-Triazabicyclo[4.4.0] dec-5-ene (TBD) and undec-7-ene (DBU)) that activate ROH or form acyl-activated intermediates[102]; and (iii) ionic liquids (ILs) and deep-eutectic solvents (DES) that couple solvation with acid/base functionality, often allowing lower temperatures and straightforward product separation[100]. Well-defined Zn(II) complexes sit between (i) and (ii), providing high activity/selectivity under comparatively mild conditions[103].

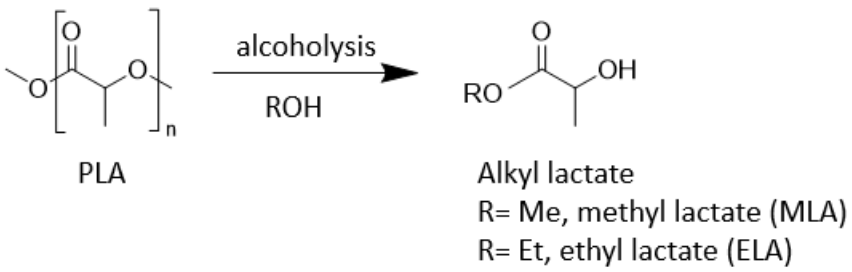


Figure 1.10 Alcoholysis of PLA[95]

Across catalysts, high MLA and ethyl lactate (ELA) yields are routinely achieved at 100 to 130 °C with MeOH or EtOH. With $Zn(OAc)_2$, methanolysis shows around 90% MLA at completion and kinetic fits that resolve multi-step apparent activation energies $E_a$ (e.g., 25–48 kJ/mol). Pairing $Zn(OAc)_2$ with TBD or DMAP gives a synergistic rate boost and reduced apparent barriers relative to single catalysts[101,104]. $FeCl_3$ in MeOH at ~130 °C has delivered >95% conversion and ~87% MLA selectivity within several hours with $E_a \approx 32$ kJ $mol^{-1}$ and demonstrated catalyst reuse[105]. Ionic liquids (e.g., [Bmim][OAc]) enable 92–96% conversion and 90% MLA selectivity around 110–115 °C, with reported $E_a \approx$ 38–47 kJ/mol depending on acidity. Zn-containing IL hybrids push activity further, achieving >97% conversion and 92% MLA selectivity at around 110 °C with multi-cycle reuse, with reported $E_a \approx 21$ kJ/mol[101,102,109] At the molecular catalyst side, well-defined Zn(II) complexes effect rapid methanolysis over 40–110 °C (solution/swell conditions), using $Zn(Et)_2$ achieve $E_a$ ~39–65 kJ/mol[107,108]. For EtOH, ELA selectivity and high conversion are observed, though temperatures or residence times are often slightly higher than MeOH to achieve parity[102,104,109,110].

## *Route selection*

For post-consumer PLA, the ideal scenario is using mechanical recycling route to achieve PLA closed-loop recycling, which maximises material reutilisation, preserves the polymer structure, and minimises energy demand. In practice, however, repeated melt-processing inevitably lowers molecular weight and diminishes mechanical performance, after only a few cycles, depending on processing history and additives, the recycled PLA no longer meets product specifications. Once mechanical recycling is no longer feasible, other recycling routes are needed. Biodegradation is often promoted as the "green" end-

of-life recycling option for PLA. If we use the general landfill method, the final products of biodegradation are $CO_2$ and water. However, the long residence time (12 weeks to one year) are consumed the land space that could otherwise serve other higher value activities. Meanwhile, because the polymer is broken down to the level of simple products, none of the carbon is directly available for re-entering the PLA supply chain; additional fermentation or chemical synthesis would be needed to rebuild LA, decreasing the benefit of degradation, which is also the waste of energy. Chemical recycling routes are still needed to explore.

Three chemical routes (thermal degradation, hydrolysis, and alcoholysis) have been investigated for achieving PLA closed-loop recycling. At least in principle, each route could complete a closed-loop recycling via regenerating the key precursor (LD), and then resynthesizing PLA with ROP.

For the thermal degradation, heating PLA with a high temperature (100-500°C) cleaves the chain and yields LD together with a complex mixture of cyclic oligomers, olefins, carbonyls, and $CO_2$. Although LD can be re-polymerised to virgin PLA, the multitude of by-products greatly complicates purification, severely limiting the practical feasibility of a closed-loop route based purely on thermal degradation.

Both of hydrolysis and alcoholysis pathways can achieve closed-loop recycling through a series of steps. In the hydrolysis-centric loop (Figure 1.11a), the direct hydrolytic derivatives of waste PLA into LA. Two possible processes could be used to synthesis PLA from recycled LA: (i) LA → Oligomer PLA → LD→PLA, using the industrial process first converses LA into oligomeric PLA via polycondensation (green route in Figure 1.11a), which then processes a transformation to LD, facilitated by the

backbiting mechanism, finally using ROP to resynthesise PLA again; (ii) LA →LD →PLA, a new route of LA to LD has been reported by Michiel Dusselier et al.[34] (yellow route in Figure 1.11a), which skips the step of oligomer, directly converses LD by cyclization from LA, then using ROP to resynthesise PLA again. In the alcoholysis-centric loop (Figure 1.11b), after alcoholysis process of PLA, alkyl lactate is conversed as the feedstock of the follow-up processes. Three technical options exist: (i) hydrolyse MLA to LA, followed by the conventional industrial LA to LD route (green route in Figure 1.11b); (ii) hydrolyse MLA to LA, then employ a one-step LA to LD process (yellow route in Figure 1.11b); or (iii) directly implement a one-step MLA to LD process (red route in Figure 1.11b), which reported by Rik De Clercq et al.[111]. After converting of MLA to LD, all these three routes using ROP to resynthesized PLA.

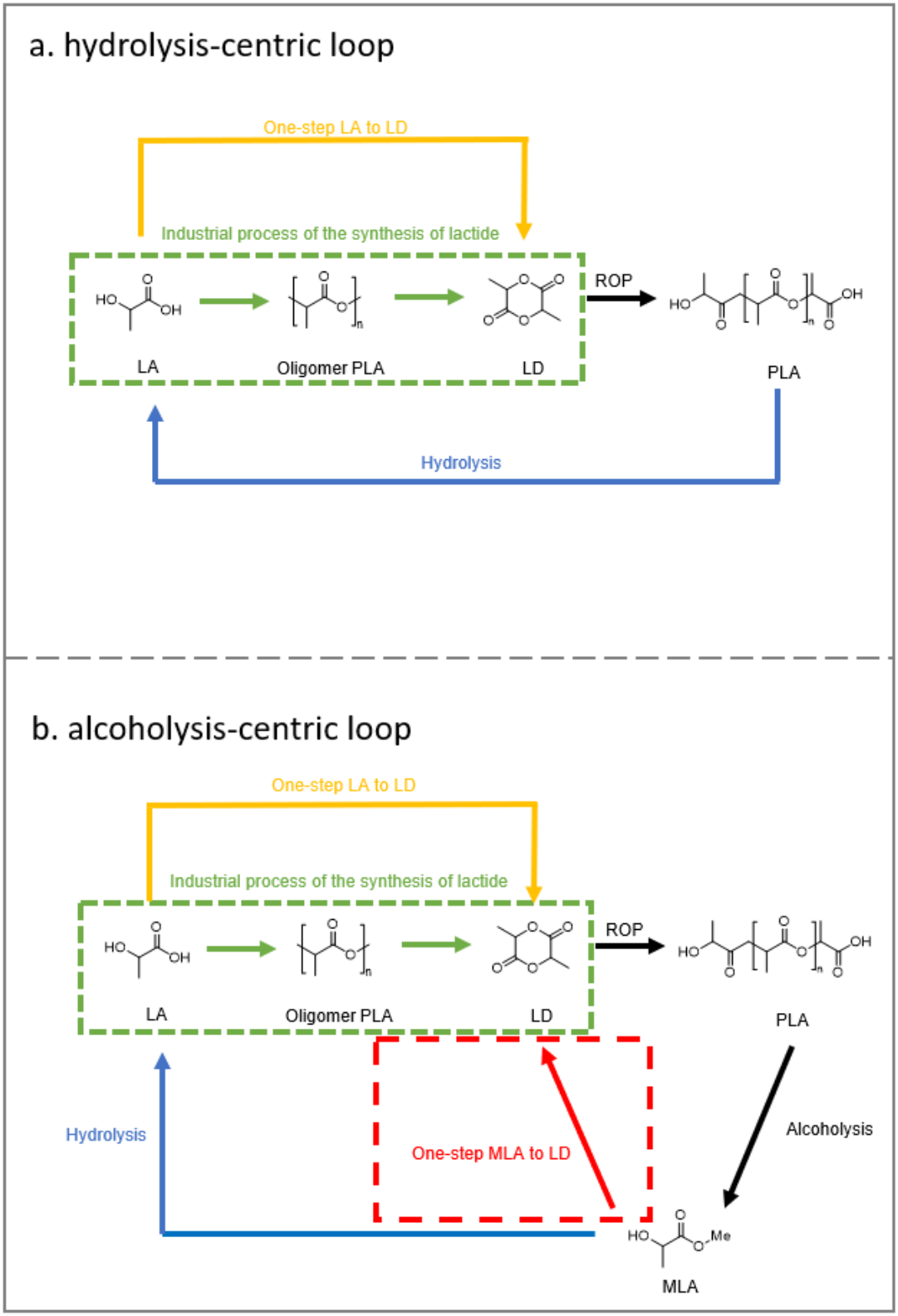


Figure 1.11 The process of PLA circular recycling via hydrolysis and alcoholysis

Table 1.2 is summarized the activation energies difference between hydrolysis and alcoholysis, alcoholysis of PLA generally exhibits lower apparent activation energies and hence faster kinetics than aqueous hydrolysis. It is therefore the preferred low temperature depolymerization route for circular recycling. For the PLA degradation step, alcoholysis is kinetically favoured (Table 1.2). The activation energy of alcoholysis is only 21 kJ/mol when 2[Bmim][OAc]–$Zn(OAc)_2$ is used as the transesterification catalyst, whereas uncatalyzed hydrolysis requires 53.23 ± 6.81 kJ/mol. The much lower barrier makes alcoholysis much easier to drive and, consequently, highly attractive for industrial scale-up. Accordingly, in this thesis, the alcoholysis-centric loop has chosen as the primary focus.

Table 1.2 The activation energies difference between hydrolysis and alcoholysis

| Recycling route | Catalyst | △Ea (kJ/mol) | Temperature (℃) | Reference |
|---|---|---|---|---|
| Hydrolysis | - | 83.68 | 21-45 | [112] |
| Hydrolysis | - | 53.23±6.81 | 140-180 | [112] |
| Alcoholysis | $Zn(OAc)_2$ | 25-48 | 100-130 | [101] |
| Alcoholysis | $Zn(OAc)_2$+TBD/DMAP | 73(step1)/40.16(step2) | 100-130 | [104] |
| Alcoholysis | $FeCl_3$ | 32.4 | 130 | [105] |
| Alcoholysis | [Bmim][OAc] | 38.29 | 90-115 | [113] |
| Alcoholysis | [$HSO_3$-pmim][$HSO_4$] | 47 | 115 | [102] |
| Alcoholysis | 2[Bmim][OAc]–$Zn(OAc)_2$ | 21 | 110 | [109] |
| Alcoholysis | $Zn(Et)_2$ | 39-65 | 40-130 | [107] |
| Pyrolysis | - | 177.5 | 100-150 | [114] |

Bmim: 1-butyl-3-methylimidazolium
Pmim:1-(3-sulfopropyl)-3-methylimidazolium

LD, the cyclic dimer of LA (1,4-dioxane-2,5-dione, 3,6-dimethyl), which is the key intermediate for polymer-grade PLA via ROP process. Because LA is chiral, LD occurs in three stereoisomers: L-LD, D-LD, and meso-LD[16]. The ratio of isomers determines the crystallinity of PLA, which is governed by the mixing ratio of the LD isomers: all L- or all D-LD gives semi-crystalline PLLA/PDLA, while meso-lactide

lowers crystallinity. Therefore, controlling and preserving stereochemistry is crucial. In practice, LD is easy to racemization during synthesis and handling, accelerated by heat, trace acid/base, even small amounts of water[115–117], which converts L- or D- into meso-LD, complicating purification and raising cost. When LA is chosen as the intermediate, MLA must first be hydrolysed to LA, adding both complexity and cost. In addition, whether the subsequent LA → LD step follows the industrial process or the one-step route, the reaction must be conducted under high temperature and deep vacuum while continuously removing water. This is because commercial LA is typically supplied as a 30–90 wt% aqueous solution, which can promote racemization side reactions and consequently generate the by-product meso-LD. Both LA-based routes also generate water stoichiometrically, necessitating further continuous removal of water or LD vapour and thereby driving up capital and operating costs. For the alcoholysis-centric loop, a third route emerges—a solvent-free, one-step continuous process for LD production, leveraging the transesterification of alkyl lactate. Recent insights from Rik De Clercq et al. spotlight the efficacy of Titania-Silica catalysts in this gas-phase one-step process, achieving LD selectivity nearing 90% with minimal LD isomerization. However, the LD yield remains a problem, at around 42%.[111,118-119]

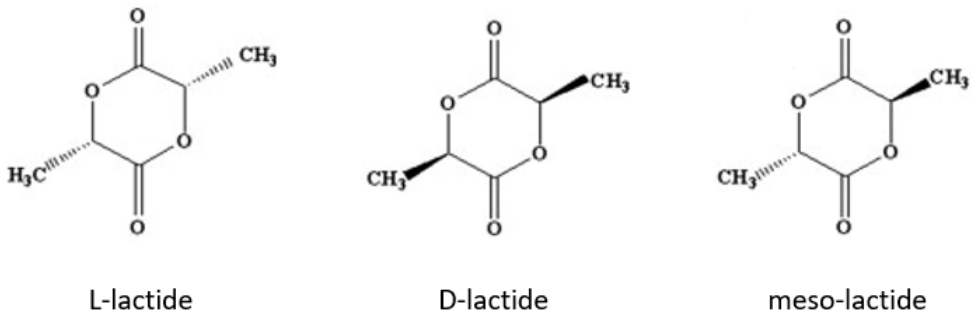


Figure 1.12 Structure of lactide

Since our comparison of PLA depolymerization routes shows that alcoholysis is the more promising option, and the LD → PLA step is conventionally accomplished by ROP, the synthesis of LD is the selected route to focus. Accordingly, the third alcoholysis-centric pathway is prioritized, which is the one-step conversion of MLA to LD. By solving this key intermediate step within the PLA closed-loop, the prospect of achieving a circular PLA economy becomes realistic.

### 1.1.6 One-step conversion of MLA to LD

Although the yield of LD obtained by one-step gas-phase transesterification of alkyl lactates produced via alcoholysis of waste PLA is still limited, the route offers several distinct advantages. (i) Feedstock economics. LD synthesis is the cost-defining step in commercial PLA production and conventionally relies on LA obtained by microbial fermentation of sugars or lignocellulosic hydrolysates which is an inherently expensive feedstock because of the pre-treatment of LA[34]. Converting the alcoholysis products of post-consumer PLA into the LD precursor therefore provides a far more economical and sustainable alternative. Because alkyl lactates vaporize at lower temperatures than LA, they can be evaporated and fed more gently. This shorter, cooler handling reduces side reactions in the evaporator and at the reactor inlet. (ii) High product selectivity. While the overall MLA to LD conversion is not yet optimal (lower than 42%[111]), the LD selectivity exceeds 90 %. Such high selectivity minimises by-product formation, simplifies downstream separation and purification, and thus reduces production costs.

The one-step conversion of MLA to LD proceeds via transesterification, as shown in Eq(1.1)[111]:

$$2\mathrm{MLA} \rightleftharpoons \mathrm{LD} + 2\mathrm{MeOH} \quad (1.1)$$

Thus, two moles of MLA form one mole of LD and two moles of methanol. In the synthetic route, MLA is processed by vaporization, subsequently mixing with nitrogen ($N_2$). The mixture gas then passes through a catalytic reactor to produce LD. The experimental results of the MLA to LD conversion are shown in Table 1.3. An analysis of the available data revealed: in the absence of catalyst[111], the conversion stagnates at 0%, indicates that no effective reaction is taking place. The inefficacy of $TiO_2$ or $SiO_2$ in catalysing the MLA to LD transition is obvious, given the low LD yield. Yet, the synergy with the $SiO_2$ support significantly alters the catalytic performance of the active phase of $TiO_2$. Comparison with other metal oxides, the $TiO_2/SiO_2$ is much better. An in-depth study of the performance of catalysis over $TiO_x/SiO_2$ catalysts could provide new ways for improving conversion and selectivity.

Table 1.3 Gas phase conversion of MLA to LD with various catalysts

| | | Selectivity (%) | | | Reference |
|---|---|---|---|---|---|
| Catalyst | Conversion (%) | LD | $ML_2A$* | Side products | |
| No catalyst [a] | 0 | 0 | 0 | 0 | [111] |
| H-beta (Si/Al=12.5) [a] | 48 | 7 | 0 | 93 | [111] |
| H-beta (Si/Al=150) [a] | 5 | 60 | 0 | 40 | [111] |
| $SiO_2$–$Al_2O_3$ [a] | 20 | 80 | 6 | 14 | [111] |
| Al-MCM-41 [a] | 24 | 49 | 5 | 46 | [111] |
| $SiO_2$ support [a] | 1 | 0 | 0 | 0 | [111] |
| $TiO_2$ (anatase) [a] | 32 | 11 | 5 | 84 | [111] |
| $TiO_2$ (rutile) [a] | 6 | 0 | 0 | 100 | [111] |
| $TiO_2$ (75%anatase/25%rutile) [a] | 16 | 0 | 0 | 100 | [111] |
| Physical mixture of $TiO_2$ (anatase, 5wt%) [a] | 4 | 0 | 0 | 100 | [111] |
| $MgO/SiO_2$ [b] | 33 | 81 | 18 | < 1 | [111] |
| $CeO_2/SiO_2$ [b] | 17 | 72 | 27 | < 1 | [111] |
| $La_2O_3/SiO_2$ [b] | 25 | 23 | 23 | < 1 | [111] |
| $Al_2O_3/SiO_2$ [b] | 32 | 11 | 11 | 7 | [111] |

| | | | | | |
|---|---|---|---|---|---|
| $Nb_2O_5/SiO_2$ [b] | 33 | 16 | 16 | 3 | [111] |
| $ZrO_2/SiO_2$ [b] | 43 | 14 | 14 | < 1 | [111] |
| $SnO_2/SiO_2$ [b] | 14 | 11 | 11 | < 1 | [111] |
| $TiO_2/SiO_2$ [b] | 50 | 12 | 12 | 10 | [111] |
| $\gamma$-$Al_2O_3$ [b] | 12 | 17 | 17 | 12 | [111] |
| $TiO_2/SiO_2$ 5wt% (impregnation) [a] | 42 | 90 | 8 | 2 | [111] |
| $TiO_2$/MCM-41 5wt%(impregnation) [a] | 46 | 90 | 9 | 1 | [111] |
| $TiO_2$–$SiO_2$ 5wt% (xerogel) [a] | 39 | 87 | 12 | 1 | [111] |
| Ti-zeolites (TS-1) [c] | 13 | 82 | 14 | 1 | [118] |
| Ti-zeolites (beta) [c] | 12 | 74 | 10 | 3 | [118] |
| $TiO_2/SiO_2$ (4.7 wt%) [c] | 14 | 88 | 10 | 0 | [118] |
| $TiO_2$/MCM-41 (4.2 wt%) [c] | 29 | 90 | 10 | 0 | [118] |
| $TiO_2$-$SiO_2$ gel (4.1 wt%) [c] | 20 | 91 | 7 | 0 | [118] |
| $SiO_2$ gel (support) [d] | 1 | 0 | 0 | 0 | [118] |
| Si-MCM-41 [d] | 2 | 0 | 0 | 0 | [118] |
| $SiO_2$ xerogel (sol-gel) [d] | 1 | 0 | 0 | 0 | [118] |
| Silicalite-1 (Si/Al = 940) [d] | 4 | 25 | 5 | 70 | [118] |
| Si-beta (Si/Al = 255) [d] | 10 | 19 | 2 | 58 | [118] |
| TS-1 (125-250μm) [e] | 20 | 85 | 12 | 1 | [118] |
| TS-1 (250-500μm) [e] | 22 | 84 | 12 | 2 | [118] |
| Ti-beta (125-250μm) [e] | 18 | 74 | 13 | 3 | [118] |
| Ti-beta (125-250μm) [e] | 17 | 75 | 11 | 3 | [118] |

a. Reaction conditions: 5.7 % L-MLA in $N_2$, T = 220°C, WHSV = 3.11/h;
b. Reaction conditions: 5.7% L-MLA in $N_2$, T = 220°C, WHSV = 1.04/h;
c. Reaction conditions: 5.7 % L-MLA in $N_2$, T =220 °C, WHSV = 15.5/h
d. Reaction conditions: 5.7% L-MLA in $N_2$, T = 220 °C, WHSV = 2.6/h
e. Reaction conditions: 5.7% L-MLA in $N_2$, T = 220 °C, WHSV = 7.8/h
* $ML_2A$: methyl lactyl lactate

Titanium-silica ($TiO_2/SiO_2$) catalysts have emerged as versatile materials in the field of heterogeneous catalysis, showing efficacy in a variety of chemical transformations. One of the most notable applications of titanium-silica catalysts is in the epoxidation of alkenes using hydrogen peroxide. This process is of significant industrial importance, especially in the production of epoxides, which are key intermediates in the synthesis of various chemicals[120]. Titanium-silica catalysts shows a high efficiency and molecular selectivity in the epoxidation reactions with hydrogen peroxide, such as olefin epoxidation, phenol hydroxylation, cyclohexanone and conversions of ammonia to hydroxylamine, secondary alcohols to ketones, and secondary amines to

dialkylhydroxylamines[121].This method is especially significant in the production of propylene oxide, with an estimated annual output of approximately 1Mt[121]. Beyond epoxidation, titanium-silica systems are not just limited to catalytic transformations. They have been employed as catalyst supports for active ingredients, expanding their applicability in various chemical processes[122]. Another application area of titanium-silica catalysts is photocatalysis. $TiO_2$ nanoparticles have good photocatalytic properties, but the nanoparticles are prone to agglomeration, which is not favourable for recycling. Catalytic loading of $TiO_2$ onto $SiO_2$ can successfully solve this problem. This method not only recycles the photocatalyst, but also provides abundant active sites for photocatalytic reactions[123 124].

The complex performance of titanium-silica catalysts mainly stems from their surface structure and the type of titanium present. Typically, the surface of these catalysts consists of a silica base made up of silicon-oxygen tetrahedra and titanium species that are bonded to it. These titanium species can be isolated, mononuclear, or they can be multinuclear or aggregated. The nature of these titanium species dictates the reactivity and selectivity of the catalyst[125]. The valence state of titanium in titanium-silica catalysts is of crucial importance. Primarily tetravalent titanium (Ti (IV)) is the most common species. Under certain conditions, trivalent titanium (Ti (III)) or another valence titanium will also be formed[126]. Titanium in high valence state and low valence state plays different roles in the catalytic reaction. The presence of Ti (IV) enhances the Lewis acidity of the catalyst, making it particularly effective in reactions that require strong Lewis acid sites. For instance, the epoxidation of alkenes and the oxidation of alcohols are significantly enhanced on titanium-silica catalysts due to the Lewis acidic nature of Ti (IV).

Ti (IV) in titanium-silica catalysts usually exhibits tetrahedral or octahedral coordination. The formation of Ti-O-Si bridges facilitates this coordination, which is crucial for creating active sites on the catalyst surface. The tetrahedral coordination of Ti (IV) ensures good dispersion and isolation of titanium centres and prevents the agglomeration of titanium species, thereby maintaining the high surface area and porosity of the catalyst[125]. Catalysts enriched with Ti (III) centres have been reported to direct the reaction with a pronounced selectivity towards the epoxide product, in contrast to their Ti (IV) catalysts[127]. However,, in the field of photocatalysis, using Ti (III) centres have shown excellent efficacy in generating hydroxyl radicals, thereby improving the degradation efficiency of organic pollutants[128]. While titanium-silica catalysts have been extensively documented across various domains, the distinct roles of Ti (IV)/Ti (III) site and silica support in the transformation of MLA to LD remain conspicuously uncharted, warranting further investigation.

# 1.2 Research Gap

Establishing a closed-loop, low-carbon economy for PLA is depended on the post-consumer PLA be depolymerised back to its cyclic monomer (LD), with high yield, modest energy input and bankable techno-economics. While recent research has shown promise, fourrelated research gaps currently impede industrial realisation:

a. Quantitative comparison of PLA with other plastics

Despite numerous handbooks and reviews compiling polymer properties, however, systematically evaluation on the sustainability potential of widely-used fossil-based and bio-based polymers is still lacking. A standardized, decision-grade dataset and applying multi-criteria decision analysis for polymers is necessary, which can enhance

the understanding of the importance of PLA and the areas where it still needs improvement.

b. Valence and support effect

Experimental studies[118] have provided valuable information of the catalytically active Ti sites. It is established that covalent Ti−O−Si bonds are a common feature and a higher turnover frequency (TOF) of the Ti sites for MLA→LD reaction. However, despite these important structural characterizations, fundamental questions about the valence of the active titanium still exist. The differences in catalytic contributions of Ti(III) versus Ti(IV) sites, as well as the synergistic role of the silica support beyond loading sites for catalyst metals remain unclear. The lack of a complete, predictive structure–activity model means that further catalyst optimisation for higher yield remains largely empirical rather than knowledge driven.

c. Fundamental mechanism

Experimental studies go no further than reaction performance observations[118]; no first-principles investigation of $ML_2A$ transesterification to LD on Ti(III)/Ti(IV)-$SiO_2$ surfaces has yet been reported. Consequently, the elementary reaction steps, the structures of key transition states, and the corresponding activation energy barriers for the various potential pathways (e.g., direct cyclization vs. linear dimer intermediate) remain purely speculative. Without such atomistic research, a predictive model cannot be constructed, leaving both catalyst development and reactor optimisation largely empirical.

d. Disconnect between lab-level process and economic viability

Laboratory studies have shown that $TiO_x/SiO_2$ catalysts can reach 85–92 % LD selectivity and that tetrahedral $TiO_4$ sites outperform octahedral centres, providing valuable structure–activity insight[118]. Yet no techno-economic analysis study has incorporated these validated findings into a plant wide process model. Existing PLA recycling analysis either target hydrolysis routes or rely on generic assumptions that are not relevant to a specific, characterised catalyst. The disconnect hampers a rational assessment of industrial potential and slows progress toward a truly circular PLA economy.

## 1.3 Aim and objectives

This thesis aims to develop a sustainable recycling concept that can address the engineering and environmental challenges associated with post-consumer PLA waste management and MLA production. MLA is the alcoholysis product of PLA, serves as a feedstock to LD for the resynthesise of PLA, thereby achieving a closed-loop circular economy for PLA. The fundamental principle of the closed-loop circular economy for PLA is resource efficiency, with this model significantly reducing landfill volumes and decreasing reliance on virgin raw materials. From an economic perspective, it enhances potential cost efficacies by optimizing material life span, whilst increasing resilience against the changes of raw material sourcing.

In this thesis, the circular economy of PLA is explored, centred on the synthesis of LD from MLA, with a number of key objectives:

a. An overview of sustainable plastics: The physical properties of a wide range of plastics are summarised, where the physical properties of PLA are analysed

amongst other plastics. This enables us to understand the application potential of PLA and provides inspiration for the future of PLA.

b. Studies for synthesis of LD from MLA by one-pot liquid-phase transesterification: A comparison of $TiO_x/SiO_2$ and $TiO_2$ catalysts performance by experiments, illustrates the effect of titanium valence and support on the reaction. Moreover, the detailed reaction pathway of MLA to LD with $TiO_x/SiO_2$ catalyst was revealed by DFT method, explained the reaction mechanism at an atomic level.

c. Studies of advancing catalytic performance: the MLA adsorption performance on Ti(III)/Ti(IV)-based catalyst with or without silica support has been analysed. The effect of different valence states of Ti and support in catalyst behaviour is illustrated from the point of view of theoretical calculations, which in turn provides theoretical support for improving catalyst performance.

d. A Techno-economic analysis of the recycling of waste PLA process: a comprehensive techno-economic analysis of five waste PLA recycling scenarios has been processed, combining two feedstocks (LA and MLA) with three process routes with different catalysts: hydrolysis, alcoholysis, and modified alcoholysis. The objective of this analysis is to benchmark the novel alcoholysis pathway against the conventional hydrolysis process and identify the most economically favourable recycling route.

## 1.4 Thesis layout

The layout of the thesis is shown in Figure 1.13:

Chapter 1 introduces the challenges posed by plastic pollution and surveyed the main recycling routes for PLA. Through a comparative assessment, an alcoholysis-centric closed-loop is identified as especially promising, while noting that the critical MLA → LD step still has room for improvement. Accordingly, the one-step conversion of MLA to LD in detail is explored, summarizes the current research gaps, and set out the objectives of this study. Chapter 2 provides a comprehensive overview of the four core methodologies utilized in this research and the DFT theory related to this thesis. It begins with the multi-criteria decision analysis (MCDA) method, overviews the scoring methodology for 17 polymers. Subsequently, it summarises the molecular-level computational methods utilised in the thesis, introducing the design parameters for first principles calculations within this work. It then details the system-level process modelling, outlining the framework for the techno-economic simulations conducted in Aspen Plus. The end of methodology section covers the experimental work, including the materials and instruments used and describing the catalyst synthesis, reactor setup, operating procedures, and product analysis. Finally, the fundamental knowledge of DFT is introduced. Chapter 3 presents a methodical dissection of the physical attributes of plastics. Beyond an overview, this section contrasts the salient features of various polymers, categorically delving into their mechanical, thermal, and chemical properties, with an added environment assessment. This comprehensive evaluation of features of PLA relative to other materials aims to enhance its prospects for future development. Chapter 4 is a thorough examination of the synthesis of LD from MLA via one-pot liquid-phase transesterification, analysing key performance metrics including conversion, selectivity under various operating conditions, characterizing the Ti-based catalysts by experiments. Meanwhile, the reaction pathway was explored via DFT calculations,

elucidating the reaction steps from a mechanistic approach. Chapter 5 is focussed on the deeper catalytic performance analysis by DFT modelling. The adsorption mechanics of MLA on different valence and support Ti-based catalysts surface were explored. Chapter 6, the economics of five waste PLA recycling scenarios is compared, combining two feedstocks (LA and MLA) with three process routes with different catalysts: hydrolysis, alcoholysis, and modified alcoholysis. Chapter 7, the final chapter wraps up the thesis, offering both the core conclusion of the thesis and future research directions.

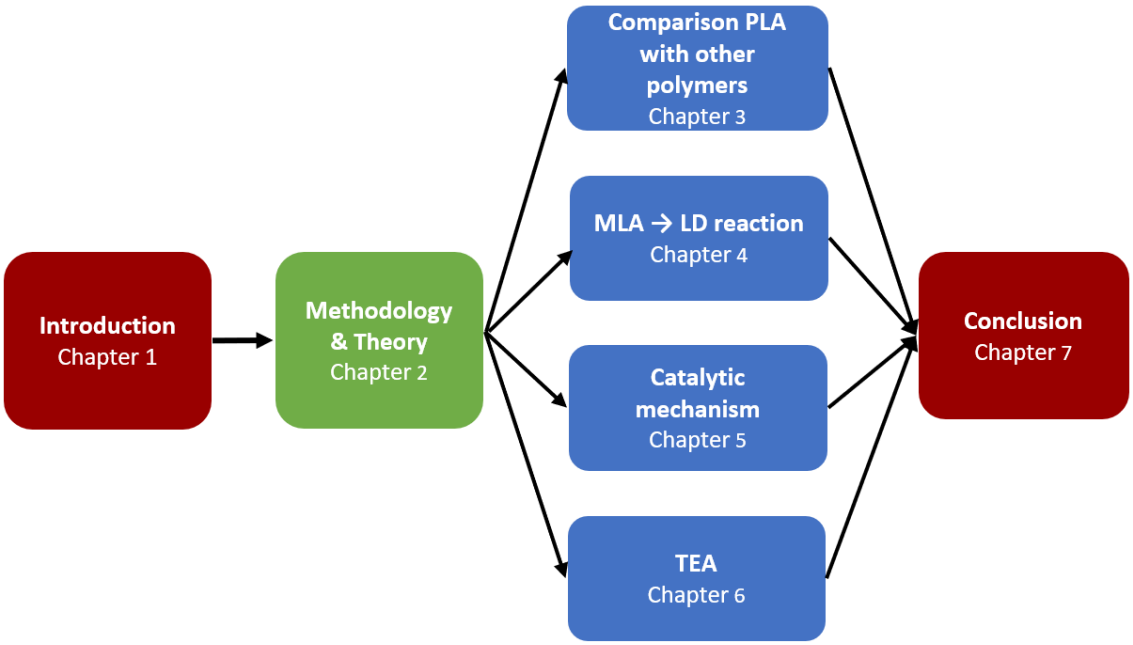


Figure 1.13 Thesis layout

# References

(1) Huck, W. T. S. Polymer Networks Take a Bow. Nature 2011, 472 (7344), 425–426. https://doi.org/10.1038/472425a.

(2) Acharjee, S. A.; Bharali, P.; Gogoi, B.; Sorhie, V.; Walling, B.; Alemtoshi. PHA-Based Bioplastic: A Potential Alternative to Address Microplastic Pollution. Water. Air. Soil Pollut. 2023, 234 (1), 21. https://doi.org/10.1007/s11270-022-06029-2.

(3) Andrady, A. L.; Neal, M. A. Applications and Societal Benefits of Plastics. Philos. Trans. R. Soc. B Biol. Sci. 2009, 364 (1526), 1977–1984. https://doi.org/10.1098/rstb.2008.0304.

(4) Dokl, M.; Copot, A.; Krajnc, D.; Fan, Y. V.; Vujanović, A.; Aviso, K. B.; Tan, R. R.; Kravanja, Z.; Čuček, L. Global Projections of Plastic Use, End-of-Life Fate and Potential Changes in Consumption, Reduction, Recycling and Replacement with Bioplastics to 2050. Sustain. Prod. Consum. 2024, 51, 498–518. https://doi.org/10.1016/j.spc.2024.09.025.

(5) Plastics – the Fast Facts 2024; Plastics Europe AISBL, 2024.

(6) Houssini, K.; Li, J.; Tan, Q. Complexities of the Global Plastics Supply Chain Revealed in a Trade-Linked Material Flow Analysis. Commun. Earth Environ. 2025, 6 (1), 257. https://doi.org/10.1038/s43247-025-02169-5.

(7) Rabnawaz, M.; Wyman, I.; Auras, R.; Cheng, S. A Roadmap towards Green Packaging: The Current Status and Future Outlook for Polyesters in the Packaging Industry. Green Chem 2017, 19 (20), 4737–4753. https://doi.org/10.1039/C7GC02521A.

(8) Walker, T. R.; Fequet, L. Current Trends of Unsustainable Plastic Production and Micro(Nano)Plastic Pollution. TrAC Trends Anal. Chem. 2023, 160, 116984. https://doi.org/10.1016/j.trac.2023.116984.

(9) Geyer, R.; Jambeck, J. R.; Law, K. L. Production, Use, and Fate of All Plastics Ever Made. Sci. Adv. 2017, 3 (7), e1700782. https://doi.org/10.1126/sciadv.1700782.

(10) Naderi Beni, N.; Karimifard, S.; Gilley, J.; Messer, T.; Schmidt, A.; Bartelt-Hunt, S. Higher Concentrations of Microplastics in Runoff from Biosolid-Amended Croplands than Manure-Amended Croplands. Commun. Earth Environ. 2023, 4 (1), 42. https://doi.org/10.1038/s43247-023-00691-y.

(11) de Souza Machado, A. A.; Lau, C. W.; Kloas, W.; Bergmann, J.; Bachelier, J. B.; Faltin, E.; Becker, R.; Görlich, A. S.; Rillig, M. C. Microplastics Can Change Soil Properties and Affect Plant Performance. Environ. Sci. Technol. 2019, 53 (10), 6044–6052. https://doi.org/10.1021/acs.est.9b01339.

(12) Brahney, J.; Hallerud, M.; Heim, E.; Hahnenberger, M.; Sukumaran, S. Plastic Rain in Protected Areas of the United States. Science 2020, 368 (6496), 1257–1260. https://doi.org/10.1126/science.aaz5819.

(13) Jambeck, J. R.; Geyer, R.; Wilcox, C.; Siegler, T. R.; Perryman, M.; Andrady, A.; Narayan, R.; Law, K. L. Plastic Waste Inputs from Land into the Ocean. Science 2015, 347 (6223), 768–771. https://doi.org/10.1126/science.1260352.

(14) Van Wouwe, P.; Dusselier, M.; Vanleeuw, E.; Sels, B. Lactide Synthesis and Chirality Control for Polylactic Acid Production. ChemSusChem 2016, 9 (9), 907–921. https://doi.org/10.1002/cssc.201501695.

(15) Balla, E.; Daniilidis, V.; Karlioti, G.; Kalamas, T.; Stefanidou, M.; Bikiaris, N. D.; Vlachopoulos, A.; Koumentakou, I.; Bikiaris, D. N. Poly(Lactic Acid): A Versatile

Biobased Polymer for the Future with Multifunctional Properties—From Monomer Synthesis, Polymerization Techniques and Molecular Weight Increase to PLA Applications. Polymers 2021, 13 (11), 1822. https://doi.org/10.3390/polym13111822.

(16) Madhavan Nampoothiri, K.; Nair, N. R.; John, R. P. An Overview of the Recent Developments in Polylactide (PLA) Research. Bioresour. Technol. 2010, 101 (22), 8493–8501. https://doi.org/10.1016/j.biortech.2010.05.092.

(17) Nova-Institute. BIOPLASTICS MARKET DEVELOPMENT UPDATE 2024. https://www.european-bioplastics.org/bioplastics-market-development-update-2024/.

(18) Bai, H.; Deng, S.; Bai, D.; Zhang, Q.; Fu, Q. Recent Advances in Processing of Stereocomplex‐Type Polylactide. Macromol. Rapid Commun. 2017, 38 (23), 1700454. https://doi.org/10.1002/marc.201700454.

(19) Capuana, E.; Lopresti, F.; Ceraulo, M.; La Carrubba, V. Poly-l-Lactic Acid (PLLA)-Based Biomaterials for Regenerative Medicine: A Review on Processing and Applications. Polymers 2022, 14 (6), 1153. https://doi.org/10.3390/polym14061153.

(20) Tsuji, H. Poly(Lactic Acid) Stereocomplexes: A Decade of Progress. Adv. Drug Deliv. Rev. 2016, 107, 97–135. https://doi.org/10.1016/j.addr.2016.04.017.

(21) Raef, M.; Sarasua, J.-R.; Etxeberria, A.; Ugartemendia, J. M. Stereocomplexation: From Molecular Structure to Functionality of Advanced Polylactide Systems. Polymer 2023, 280, 126066. https://doi.org/10.1016/j.polymer.2023.126066.

(22) Annunziata, M.; Nastri, L.; Cecoro, G.; Guida, L. The Use of Poly-d,l-Lactic Acid (PDLLA) Devices for Bone Augmentation Techniques: A Systematic Review. Molecules 2017, 22 (12), 2214. https://doi.org/10.3390/molecules22122214.

(23) Okamoto, M.; John, B. Synthetic Biopolymer Nanocomposites for Tissue Engineering Scaffolds. Prog. Polym. Sci. 2013, 38 (10–11), 1487–1503. https://doi.org/10.1016/j.progpolymsci.2013.06.001.

(24) Macnamara, J. F.; Rubino, M.; Daum, M.; Kathuria, A.; Auras, R. Unlocking the Secrets of High-Water Barrier Stereocomplex Polylactide Blend Extrusion Films. Green Chem. 2024, 26 (4), 2248–2257. https://doi.org/10.1039/D3GC04805E.

(25) Casalini, T.; Rossi, F.; Castrovinci, A.; Perale, G. A Perspective on Polylactic Acid-Based Polymers Use for Nanoparticles Synthesis and Applications. Front. Bioeng. Biotechnol. 2019, 7, 259. https://doi.org/10.3389/fbioe.2019.00259.

(26) Farah, S.; Anderson, D. G.; Langer, R. Physical and Mechanical Properties of PLA, and Their Functions in Widespread Applications — A Comprehensive Review. Adv. Drug Deliv. Rev. 2016, 107, 367–392. https://doi.org/10.1016/j.addr.2016.06.012.

(27) Raquez, J.-M.; Habibi, Y.; Murariu, M.; Dubois, P. Polylactide (PLA)-Based Nanocomposites. Prog. Polym. Sci. 2013, 38 (10), 1504–1542. https://doi.org/10.1016/j.progpolymsci.2013.05.014.

(28) Zhang, Z.; Cao, B.; Jiang, N. The Mechanical Properties and Degradation Behavior of 3D-Printed Cellulose Nanofiber/Polylactic Acid Composites. Materials 2023, 16 (18), 6197. https://doi.org/10.3390/ma16186197.

(29) Standau, T.; Zhao, C.; Murillo Castellón, S.; Bonten, C.; Altstädt, V. Chemical Modification and Foam Processing of Polylactide (PLA). Polymers 2019, 11 (2), 306. https://doi.org/10.3390/polym11020306.

(30) Ramezani Dana, H.; Ebrahimi, F. Synthesis, Properties, and Applications of Polylactic acid - based Polymers. Polym. Eng. Sci. 2023, 63 (1), 22 – 43. https://doi.org/10.1002/pen.26193.

(31) Hu, Y.; Daoud, W.; Cheuk, K.; Lin, C. Newly Developed Techniques on Polycondensation, Ring-Opening Polymerization and Polymer Modification: Focus on Poly(Lactic Acid). Materials 2016, 9 (3), 133. https://doi.org/10.3390/ma9030133.

(32) Egiazaryan, T. A.; Makarov, V. M.; Moskalev, M. V.; Razborov, D. A.; Fedushkin, I. L. Synthesis of Lactide from Alkyl Lactates Catalyzed by Lanthanide Salts. Mendeleev Commun. 2019, 29 (6), 648–650. https://doi.org/10.1016/j.mencom.2019.11.014.

(33) Yeh, C.-C.; Chen, C.-N.; Li, Y.-T.; Chang, C.-W.; Cheng, M.-Y.; Chang, H.-I. The Effect of Polymer Molecular Weight and UV Radiation on Physical Properties and Bioactivities of PCL Films. Cell. Polym. 2011, 30 (5), 261–276. https://doi.org/10.1177/026248931103000503.

(34) Dusselier, M.; Van Wouwe, P.; Dewaele, A.; Jacobs, P. A.; Sels, B. F. Shape-Selective Zeolite Catalysis for Bioplastics Production. Science 2015, 349 (6243), 78–80. https://doi.org/10.1126/science.aaa7169.

(35) Kumar, S.; Panda, A. K.; Singh, R. K. A Review on Tertiary Recycling of High-Density Polyethylene to Fuel. Resour. Conserv. Recycl. 2011, 55 (11), 893–910. https://doi.org/10.1016/j.resconrec.2011.05.005.

(36) Waste Framework Directive. https://environment.ec.europa.eu/topics/waste-and-recycling/waste-framework-directive_en.

(37) Fredi, G.; Dorigato, A. Recycling of Bioplastic Waste: A Review. Adv. Ind. Eng. Polym. Res. 2021, 4 (3), 159–177. https://doi.org/10.1016/j.aiepr.2021.06.006.

(38) Bezeraj, E.; Debrie, S.; Arraez, F. J.; Reyes, P.; Van Steenberge, P. H. M.; D'hooge, D. R.; Edeleva, M. State-of-the-Art of Industrial PET Mechanical Recycling: Technologies, Impact of Contamination and Guidelines for Decision-Making. RSC Sustain. 2025, 3 (5), 1996–2047. https://doi.org/10.1039/D4SU00571F.

(39) Lamberti, F. M.; Román-Ramírez, L. A.; Wood, J. Recycling of Bioplastics: Routes and Benefits. J. Polym. Environ. 2020, 28 (10), 2551–2571. https://doi.org/10.1007/s10924-020-01795-8.

(40) Lamberti, F. M. Studies on the Chemical Recycling of Poly(Lactic Acid) via Alcoholysis.

(41) Cosate De Andrade, M. F.; Souza, P. M. S.; Cavalett, O.; Morales, A. R. Life Cycle Assessment of Poly(Lactic Acid) (PLA): Comparison Between Chemical Recycling, Mechanical Recycling and Composting. J. Polym. Environ. 2016, 24 (4), 372–384. https://doi.org/10.1007/s10924-016-0787-2.

(42) Ramos-Hernández, T.; Robledo-Ortíz, J. R.; González-López, M. E.; Del Campo, A. S. M.; González-Núñez, R.; Rodrigue, D.; Pérez Fonseca, A. A. Mechanical Recycling of PLA : Effect of Weathering, Extrusion Cycles, and Chain Extender. J. Appl. Polym. Sci. 2023, 140 (16), e53759. https://doi.org/10.1002/app.53759.

(43) Kassab, A.; Al Nabhani, D.; Mohanty, P.; Pannier, C.; Ayoub, G. Y. Advancing Plastic Recycling: Challenges and Opportunities in the Integration of 3D Printing and Distributed Recycling for a Circular Economy. Polymers 2023, 15 (19), 3881. https://doi.org/10.3390/polym15193881.

(44) Siddiqui, M. N.; Redhwi, H. H.; Al-Arfaj, A. A.; Achilias, D. S. Chemical Recycling of PET in the Presence of the Bio-Based Polymers, PLA, PHB and PEF: A Review. Sustainability 2021, 13 (19), 10528. https://doi.org/10.3390/su131910528.

(45) Bezeraj, E.; Debrie, S.; Arraez, F. J.; Reyes, P.; Van Steenberge, P. H. M.; D'hooge, D. R.; Edeleva, M. State-of-the-Art of Industrial PET Mechanical Recycling: Technologies, Impact of Contamination and Guidelines for Decision-Making. RSC Sustain. 2025, 3 (5), 1996–2047. https://doi.org/10.1039/D4SU00571F.

(46) Li, H.; Brown, J. L.; Cecon, V. S.; Curley, J. B.; Kim, M. S.; Mark, L. O.; Mavrikakis, M.; others; Huber, G. W. Expanding Plastics Recycling Technologies: Chemical Aspects, Technology Status and Challenges. Green Chem. 2022, 24, 8899–9002. https://doi.org/10.1039/D2GC02588D.

(47) Ügdüler, S.; Laere, T. V.; Somer, T. D.; Gusev, S.; Geem, K. M. V.; Kulawig, A.; Leineweber, R.; Defoin, M.; den Bergen, H. V.; Bontinck, D.; Meester, S. D. Understanding the Complexity of Deinking Plastic Waste: An Assessment of the Efficiency of Different Treatments to Remove Ink Resins from Printed Plastic Film. J. Hazard. Mater. 2023, 452, 131239. https://doi.org/10.1016/j.jhazmat.2023.131239.

(48) Strangl, M.; Lok, B.; Breunig, P.; Ortner, E.; Buettner, A. The Challenge of Deodorizing Post-Consumer Polypropylene Packaging: Screening of the Effect of Washing, Color-Sorting and Heat Exposure. Resour. Conserv. Recycl. 2021, 164, 105143. https://doi.org/10.1016/j.resconrec.2020.105143.

(49) Lase, I. S.; Bashirgonbadi, A.; van Rhijn, F.; Dewulf, J.; Ragaert, K.; Delva, L.; Roosen, M.; Brandsma, M.; Langen, M.; Meester, S. D. Material Flow Analysis and Recycling Performance of an Improved Mechanical Recycling Process for Post-Consumer Flexible Plastics. Waste Manag. 2022, 249–263. https://doi.org/10.1016/j.wasman.2022.09.002.

(50) Guo, J.; Luo, C.; Wittkowski, C.; Fehr, I.; Chong, Z.; Kitzberger, M.; Alassali, A.; Zhao, X.; Leineweber, R.; Feng, Y.; Kuchta, K. Screening the Impact of Surfactants and

Reaction Conditions on the De-Inkability of Different Printing Ink Systems for Plastic Packaging. Polymers 2023, 15 (9), 2220. https://doi.org/10.3390/polym15092220.

(51) Otten, M.; Gregory, E.; Elshof, M.; Walgreen, M.; van Essen, H. PLA Sorting for Recycling: Experiments Performed at the National Test Centre Circular Plastics (NTCP); CE Delft: Delft, The Netherlands, 2021. https://cedelft.eu/publications/pla-sorting-for-recycling/.

(52) RecyClass Washing Quick Test Procedure for Paper Labels Applied on PE and PP Films (v1.0), 2022. https://recyclass.eu/wp-content/uploads/2022/11/RecyClass-Washing-QT-Procedure-for-Paper-Labels-applied-on-PE-and-PP-Films-v1.0.pdf.

(53) The Science behind Recyclability, 2024. https://recyclass.eu/wp-content/uploads/2024/05/240522_Science-behind-Recyclability__Presentation.pdf.

(54) Roosen, M.; Harinck, L.; Ügdüler, S.; Somer, T. D.; Hucks, A.-G.; Belé, T. G. A.; Buettner, A.; Ragaert, K.; Geem, K. V.; Dumoulin, A.; Meester, S. D. Deodorization of Post-Consumer Plastic Waste Fractions: A Comparison of Different Washing Media. Sci. Total Environ. 2022, 812, 152467. https://doi.org/10.1016/j.scitotenv.2021.152467.

(55) Genuino, H. C.; Ruiz, M. P.; Heeres, H. J.; Kersten, S. R. A. Pyrolysis of Mixed Plastic Waste (DKR-350): Effect of Washing Pre-Treatment and Fate of Chlorine. Fuel Process. Technol. 2022, 233, 107304. https://doi.org/10.1016/j.fuproc.2022.107304.

(56) Beltrán, F. R.; Lorenzo, V.; Acosta, J.; de la Orden, M. U.; Martínez Urreaga, J. Effect of Simulated Mechanical Recycling Processes on the Structure and Properties of Poly(Lactic Acid). J. Environ. Manage. 2018, 216, 25–31. https://doi.org/10.1016/j.jenvman.2017.05.020.

(57) NatureWorks LLC. Ingeo Biopolymer 3052D Technical Data Sheet: Injection Molding Process Guide; manual; NatureWorks LLC: Minnetonka, MN, USA, 2015. https://www.natureworksllc.com/~/media/Technical_Resources/Technical_Data_Sheets/TechnicalDataSheet_3052D_injection-molding_pdf.pdf.

(58) Milovanovic, S.; Pajnik, J.; Lukic, I. Tailoring of Advanced Poly(Lactic Acid)‐based Materials: A Review. J. Appl. Polym. Sci. 2022, 139 (12), 51839. https://doi.org/10.1002/app.51839.

(59) Agbakoba, V. C.; Webb, N.; Jegede, E.; Phillips, R.; Hlangothi, S. P.; John, M. J. Mechanical Recycling of Waste PLA Generated From 3D Printing Activities: Filament Production and Thermomechanical Analysis. Macromol. Mater. Eng. 2024, 309 (8), 2300276. https://doi.org/10.1002/mame.202300276.

(60) NatureWorks LLC. Sheet Extrusion Processing Guide; manual; NatureWorks LLC: Minnetonka, MN, USA, 2015. https://www.natureworksllc.com/~/media/Technical_Resources/Processing_Guides/ProcessingGuide_Sheet-Extrusion_pdf.pdf.

(61) Lamtai, A.; Elkoun, S.; Robert, M.; Mighri, F.; Diez, C. Mechanical Recycling of Thermoplastics: A Review of Key Issues. Waste 2023, 1 (4), 860–883. https://doi.org/10.3390/waste1040050.

(62) Carrasco, F.; Cailloux, J.; Sánchez-Jiménez, P. E.; Maspoch, M. Ll. Improvement of the Thermal Stability of Branched Poly(Lactic Acid) Obtained by Reactive Extrusion. Polym. Degrad. Stab. 2014, 104, 40–49. https://doi.org/10.1016/j.polymdegradstab.2014.03.026.

(63) COLLIN Lab & Pilot Solutions GmbH. Strand Pelletizers – cutting of plastomer strands. https://www.collin-solutions.com/en/product/strand-pelletizers/.

(64) Bay Plastics Machinery. Bay Plastics Machinery: Product Training Presentation (Pelletizing Basics); manual; 2014. https://bayplasticsmachinery.com/wp-content/uploads/2015/11/BPM-Training.pdf.

(65) MAAG Group. Micropellet Technology; manual; 2017. https://maag.com/wp-content/uploads/Micropellet_Gala_2S_EN_s.pdf.

(66) Davis-Standard, LLC. Underwater Pelletizers Model 3.5 / 3.5X Pelletor®; manual; 2020. https://davis-standard.com/DS_wordpress/wp-content/uploads/2020/03/PELLETIZING_Underwater-Pelletizers-3.5-3.5X_EN.pdf.

(67) ips Intelligent Pelletizing Solutions. Ips-SGU Strand Pelletizer Brochure; manual; 2020. https://pelletizing.de/images/pdf/EN_SGU_4s_2020_final.pdf.

(68) Jafari, A.; Saljooghi Nezhad, V. Employing DEM to Study the Impact of Different Parameters on the Screening Efficiency and Mesh Wear. Powder Technol. 2016, 297, 126–143. https://doi.org/10.1016/j.powtec.2016.04.008.

(69) Backes, E.; Pires, L.; Costa, L.; Passador, F.; Pessan, L. Analysis of the Degradation During Melt Processing of PLA/Biosilicate® Composites. J. Compos. Sci. 2019, 3 (2), 52. https://doi.org/10.3390/jcs3020052.

(70) Aliotta, L.; Sciara, L. M.; Cinelli, P.; Canesi, I.; Lazzeri, A. Improvement of the PLA Crystallinity and Heat Distortion Temperature Optimizing the Content of Nucleating Agents and the Injection Molding Cycle Time. Polymers 2022, 14 (5), 977. https://doi.org/10.3390/polym14050977.

(71) Nagarajan, V.; Zhang, K.; Misra, M.; Mohanty, A. K. Overcoming the Fundamental Challenges in Improving the Impact Strength and Crystallinity of PLA Biocomposites: Influence of Nucleating Agent and Mold Temperature. ACS Appl. Mater. Interfaces 2015, 7 (21), 11203–11214. https://doi.org/10.1021/acsami.5b01145.

(72) Zhao, P.; Rao, C.; Gu, F.; Sharmin, N.; Fu, J. Close-Looped Recycling of Polylactic Acid Used in 3D Printing: An Experimental Investigation and Life Cycle Assessment. J. Clean. Prod. 2018, 197, 1046–1055. https://doi.org/10.1016/j.jclepro.2018.06.275.

(73) Pillin, I.; Montrelay, N.; Bourmaud, A.; Grohens, Y. Effect of Thermo-Mechanical Cycles on the Physico-Chemical Properties of Poly(Lactic Acid). Polym. Degrad. Stab. 2008, 93 (2), 321–328. https://doi.org/10.1016/j.polymdegradstab.2007.12.005.

(74) Żenkiewicz, M.; Richert, J.; Rytlewski, P.; Moraczewski, K.; Stepczyńska, M.; Karasiewicz, T. Characterisation of Multi-Extruded Poly(Lactic Acid). Polym. Test. 2009, 28 (4), 412–418. https://doi.org/10.1016/j.polymertesting.2009.01.012.

(75) Pillin, I.; Montrelay, N.; Bourmaud, A.; Grohens, Y. Effect of Thermo-Mechanical Cycles on the Physico-Chemical Properties of Poly(Lactic Acid). Polym. Degrad. Stab. 2008, 93 (2), 321–328. https://doi.org/10.1016/j.polymdegradstab.2007.12.005.

(76) Cosate de Andrade, M. F.; Fonseca, G.; Morales, A. R.; Mei, L. H. I. Mechanical Recycling Simulation of Polylactide Using a Chain Extender. Adv. Polym. Technol. 2018, 37 (6), 2053–2060. https://doi.org/10.1002/adv.21863.

(77) Qi, X.; Ren, Y.; Wang, X. New Advances in the Biodegradation of Poly(Lactic) Acid. Int. Biodeterior. Biodegrad. 2017, 117, 215–223. https://doi.org/10.1016/j.ibiod.2017.01.010.

(78) Soo, X. Y. D.; Jia, L.; Lim, Q. F.; Chua, M. H.; Wang, S.; Hui, H. K.; See, J. M. R.; Chen, Y.; Li, J.; Wei, F.; Tomczak, N.; Kong, J.; Loh, X. J.; Fei, X.; Zhu, Q. Hydrolytic Degradation and Biodegradation of Polylactic Acid Electrospun Fibers. Chemosphere 2024, 350, 141186. https://doi.org/10.1016/j.chemosphere.2024.141186.

(79) Haider, T. P.; Völker, C.; Kramm, J.; Landfester, K.; Wurm, F. R. Plastics of the Future? The Impact of Biodegradable Polymers on the Environment and on Society. Angew. Chem. Int. Ed. 2019, 58 (1), 50–62. https://doi.org/10.1002/anie.201805766.

(80) Yagi, H.; Ninomiya, F.; Funabashi, M.; Kunioka, M. Anaerobic Biodegradation Tests of Poly(Lactic Acid) under Mesophilic and Thermophilic Conditions Using a New Evaluation System for Methane Fermentation in Anaerobic Sludge. Int. J. Mol. Sci. 2009, 10 (9), 3824–3835. https://doi.org/10.3390/ijms10093824.

(81) Nakamura, K.; Tomita, T.; Abe, N.; Kamio, Y. Purification and Characterization of an Extracellular Poly( l -Lactic Acid) Depolymerase from a Soil Isolate, Amycolatopsis Sp. Strain K104-1. Appl. Environ. Microbiol. 2001, 67 (1), 345–353. https://doi.org/10.1128/AEM.67.1.345-353.2001.

(82) Qi, X.; Ren, Y.; Wang, X. New Advances in the Biodegradation of Poly(Lactic) Acid. Int. Biodeterior. Biodegrad. 2017, 117, 215–223. https://doi.org/10.1016/j.ibiod.2017.01.010.

(83) Huang, Q.; Hiyama, M.; Kabe, T.; Kimura, S.; Iwata, T. Enzymatic Self-Biodegradation of Poly( l -Lactic Acid) Films by Embedded Heat-Treated and Immobilized Proteinase K. Biomacromolecules 2020, 21 (8), 3301–3307. https://doi.org/10.1021/acs.biomac.0c00759.

(84) McNeill, I. C.; Leiper, H. A. Degradation Studies of Some Polyesters and Polycarbonates—1. Polylactide: General Features of the Degradation under Programmed Heating Conditions. Polym. Degrad. Stab. 1985, 11 (3), 267–285. https://doi.org/10.1016/0141-3910(85)90050-3.

(85) McNeill, I. C.; Leiper, H. A. Degradation Studies of Some Polyesters and Polycarbonates—2. Polylactide: Degradation under Isothermal Conditions, Thermal Degradation Mechanism and Photolysis of the Polymer. Polym. Degrad. Stab. 1985, 11 (4), 309–326. https://doi.org/10.1016/0141-3910(85)90035-7.

(86) Kaya, H.; Hacaloglu, J. Thermal Degradation of Polylactide/Aluminium Diethylphosphinate. J. Anal. Appl. Pyrolysis 2014, 110, 155–162. https://doi.org/10.1016/j.jaap.2014.08.015.

(87) Nishida, H.; Mori, T.; Hoshihara, S.; Fan, Y.; Shirai, Y.; Endo, T. Effect of Tin on Poly(l-Lactic Acid) Pyrolysis. Polym. Degrad. Stab. 2003, 81 (3), 515–523. https://doi.org/10.1016/S0141-3910(03)00152-6.

(88) Mori, T.; Nishida, H.; Shirai, Y.; Endo, T. Effects of Chain End Structures on Pyrolysis of Poly(l-Lactic Acid) Containing Tin Atoms. Polym. Degrad. Stab. 2004, 84 (2), 243–251. https://doi.org/10.1016/j.polymdegradstab.2003.11.008.

(89) Fan, Y.; Nishida, H.; Hoshihara, S.; Shirai, Y.; Tokiwa, Y.; Endo, T. Pyrolysis Kinetics of Poly(l-Lactide) with Carboxyl and Calcium Salt End Structures. Polym. Degrad. Stab. 2003, 79 (3), 547–562. https://doi.org/10.1016/S0141-3910(02)00374-9.

(90) Fan, Y.; Nishida, H.; Mori, T.; Shirai, Y.; Endo, T. Thermal Degradation of Poly(l-Lactide): Effect of Alkali Earth Metal Oxides for Selective l,l-Lactide Formation. Polymer 2004, 45 (4), 1197–1205. https://doi.org/10.1016/j.polymer.2003.12.058.

(91) Piemonte, V.; Gironi, F. Kinetics of Hydrolytic Degradation of PLA. J. Polym. Environ. 2013, 21 (2), 313–318. https://doi.org/10.1007/s10924-012-0547-x.

(92) Rodriguez, E. J.; Marcos, B.; Huneault, M. A. Hydrolysis of Polylactide in Aqueous Media. J. Appl. Polym. Sci. 2016, 133 (44), app.44152. https://doi.org/10.1002/app.44152.

(93) Burkersroda, F. von; Schedl, L.; Göpferich, A. Why Degradable Polymers Undergo Surface Erosion or Bulk Erosion. Biomaterials 2002, 23 (21), 4221–4231. https://doi.org/10.1016/S0142-9612(02)00170-9.

(94) Gorrasi, G.; Pantani, R. Hydrolysis and Biodegradation of Poly(Lactic Acid). In Synthesis, Structure and Properties of Poly(lactic acid); Di Lorenzo, M. L., Androsch, R., Eds.; Springer International Publishing: Cham, 2018; pp 119–151. https://doi.org/10.1007/12_2016_12.

(95) McKeown, P.; Jones, M. D. The Chemical Recycling of PLA: A Review. Sustain. Chem. 2020, 1 (1), 1–22. https://doi.org/10.3390/suschem1010001.

(96) Jong, S. J. de; Arias, E. R.; Rijkers, D. T. S.; Nostrum, C. F. van; Bosch, J. J. K. den; Hennink, W. E. New Insights into the Hydrolytic Degradation of Poly(Lactic Acid): Participation of the Alcohol Terminus. Polymer 2001, 42 (7), 2795–2802. https://doi.org/10.1016/S0032-3861(00)00646-7.

(97) Tsuji, H.; Ikada, Y. Properties and Morphology of Poly(L-Lactide). II. Hydrolysis in Alkaline Solution. J. Polym. Sci. Part Polym. Chem. 1998, 36 (1), 59–66.

https://doi.org/10.1002/(SICI)1099-0518(19980115)36:1%253C59::AID-POLA9%253E3.0.CO;2-X.

(98) Piemonte, V.; Sabatini, S.; Gironi, F. Chemical Recycling of PLA: A Great Opportunity Towards the Sustainable Development? J. Polym. Environ. 2013, 21 (3), 640–647. https://doi.org/10.1007/s10924-013-0608-9.

(99) Jehanno, C.; Pérez-Madrigal, M. M.; Demarteau, J.; Sardon, H.; Dove, A. P. Organocatalysis for Depolymerisation. Polym. Chem. 2019, 10 (2), 172–186. https://doi.org/10.1039/C8PY01284A.

(100) McKeown, P.; Jones, M. D. The Chemical Recycling of PLA: A Review. Sustain. Chem. 2020, 1 (1), 1–22. https://doi.org/10.3390/suschem1010001.

(101) Lamberti, F. M.; Román-Ramírez, L. A.; Dove, A. P.; Wood, J. Methanolysis of Poly(Lactic Acid) Using Catalyst Mixtures and the Kinetics of Methyl Lactate Production. Polymers 2022, 14 (9), 1763. https://doi.org/10.3390/polym14091763.

(102) Song, X.; Wang, H.; Zheng, X.; Liu, F.; Yu, S. Methanolysis of Poly(Lactic Acid) Using Acidic Functionalized Ionic Liquids as Catalysts. J. Appl. Polym. Sci. 2014, 131 (20), 40817. https://doi.org/10.1002/app.40817.

(103) Román-Ramírez, L. A.; McKeown, P.; Jones, M. D.; Wood, J. Poly(Lactic Acid) Degradation into Methyl Lactate Catalyzed by a Well-Defined Zn(II) Complex. ACS Catal. 2019, 9 (1), 409–416. https://doi.org/10.1021/acscatal.8b04863.

(104) Lamberti, F. M.; Ingram, A.; Wood, J. Synergistic Dual Catalytic System and Kinetics for the Alcoholysis of Poly(Lactic Acid). Processes 2021, 9 (6), 921. https://doi.org/10.3390/pr9060921.

(105) Liu, H.; Song, X.; Liu, F.; Liu, S.; Yu, S. Ferric Chloride as an Efficient and Reusable Catalyst for Methanolysis of Poly(Lactic Acid) Waste. J. Polym. Res. 2015, 22 (1), 135. https://doi.org/10.1007/s10965-015-0783-6.

(106) Bian, Z.; Song, X.; Hui, Y.; Wang, H.; Liu, F.; Yu, S. Zn-Acetate-Containing Ionic Liquid as Highly Active Catalyst for Fast and Mild Methanolysis of Poly(Lactic Acid). Polym. Degrad. Stab. 2019, 168, 108937. https://doi.org/10.1016/j.polymdegradstab.2019.108937.

(107) Román-Ramírez, L. A.; Mckeown, P.; Jones, M. D.; Wood, J. Poly(Lactic Acid) Degradation into Methyl Lactate Catalyzed by a Well-Defined Zn(II) Complex. ACS Catal. 2019, 9 (1), 409–416. https://doi.org/10.1021/acscatal.8b04863.

(108) Lamberti, F.; Román-Ramírez, L.; Mckeown, P.; Jones, M.; Wood, J. Kinetics of Alkyl Lactate Formation from the Alcoholysis of Poly(Lactic Acid). Processes 2020, 8 (6), 738. https://doi.org/10.3390/pr8060738.

(109) Song, X.; Bian, Z.; Hui, Y.; Wang, H.; Liu, F.; Yu, S. Zn-Acetate-Containing Ionic Liquid as Highly Active Catalyst for Fast and Mild Methanolysis of Poly(Lactic Acid). Polym. Degrad. Stab. 2019, 168, 108937. https://doi.org/10.1016/j.polymdegradstab.2019.108937.

(110) Song, X.; Zhang, X.; Wang, H.; Liu, F.; Yu, S.; Liu, S. Methanolysis of Poly(Lactic Acid) (PLA) Catalyzed by Ionic Liquids. Polym. Degrad. Stab. 2013, 98 (12), 2760–2764. https://doi.org/10.1016/j.polymdegradstab.2013.10.012.

(111) Clercq, R.; Dusselier, M.; Makshina, E.; Sels, B. F. Catalytic Gas-Phase Production of Lactide from Renewable Alkyl Lactates. Angew. Chem. Int. Ed. 2018, 57 (12), 3074–3078. https://doi.org/10.1002/anie.201711446.

(112) Piemonte, V.; Gironi, F. Lactic Acid Production by Hydrolysis of Poly(Lactic Acid) in Aqueous Solutions: An Experimental and Kinetic Study. J. Polym. Environ. 2013, 21 (1), 275–279. https://doi.org/10.1007/s10924-012-0468-8.

(113) Song, X.; Zhang, X.; Wang, H.; Liu, F.; Yu, S.; Liu, S. Methanolysis of Poly(Lactic Acid) (PLA) Catalyzed by Ionic Liquids. Polym. Degrad. Stab. 2013, 98 (12), 2760–2764. https://doi.org/10.1016/j.polymdegradstab.2013.10.012.

(114) Zou, H.; Yi, C.; Wang, L.; Liu, H.; Xu, W. Thermal Degradation of Poly(Lactic Acid) Measured by Thermogravimetry Coupled to Fourier Transform Infrared Spectroscopy. J. Therm. Anal. Calorim. 2009, 97 (3), 929–935. https://doi.org/10.1007/s10973-009-0121-5.

(115) Feng, L.; Chen, X.; Sun, B.; Bian, X. Water-Catalyzed Racemisation of Lactide. Polym. Degrad. Stab. 2011, 96 (10), 1745–1750. https://doi.org/10.1016/j.polymdegradstab.2011.07.024.

(116) Tsukegi, T.; Motoyama, T.; Shirai, Y. Racemization Behavior of L,L-Lactide during Heating. Polym. Degrad. Stab. 2007, 92 (4), 552–559. https://doi.org/10.1016/j.polymdegradstab.2007.01.009.

(117) Mezzasalma, L.; Dove, A. P.; Coulembier, O. Organocatalytic Ring-Opening Polymerization of L-Lactide in Bulk: A Long Standing Challenge. Eur. Polym. J. 2017, 95, 628–634. https://doi.org/10.1016/j.eurpolymj.2017.05.013.

(118) De Clercq, R.; Dusselier, M.; Poleunis, C.; Debecker, D. P.; Giebeler, L.; Oswald, S.; Makshina, E.; Sels, B. F. Titania-Silica Catalysts for Lactide Production from Renewable Alkyl Lactates: Structure–Activity Relations. ACS Catal. 2018, 8 (9), 8130–8139. https://doi.org/10.1021/acscatal.8b02216.

(119) Heo, S.; Park, H. W.; Lee, J. H.; Chang, Y. K. Design and Evaluation of Sustainable Lactide Production Process with an One-Step Gas Phase Synthesis Route. ACS Sustain. Chem. Eng. 2019, 7 (6), 6178–6184. https://doi.org/10.1021/acssuschemeng.8b06383.

(120) Capel-Sanchez, M. C.; Blanco-Brieva, G.; Campos-Martin, J. M.; de Frutos, M. P.; Wen, W.; Rodriguez, J. A.; Fierro, J. L. G. Grafting Strategy to Develop Single Site Titanium on an Amorphous Silica Surface. Langmuir 2009, 25 (12), 7148–7155. https://doi.org/10.1021/la900578u.

(121) Capel-Sanchez, M. C.; dela Peña-O'Shea, V. A.; Barrio, L.; Campos-Martin, J. M.; Fierro, J. L. G. TD-DFT Analysis of the Electronic Spectra of Ti-Containing Catalysts. Top. Catal. 2006, 41 (1–4), 27–34. https://doi.org/10.1007/s11244-006-0091-9.

(122) Saputera, W. H.; Tan, T. H.; Lovell, E. C.; Rawal, A.; Aguey-Zinsou, K.-F.; Friedmann, D.; Amal, R.; Scott, J. A. Modulating Catalytic Oxygen Activation over Pt–TiO 2 /SiO 2 Catalysts by Defect Engineering of a TiO 2 /SiO 2 Support. Catal. Sci. Technol. 2022, 12 (4), 1049–1059. https://doi.org/10.1039/D1CY02037D.

(123) Voisin, H.; Falourd, X.; Rivard, C.; Capron, I. Versatile Nanocellulose-Anatase TiO2 Hybrid Nanoparticles in Pickering Emulsions for the Photocatalytic Degradation of Organic and Aqueous Dyes. JCIS Open 2021, 3, 100014. https://doi.org/10.1016/j.jciso.2021.100014.

(124) Bessa, M. J.; Costa, C.; Reinosa, J.; Pereira, C.; Fraga, S.; Fernández, J.; Bañares, M. A.; Teixeira, J. P. Moving into Advanced Nanomaterials. Toxicity of Rutile TiO2 Nanoparticles Immobilized in Nanokaolin Nanocomposites on HepG2 Cell Line. Toxicol. Appl. Pharmacol. 2017, 316, 114–122. https://doi.org/10.1016/j.taap.2016.12.018.

(125) Chen, X.; Liu, L.; Liu, Z.; Marcus, M. A.; Wang, W.-C.; Oyler, N. A.; Grass, M. E.; Mao, B.; Glans, P.-A.; Yu, P. Y.; Guo, J.; Mao, S. S. Properties of Disorder-Engineered Black Titanium Dioxide Nanoparticles through Hydrogenation. Sci. Rep. 2013, 3 (1), 1510. https://doi.org/10.1038/srep01510.

(126) Iwaszuk, A.; Nolan, M.; Jin, Q.; Fujishima, M.; Tada, H. Origin of the Visible-Light Response of Nickel(II) Oxide Cluster Surface Modified Titanium(IV) Dioxide. J. Phys. Chem. C 2013, 117 (6), 2709–2718. https://doi.org/10.1021/jp306793r.

(127) Praserthdam, S.; Rittiruam, M.; Maungthong, K.; Saelee, T.; Somdee, S.; Praserthdam, P. Performance Controlled via Surface Oxygen-Vacancy in Ti-Based Oxide Catalyst during Methyl Oleate Epoxidation. Sci. Rep. 2020, 10 (1), 18952. https://doi.org/10.1038/s41598-020-76094-2.

(128) Sarafraz, M.; Sadeghi, M.; Yazdanbakhsh, A.; Amini, M. M.; Sadani, M.; Eslami, A. Enhanced Photocatalytic Degradation of Ciprofloxacin by Black Ti3+/N-TiO2 under Visible LED Light Irradiation: Kinetic, Energy Consumption, Degradation Pathway, and Toxicity Assessment. Process Saf. Environ. Prot. 2020, 137, 261–272. https://doi.org/10.1016/j.psep.2020.02.030.

(129) Tanjung, F. A.; Arifin, Y.; Husseinsyah, S. Enzymatic Degradation of Coconut Shell Powder–Reinforced Polylactic Acid Biocomposites. J. Thermoplast. Compos. Mater. 2020, 33 (6), 800–816. https://doi.org/10.1177/0892705718811895.

# Chapter 2

# Methodology and Theory

Chapter 2 outlines the principal methodologies and theoretical foundations of this thesis. The methodological component comprises multi-criteria decision analysis (MCDA), density functional theory (DFT), experimental studies, and techno-economic analysis (TEA). MCDA evaluates the performance and sustainability of polylactic acid (PLA) with other polymers. By integrating experimental data and DFT modelling, researchers can obtain a general view of the catalytic process from methyl lactate (MLA) to lactide (LD). TEA constructs on experimental data and DFT-derived reaction mechanisms can enable the scale-up and optimization of PLA circularity economy. The theory section focuses on the principles of DFT.

## 2.1 Methodology

The methodology comprises four components: MCDA, DFT, experiments, and TEA. The process flow of the thesis methodology is shown in Figure 2.1. MCDA is employed to evaluate polylactic acid (PLA) with other representative polymers, clarifying strengths and weaknesses of PLA. Subsequently, DFT calculations are performed to investigate the reaction mechanism, together with targeted experiments to compare catalytic performance. Computational results and experimental observations cross-validate one another, providing deeper insight into differences in reaction pathways and catalyst behaviour. Finally, a TEA is conducted: process simulations further bridge fundamental understanding and practical implementation. Process models parameterized by experimental data and DFT mechanisms identify key design parameters, predict product yields, and assess the techno-economic feasibility of the proposed catalytic recycling strategies, thereby guiding the development of industrially viable closed-loop recycling technologies for PLA.

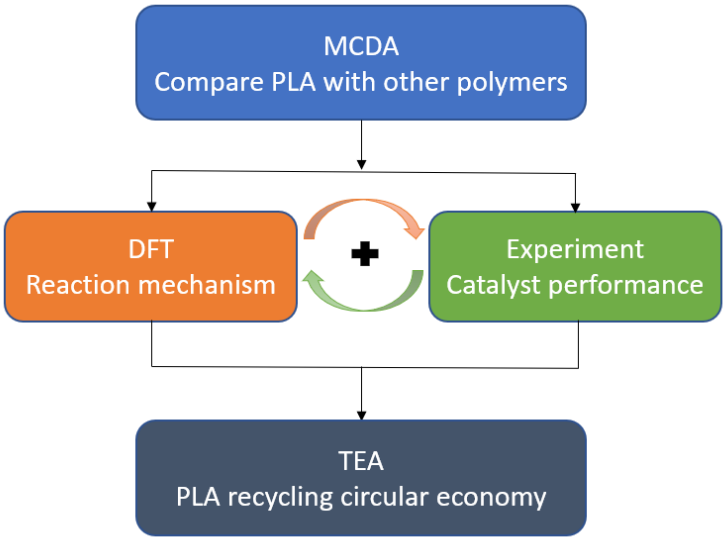


Figure 2.1 Process Flow of the Thesis Methodology.

### 2.1.1 Overall MCDA methods

This subsection presents the overall MCDA framework employed to evaluate seventeen polymers spanning fossil-based and bio-based classes. The material set covers major application domains (packaging, consumer goods, and medical uses). The complete list of polymers and representative applications is provided in Chapter 3 (Table 3.1). Section 2.2.1 primarily describes the decision logic and scoring rules.

The indicator system balances performance and sustainability within a unified comparative scheme. Mechanical properties include tensile strength, elongation at break, Young's modulus, and flexural modulus. Thermal behaviour is represented by melting temperature (Tm) and glass transition temperature (Tg). Chemical and environmental resistance is captured through water absorption and resistance to weak acids, weak alkalis, and UV exposure. Environmental indicators have been derived from life cycle assessment (LCA), namely $CO_2$ emissions, energy use, and mechanical recyclability, quantify the footprint and end-of-life potential. To ensure baseline fitness for use, three gatekeeper criteria, tensile strength, elongation at break, and melting temperature, which are defined as minimum viability checks against breakage and softening under expected conditions; the remaining indicators provide discriminatory power for ranking and application matching rather than pass or fail screening.

Evidence was assembled through a structured literature review and harmonised before analysis. Reported values were converted to consistent units and compiled into an evaluation matrix. Where sources provided ranges, the mid-point was adopted as a representative value to avoid bias from outliers or atypical test conditions. In a small number of cases, conservative substitutions were introduced to manage data gaps while

preserving comparability. Where bio-based polymers lacked itemised resistance to each medium but reported an overall chemical resistance ranking, that overall ranking was used to define the score. All substitutions and limitations are flagged in the compiled tables in Chapter 3, and items of concern are highlighted to signal uncertainty or restricted applicability.

To place heterogeneous evidence on a common scale, all quantitative indicators were discretised to a five-point scoring scheme. For each metric, the observed span across the candidate set was partitioned into five equal intervals, with scores assigned from five to one in descending order of desirability. Directionality was handled explicitly: higher is better metrics (e.g., tensile strength and Tm) map directly to higher scores, whereas lower is better metrics (e.g., $CO_2$ emissions, energy use, and water absorption) are inversely mapped. Qualitative indicators were converted via mapping to the same five-point scale to preserve the relative ordering implied by the literature. For readability and rapid screening, descriptive labels such as “excellent,” “good,” “fair,” and “poor” accompany the numerical scores in the decision matrix, and materials that trigger suitability concerns for a given criterion are visually emphasised.

The MCDA process yields a decision matrix that reports, for each polymer, its five-point scores across all indicators, with gatekeeper properties presented prominently to facilitate immediate checks of fundamental viability. Aggregation for overall ranking is then performed by combining the discretised scores across materials, the precise aggregation rule, any weighting choices, and tie-breaking conventions are specified and justified in Chapter 3 (Table 3.2). The principal outputs include per-material performance profiles, an overall ranking, and compliance assessment against the gatekeeper thresholds.

Overall, the MCDA framework integrates sustainability evidence into a clear comparison, traceable comparison suitable for material assessment, while allowing each decision to be linked back to the underlying evidence presented in Chapter 3.

## 2.1.2 Overall Experimental methods

All experiments were designed to evaluate the catalytic performance of MLA to LD under controlled batch conditions. Titania-silica materials were synthesized by wet impregnation and subsequent thermal treatment, while commercial anatase $TiO_2$ was employed as a reference. Liquid-phase transesterification was conducted in a nitrogen environment and a product-capture setup to keep out moisture and retain volatile products for quantification. Reaction mixtures and trapped condensable were analyzed by gas chromatography-mass spectrometry (GC–MS) for identification and gas chromatography flame ionization detector (GC–FID) for quantification. Catalyst structure were characterized by a suite of techniques (the powder X-ray diffraction (XRD), scanning electron microscopy (SEM) / transmission electron microscopy (TEM), scanning transmission electron microscopy with energy-dispersive X-ray spectroscopy (STEM-EDS) mapping, X-ray photoelectron spectroscopy (XPS), $N_2$ physisorption, and FT-IR spectrum), providing a consistent basis for comparing activity and selectivity across catalysts.

## *Materials*

$SiO_2$ gel (Thermo Scientific Chemicals; BET surface area 350–400 $m^2/g$) was used as the support. Titanium isopropoxide (TTIP) and 2-propanol (percent purity >99.7%) served as the precursor and solvent for impregnation, respectively. Anatase $TiO_2$ powder (percent purity >98%, Thermo Scientific Chemicals) was used

as a reference catalyst. MLA (97 %) was used as the reactant. Dichloromethane (DCM) and o-xylene (99 %, internal standard) were used for product collection and quantification. High-purity nitrogen was employed for drying, inerting, and calcination steps.

## *Synthesis of Catalysts*

Titania-silica catalysts were prepared by wet impregnation[1], the impregnation step set-up is shown in Figure 2.2. The $SiO_2$ gel was first dried at 100 °C (overnight). An impregnation solution was prepared by adding titanium isopropoxide (TTIP) (354 mg for a 3 wt % Ti target in a 2 g batch) dropwise to 2-propanol (20 mL) under $N_2$ and stirring for 1 h. Dried $SiO_2$ (1.9 g) was then introduced into the precursor solution under $N_2$ and stirred for 4 h. Solvent was removed on a rotary evaporator at 50 °C under vacuum, and the recovered solid was dried at 80 °C for 10 h. The powder was finally calcined under flowing $N_2$ at 500 °C for 4 h (10 °C $min^{-1}$ ramp). The commercial $TiO_2$ reference (anatase) was dried in an oven for 10 h prior to use to remove moisture.

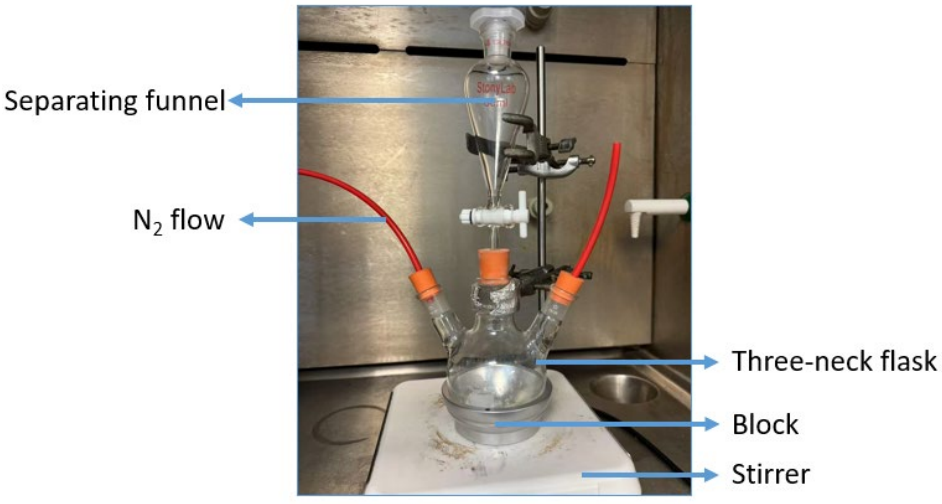


Figure 2.2 Impregnation step in the synthesis of $TiO_x/SiO_2$ catalyst

## *Transesterification Reaction*

Figure 2.3 shows the diagram of MLA to LD transesterification process. Liquid-phase transesterification of MLA to LD was conducted in a three-neck flask heated sitting in a block on a hotplate. The setup included one neck for $N_2$ purging prior to reaction (to prevent moisture ingress) and one neck connected to a DCM trap (44 mL) containing o-xylene (1 mL) as the internal standard to collect volatile products. After charging MLA (2 mL) to the reactor, the flask was brought to the set temperature (170, 200, or 220 °C), the catalyst (100 mg) was introduced, and the batch was allowed to proceed under the inert atmosphere. Reaction mixtures were analysed after completion of the batch, volatile and condensable products captured in the DCM/internal-standard trap were combined with the liquid contents for analysis. Qualitative analysis was performed by GC–MS, and quantitative analysis by GC-FID. MLA conversion was calculated by an internal-standard method using calibration curves prepared from standard MLA solutions at a fixed o-xylene concentration. Owing to uncertain oligomer distributions, selectivity was obtained by peak-area normalization.

Instrumental conditions and processing parameters (calcination temperatures, ramp rates, gas atmospheres; detector type, columns, and referencing conventions) were kept consistent across samples and experiments to permit direct comparison between $TiO_x/SiO_2$ and $TiO_2$.

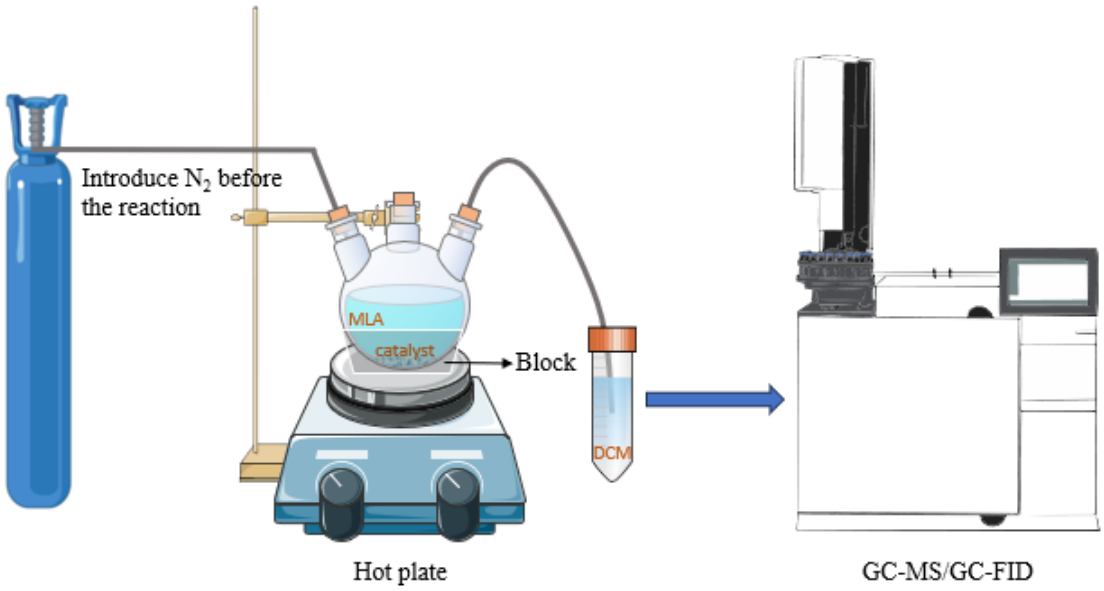


Figure 2.3 Transesterification reaction of MLA to LD process diagram

## *Material Characterization*

XRD was collected on a MiniFlex-600 diffractometer (40 kV, 15 mA) over 2θ = 3–60° with 0.02° step size to distinguish crystalline $TiO_2$ from highly dispersed $TiO_x$ species on $SiO_2$. Morphologies were examined by SEM (HITACHI S4800). Higher-resolution imaging and elemental mapping were performed by TEM and STEM-EDS (FEI Tecnai G2 F30), representative spectra were used to verify elemental composition and dispersion. XPS (Thermo Escalab 250Xi) was used to determine Ti oxidation states; spectra were referenced to C 1s = 284.8 eV. Textural properties were measured from $N_2$ adsorption–desorption isotherms at 77 K (ASAP 2460). Specific surface areas were obtained by the BET method (desorption branch), and pore-size distributions/volumes by the BJH method (adsorption branch). FT-IR spectra (MB3000 FT-IR Laboratory Analyzer) were recorded from 700 to 1100 $cm^{-1}$ at 7.7 $cm^{-1}$ resolution to probe Si–O–Si and Ti–O–Si vibrations.

### 2.1.3 Overall DFT computational methods

Figure 2.4 presents the overall process flow of the DFT modelling conducted in this thesis. The computational procedure is divided into two stages. Firstly, based on the experiment results, the Titania-silica catalyst was selected for transition state (TS) searching, thereby elucidating the reaction pathway. Secondly, adsorption analyses of MLA were performed on catalysts with different valence of Ti, both in the presence and absence of a $SiO_2$ support, to evaluate the effects of the valence of Ti and the support on adsorption behaviour.

Initially, preliminary models of the catalysts were constructed, and geometry optimizations were performed using DFT. For the reaction pathway investigation, the catalyst exhibiting the most favourable adsorption structure was selected, reasonable intermediates along the pathway were first optimized, after which TS searching were conducted. Energy barriers were subsequently determined from the TS energies. The details are provided in section "Reaction Pathway". The MLA adsorption models were then built on the DFT-optimized catalyst structures, followed by geometry optimization and energy calculation. The analyses employed adsorption energy, Bader charge, density of state (DOS), charge density difference (CDD), bond order, and bond length. Detailed modelling method are provided in the section "Adsorption of MLA".

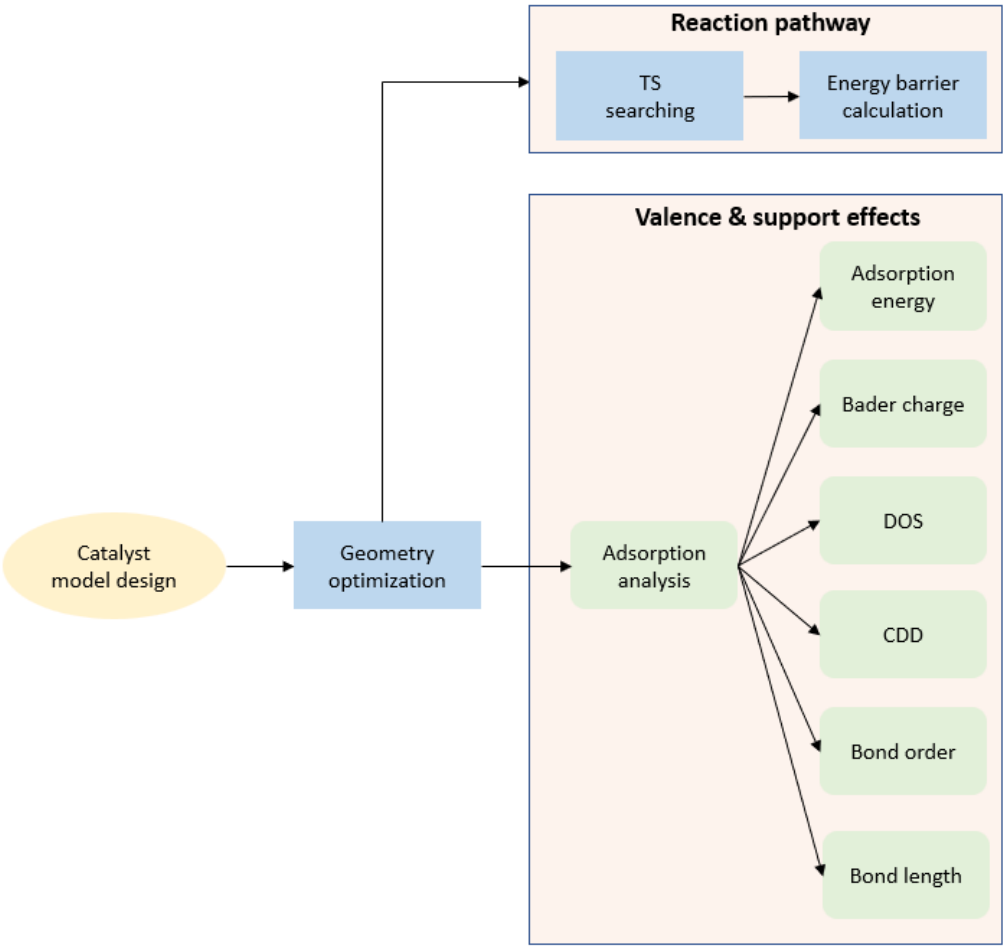


Figure 2.4 DFT calculation process flow diagram

## *Reaction Pathway*

Guided by the experiment results, the most promising Titanium-silica catalyst was selected, and an enlarged surface model consistent with the MLA → LD transesterification pathway was constructed. Adsorbed and reactants and products were fully optimized. A minimal set of elementary steps was defined. First, the 1$^{st}$ MLA was adsorbed on the surface. Second, the 2$^{nd}$ MLA were adsorbed on the surface. For the 2$^{nd}$ MLA adsorption, both adsorbed on the 1$^{st}$ MLA and adsorbed on the catalyst surface cases were tested, then combined the geometry position and adsorption energy results,

chose the surface adsorption configuration. Third, nucleophilic attack on the 2nd MLA occurred, methanol was released, and a dimeric intermediate was formed. Fourth, intramolecular transesterification closed the ring to give LD, the second methanol released. Fifth, product LD desorption was included. For each step, the initial and final states (IS and FS) were prepared from adsorption-derived binding configurations. Slab terminations and deeper layers were treated consistently across IS/TS/FS to ensure a coherent reference.

To identify TS, multiple chemically reasonable TS guesses were generated per step to minimize bias from starting geometries. Two complementary strategies were employed: the double-ended surface walking (DESW) algorithm with the climbing-image nudged elastic band (CI-NEB) method. DESW was used to explore candidate saddle points between optimized endpoints, while CI-NEB was employed to trace the minimum-energy path and drive the highest-energy image to a first-order saddle point. Each TS was subsequently verified by harmonic frequency analysis (one imaginary mode) and, where feasible, by intrinsic reaction-coordinate integrations. Energy barriers were obtained from the TS search results.

The TS searching was carried out by the Vienna Ab Initio simulation package[3,4] and LASP code[7]. The more detailed methods were written in chapter 4.

## *Adsorption of MLA*

In the adsorption of MLA part, six catalyst models were constructed: two geometries of Ti(IV) supported on $SiO_2$, two geometries of Ti(III) supported on $SiO_2$, pure anatase $TiO_2$ (Ti(IV)), and anatase $TiO_2$ with an oxygen vacancy (Ti(III)). The selection of Ti as the supported metal was guided by a review of the experimental

literature[1,2], which indicates that Ti on $SiO_2$ performs best. However, the existing studies do not pinpoint a definitive active-site geometry for simulation, therefore, even for the $TiO_x/SiO_2$ systems we explored multiple structures. After geometry optimization, all structures were subjected to higher-accuracy single-point energy calculations to obtain more reliable results.

When building the adsorption models on 6 catalysts surface, guided by the molecular structure of MLA, three distinct oxygen atoms were examined as candidate adsorption sites and explicitly multiple adsorption orientations were modelled. After geometry optimization, single point energy calculations were performed and the adsorption energies were analysed. Although geometry optimization can relax systems toward the most stable configurations, a broad set of chemically reasonable initial geometries were tried built to reduce sensitivity to initial structures (IS) and to mitigate potential errors arising from limitations of the software and optimization algorithms.

For each of the six catalysts, the structure with the strongest adsorption (i.e., the most stable adsorption energy) was selected for detailed analysis, focusing on CDD, DOS, Bader charge. Mayer Bond order and bond length were included as the support evidence. Specifically, CDD in conjunction with Bader charge analysis was used to assess the direction and extent of electron redistribution; DOS combined with Bader charge analysis was employed to evaluate orbital occupations; and bond order together with bond length was used to corroborate structural distortions before and after adsorption.

All the geometry optimization and energy calculation were carried out using the Vienna Ab Initio simulation package[3,4]. The converged wavefunctions calculation

for the Mayer bond order was computed by Gaussian 16 Packaged[5], the further Mayer bond order analysis were performed using the Multiwfn[6]. The more detailed methods were written in chapter 4.

## 2.1.4 Overall TEA computational methods

Process simulation and data generation were performed in Aspen Plus. All process flowsheets for the hydrolysis (Process 1), alcoholysis (Process 2), and alcoholysis with MLA recycle (Process 3) routes were built and solved under a consistent thermodynamic basis using the Non-Random Two-Liquid (NRTL) model. Missing physical property parameters for PLA/WPLA (waste PLA) and intermediates were estimated via UNIFAC group-contribution methods[8]. Reaction stoichiometries, conversions, and selectivity required by reactor blocks were taken from literature reported[2,9]. To enable fair cross-scenario comparison, a common design basis of 20,000 $kg \cdot h^{-1}$ WPLA feed and an on-stream factor of 0.95 (24 $h \cdot day^{-1}$, 365 $days \cdot year^{-1}$) was applied to all cases. Mass and energy balances, utility duties, and equipment sizing were obtained directly from the converged Aspen models and exported as the input deck for economic calculations.

Total capital cost was evaluated as fixed capital investment (FCI) plus working capital. FCI was estimated by the delivered equipment cost percentage method for solid–fluid processing plants[10]. Equipment purchase and installation were taken directly from Aspen Plus "Measured" reports, while other direct costs (piping, instrumentation, electrical, buildings, yard improvements, service facilities, land) and indirect costs were calculated as standard fractions of the equipment purchase cost[11]. Annualized capital charge was obtained by applying the capital-recovery factor $A_{i,N}$

with i=8% and *N*= 20 years to the total capital cost. Working capital was set to 15% of FCI.

Operating cost was computed as the sum of raw materials, utilities, labour, and fixed expenses. Raw material usage (including catalysts) and utilities (electricity, steam, cooling) were read from Aspen Plus mass/energy balances. Labour cost was based on an industrial PLA producer's public filing and converted to an hourly wage; labour was scaled with production. The unit production cost of PLA was defined as total annual cost (capital charge + operating cost + fixed expenses) divided by the simulated annual PLA production rate reported by Aspen Plus.

The more details information of TEA setting methods was written in chapter 6.

# 2.2 DFT Theory

## 2.2.1 Early Development of Computational Chemistry

### *The Schrödinger Equation*

Quantum mechanics is a fundamental theory in physics, relies heavily on the Schrödinger equation to describe the behaviour of particles at the atomic and subatomic levels. This important mathematical formulation, introduced by Austrian physicist Erwin Schrödinger in the mid-1920s, provides a means to characterize the quantum state of a system through its wave function. The equation's publication in 1926 named Schrödinger Equation, revolutionizing our understanding of matter and energy:

$$H\Psi = E\Psi \tag{2.1}$$

where $H$ is the Hamiltonian operator; Ψ is the wavefunction and E is the eigenvalue associated with Ψ, the total energy of that stationary state. The Hamiltonian is the sum of kinetic and potential terms:

$$H = -\frac{\hbar}{2m}\nabla^2 + V \tag{2.2}$$

where $V_{(r)}$ is external potential term; $-\frac{\hbar}{2m}\nabla^2$ is the kinetic term: $\hbar$ is $\frac{h}{2\pi}$, which has units of action; the reduced Planck constant $(h)$, $m$ is mass, and ∇ is Laplace operator:

$$\nabla^2 = \frac{\partial^2}{\partial x^2} + \frac{\partial^2}{\partial y^2} + \frac{\partial^2}{\partial z^2} \tag{2.3}$$

where x, y and z are positions of three-dimension Cartesian coordination.

Because the Hamiltonian operator is exceedingly complex, the Schrödinger equation can be solved analytically only for the simple systems, most famously the hydrogen atom and the $H_2^+$ molecular ion. For complicated many-body problem are resorted to numerical or approximate techniques that build on the Schrödinger framework.

## *The Many-Body System and Born-Oppenheimer (BO) Approximation*

The many-body problem in quantum chemistry refers to the challenge of accurately describing systems containing multiple interacting particles at the atomic scale. In these systems, quantum mechanical effects dominate, and the interactions between particles become complex and interdependent. These interactions include those between electrons, between electrons and nuclei, and various other cross-interactions. Due to the complexity of these interactions, obtaining an exact solution to the many-body problem is practically impossible for all but the simplest systems.

To address this challenge, scientists employ various approximations and simplifications. One of the most fundamental of these is the Born-Oppenheimer (BO) approximation. The BO approximation simplifies the quantum mechanical treatment of molecules by separating the motion of atomic nuclei from that of electrons. This approximation is based on the fact that electrons, being much lighter than nuclei, move much more rapidly. As a result, from the perspective of the electrons, the nuclei can be considered essentially stationary. The Hamiltonian operator separated to electrons and nuclei, which shows as:

$$H = T_n + T_e + V_{nn} + V_{ne} + V_{ee} \tag{2.4}$$

where $T_n$ is the kinetics operator of nuclei; $T_e$ is the kinetics operator of electrons; $V_{nn}$ is the potential operators of nuclei-nuclei Coulombic interaction; $V_{ne}$ is the potential operators of nuclei-electrons Coulombic interaction; $V_{ee}$ is the potential operators of electrons-electrons Coulombic interaction.

With the separation, the Schrödinger equation can be solved in two steps. First, the electronic Schrödinger equation is solved for fixed nuclear positions, yielding the electronic energy and wave function. Then, the nuclear Schrödinger equation is solved, using the electronic energy as a potential energy surface for nuclear motion. Formally, the total wavefunction is factorised,

$$\Psi(r, R) = \Psi_n(R) + \Psi_n(r, R) \tag{2.5}$$

where $r$ and $R$ collect the electronic and nuclear positions, respectively. The electronic part obeys:

$$H_e(r, R)\Psi_e(r, R) = E_e\Psi_e(r, R) \tag{2.6}$$

where $E_e$ is electronic energy, while the nuclear part is governed by:

$$H_n(R)\Psi_n(R) = E_n\Psi_n(R) \tag{2.7}$$

where $E_n$ represent nuclei energy. The total energy ($E_{total}$) is then the sum of the electronic energy （$E_e(R)$） and the nucleus–nucleus energy （$E_{nn}(R)$）:

$$E_{total} = E_e(R) + E_{nn}(R) \tag{2.8}$$

## *The Hartree-Fock (HF) Approximation with the Self-Consistent Field Theory*

Although the BO approximation can be used to simplify the Schrödinger equation, it is still impossible to solve for complex systems in reality. In 1927, Hartree introduced a new Self Consistent Field (SCF) method to simplify the wavefunction and energy calculation of atoms and ions, the fundamental physical parameters (ab initio) was applied, called Hartree method. SCF can estimate the spatial distribution of interacting electrons and nuclei. The wavefunction of an n-electron system was simplified as a system of n single electron wavefunction:

$$\Psi_{(r)} = \Psi_{(1)}(r_1) \cdot \Psi_{(2)}(r_2) \cdots\cdots \Psi_{(n)}(r_n) \tag{2.9}$$

However, in SCF method, the n-electron wave function is represented as the sum of the products of single electron wave functions, in which all electrons are regarded as fermions and cannot satisfy the Pauli exclusion principle, i.e., two electrons cannot occupy the same quantum state. Furthermore, since exchange the terms in the formula remain unchanged, the anti-symmetry of electrons is also not satisfied.

Later, in 1930, Slater and Fock subsequently refined the approach by replacing the Hartree method with an " anti-symmetry wavefunctions" instead of the single

electron wavefunctions, producing what is now called the Hartree-Fock (HF) method. The anti-symmetrized wavefunctions was described by Slater determinant:

$$\Psi = \frac{1}{\sqrt{N!}} \begin{vmatrix} \Psi_{1,\alpha}(1) & \Psi_{1,\beta}(1) & \cdots & \Psi_{\mathrm{N},\alpha}(1) \\ \Psi_{1,\alpha}(2) & \Psi_{1,\beta}(2) & \cdots & \Psi_{\mathrm{N},\beta}(2) \\ \vdots & \vdots & \vdots & \vdots \\ \Psi_{1,\alpha}(N) & \Psi_{1,\beta}(N) & \cdots & \Psi_{\mathrm{N},\alpha}(N) \end{vmatrix} \tag{2.10}$$

where the rows are electron coordination; the columns are electron wavefunction. The Slater determinant solved the problem of unsatisfied Pauli exclusion principle. The Schrödinger equation is calculated separately based on the slater determinant and combined to obtain an approximate multielectron wavefunction.

Even though HF method had already made a great progress in many-body system, a major problem is that it completely ignores electron correlation, which leads to large errors. Introducing electron correlation into the Fock operator can improve accuracy, but the enormous computational cost makes it challenging to simulate large systems.

## 2.2.2 Density Functional Theory

DFT recasts the many-body Schrödinger problem in terms of the electron density. Because electron density depends on only three spatial variables, whereas the full many body wavefunction depends on 3N electronic coordinates, the dimensionality of the problem is dramatically reduced.

### *The Hohenberg–Kohn (HK) theorems*

In the 1960s, the DFT method was proposed, which is used to calculate the total energy of a system while considering both electron exchange and correlation which reported by Pierre Hohenberg and Walter Kohn. DFT rests on two theorems:

Theorem I: The external potential $V_{ext}(\rho)$ and the total energy of system $E_{total}$ are unique functionals of the electron density $\rho(r)$.

Theorem II: Only when the input density is the real ground state density, the ground state energy function value of the system is lowest, which provides a variational principle formulated in terms of that density. It states that there exists a universal energy functional:

$$E[\rho(r)] = F[\rho(r)] + \int V_{\text{ext}}[\rho(r)]dr \tag{2.11}$$

where $E[\rho(r)]$ is the ground state energy of the system; $F[\rho(r)]$ is a universal functional of the density, defined as:

$$F[\rho(r)] = T[\rho(r)] + V_{\text{int}}(r)[\rho(r)] \tag{2.12}$$

where $T[\rho(r)]$ is the kinetic-energy functional and $V_{int}[\rho(r)]$ captures the electron–electron Coulomb interaction.

Therefore, the total system energy can be written as:

$$E[\rho(r)] = T[\rho(r)] + V_{\text{int}}[\rho(r)] + \int V_{\text{ext}}(r)[\rho(r)]dr \tag{2.13}$$

## *The Kohn–Sham (KS) scheme*

The Kohn-Sham (KS) scheme was improved upon the Hohenberg-Kohn theorems, making it practical and enabling DFT calculations to be performed even on a personal computer. KS scheme greatly reduced the time required for electronic

structure calculations, and this tremendous advance earned Kohn the Nobel Prize in Chemistry in 1998. KS scheme selects an auxiliary independent particle system to simplify the original many-body system and assumes that the ground state density of the two systems is the same. The systems with real potential interactions are replaced by a fictitious non-interacting system through mapping, and electrons can move within the effective Kohn-Sham single-particle potential $V_{KS}(r)$.

For N-electron system, the wavefunction can be assumed by the single-electron system, the Schrödinger Equation is written as:

$$\left(-\frac{\hbar}{2m}\nabla^2 + V_{KS}(r)\right)\varphi_i(r) = \varepsilon_i\varphi_i(r) \tag{2.14}$$

where N orbitals $\varphi_i(r)$ with one single-electron in each with the smallest eigenvalues $\varepsilon_i$. The density of auxiliary system is

$$\rho(r) = \sum_{i=1}^{N}|\varphi_i(r)|^2 \tag{2.15}$$

Thus, the total energy is

$$E[\rho(r)] = T_S[\rho(r)] + \int V_{\text{ext}}[\rho(r)]dr + V_H[\rho(r)] + E_{\text{xc}}[\rho(r)] \tag{2.16}$$

where $T_S[\rho(r)]$ is the Kohn-Sham kinetic energy, $V_{ext}[\rho(r)]$ is the external potential for nuclei-electron interaction; $V_H[\rho(r)]$ is the Hartree potential; $E_{xc}[\rho(r)]$ is the exchange-correlation functional, which represents the sum of error in the system. In the Kohn-Sham scheme, $T_S[\rho(r)]$, $V_{ext}[\rho(r)]$, and $V_{ext}[\rho(r)]$ are available to form, however, $E_{xc}[\rho(r)]$ is an unknown energy term, which is need to be approximated. A further approximation for DFT calculation is needed to solve the exchange-correlation term.

## *Exchange–correlation approximations*

Local density approximation (LDA) is a simple but successful approximation in exchange-correlation function. LDA assumes that the electron density is a homogeneous electron gas, which means the electron density at point r is the same in space. The exchange-correlation energy with LDA is:

$$E_{xc}^{LDA}[\rho(r)] = \int \rho(r)\varepsilon_{xc}[\rho(r)]dr \tag{2.17}$$

where $\rho(r)$ is the election density; $\varepsilon_{xc}$ is the exchange-correlation energy of each particle of homogeneous electron gas. In the LDA approximation, the exchange-correlation energy has two terms as:

$$E_{xc} = E_x + E_c \tag{2.18}$$

where is the exchange term and $E_c$ is the correlation term. $E_x$ called Dirac exchange, the formula is:

$$E_x[\rho(r)] = -\frac{3}{4}\left(\frac{3}{\pi}\right)^{\frac{1}{3}} \int \rho(r)^{\frac{4}{3}}\mathrm{dr} \tag{2.19}$$

However, $E_c$ (correlation term) is still no formula yet, it is constructed from quantum Monte Carlo (QMC) simulations.

Using LDA can get a well description of molecules, geometries, and vibration frequencies, however, the exchange energy is underestimated, and the correlation energy is overestimated because homogeneous electron gas assumed as the electron density. Generalized gradient approximations (GGA) reduced this problem by introducing not only density, but the gradient of the density to explain the exchange energy $E_x$. Moreover, some expanded GGA functions were proposed to further correct

the error, such as PW91[12] and Perdew-Burke-Ernzerhof (PBE)[13]. PW91 is the first GGA that can be reliably used over a very wide range of materials, however, PBE ignored some correct features of PW91 to save the cost of CPU calculation time which also applied widely in this thesis.

The GGA method also has its disadvantage: it fails to address a fundamental error in Kohn-Sham scheme. The HF method eliminates self-interactions by cancelling out the energies of exchange and Coulomb interactions when calculating the same electron, whereas the GGA approximation of exchange and correlation allows the electron density to repel itself. This means that the more localized the electron density, the stronger the false repulsion becomes, leading to erroneous delocalization phenomena in GGA functions, such as in the d orbitals of transition metals. For DFT calculation results, this has a certain impact on the electronic structure, with band gap calculations yielding larger values. In some cases, charge carriers may be migrated to the metallic state. To reduce this self-interaction error, modified GGA functions or alternative functions have been reported for electronic structure calculations.

## *DFT+U*

To reduce self-interaction error, Dudarev et al. [14]proposed a useful method of adding on-site energy penalties for partially occupied electrons with spurious delocalization in their orbitals, i.e., adding penalties to the Coulomb (U) and orbital-related exchange (J) interactions at the target site, which follows

$$E_{DFT+U} = E_{DFT} + \frac{U-J}{2}\sum_{\sigma,m}(n_{l,m,s} - n_{l,m,s}^2) \tag{2.20}$$

where n is the orbital occupation of an electron; l is the angular momentum of the orbital occupation electron; m is the magnetic quantum number; s is the spin. The (U -

J) factor in the DFT+U formula (2.20) can only insert one energy penalty. That is, if J is assumed to be zero, the penalty is purely a Coulomb interaction. The selection of U values is typically determined by comparing the results of DFT+U calculations with empirical data, and the specific correction accuracy depends on the system. DFT+U correction is a relatively simple correction method that does not add significant computational costs to commonly used LDA or GGA functional.

## 2.2.3 Application of DFT on Solid Surface

### *Basis set*

In first-principles electronic-structure theory, a basis set is a collection of functions used to expand the one-electron Kohn–Sham orbitals and thereby represent the many-electron ground state within Hartree–Fock or DFT[15,16]. Common choices are linear combinations of atomic orbitals (LCAO), which employ localized atomic functions, and plane waves, which are compatible with periodic boundary conditions in crystalline materials[17,18]. This work was employed a plane waves basis set because it offers systematic and monotonic convergence controlled by a single kinetic-energy cut-off ($Ecut$). Moreover, because several key operators become simple in reciprocal space, for example, the kinetic-energy operator is diagonal, while real-space quantities can be evaluated efficiently via fast Fourier transforms (FFT)[17,19].

For a given crystal momentum k, the Kohn–Sham orbital is expanded as a sum over reciprocal lattice vectors G with $\frac{|\mathrm{k+G}|^2}{2} < Ecut$ :

$$\Psi_{\mathrm{nk}}(\mathrm{r}) = \sum_{\mathrm{G}}^{\frac{|\mathrm{k+G}|^2}{2} < Ecut} c_{\mathrm{nk}}(\mathrm{G}) \mathrm{e}^{\mathrm{i(k+G)\cdot r}} \qquad (2.21)$$

where $\Psi_{nk}(r)$ is Fourier Series expansion expression; $c_{nk}(G)$ are Fourier coefficients stored on a regular G-space grid[17,19]. In practice, $Ecut$ is chosen by convergence tests on total energy, forces, stress, and the target observables (e.g., defect formation energies or migration barriers), increasing $Ecut$ above the dataset's recommended value until changes fall below a predefined tolerance[17].

## *Supercell*

Real materials often contain surfaces, interfaces, dilute dopants, and point defects, modelling such features at tractable cost is commonly achieved by combining supercells with periodic boundary conditions[17]. The formal underpinning is Bloch's theorem, which states that each one-electron state can be written as a plane wave times a lattice-periodic function:

$$\Psi_{nk}(r) = e^{ik-r} \tag{2.22}$$

$$u(r) = u(r + l) \tag{2.23}$$

where l is a direct-lattice translation and k lies in the first Brillouin zone[20]. Expanding the periodic part in a Fourier series over reciprocal vectors G,

$$u_{nk}(r) = \sum_{G} c_{nk}(G) e^{iG\cdot r} \tag{2.24}$$

yields the conventional plane-wave representation

$$\Psi_{nk}(r) = \sum_{G} c_{nk}(G) e^{i(k+G)\cdot r} \tag{2.25}$$

To control finite-size and image interactions, the supercell must be large enough that defect–defect or adsorbate–adsorbate separations exceed typical screening lengths,

while slab models require sufficient vacuum (often ≥10–20 Å) and, for asymmetric slabs, a dipole correction[17,19]. Brillouin-zone integration employs Monkhorst–Pack meshes or Γ-centered grids, the required k-point density decreases as the supercell grows[17,21].

## *The Pseudopotential Approximation*

By Bloch's theorem, the Kohn–Sham orbitals of a periodic solid can be expanded in plane waves. Figure 2.5 shows the comparison of all-electron (AE) wavefunction and pseudopotential (PS) wave function[32]. In the vicinity of atomic cores, the strong Coulomb potential drives rapid oscillations of the valence wavefunctions. Accurately resolving these features with a pure plane-wave basis requires very high cut-off energy and thus an extremely large number of basis functions (often exceeding $10^4$), which is computationally demanding. This is why pseudopotentials are used: they replace the complicated core region by a smooth, equivalent potential so the wavefunction is easy to represent (fewer plane waves), while outside the core they are forced to match the all-electron solution, so valence properties remain unchanged.

The plane-wave cutoff energy  is determined by the hardest pseudopotential present; use a single global value at or above the largest species recommendation and validate by convergence.

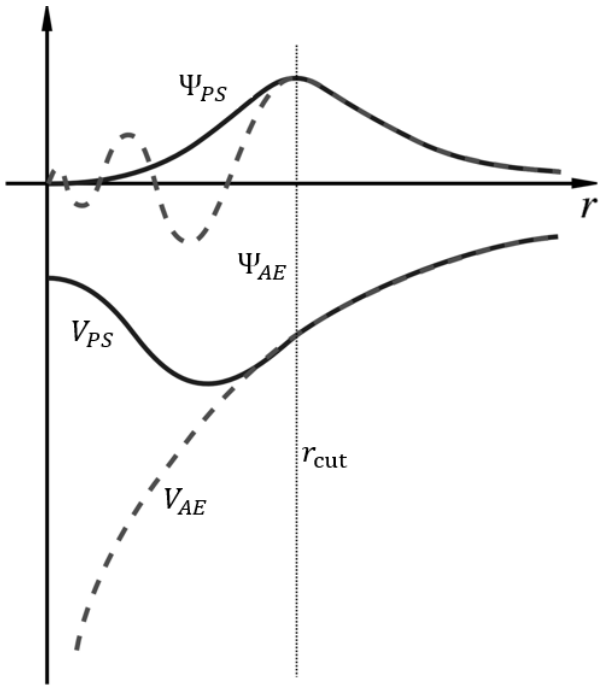


Figure 2.5 Comparison of AE wavefunction and PS wave function[32].

An AE wavefunction shows in dash line, PS wave shows in solid line. The $r_{cut}$ represents the dividing line, where the all-electron potential and the pseudo-electron potential to the right of $r_{cut}$ match well.

## *The Projector Augmented Wave (PAW) Method*

The projector augmented-wave (PAW) method is a first-principles framework that unifies the accuracy of AE approaches with the efficiency of plane-wave pseudopotentials, and can be viewed as a systematic generalization of both pseudopotential and linear augmented plane wave (LAPW) ideas, enabling DFT calculations at reduced computational cost without sacrificing AE fidelity[22,23].

In crystalline materials, valence wavefunctions oscillate strongly near ionic cores because they must remain orthogonal to core states; representing these rapid variations with plane waves alone demands very high kinetic-energy cutoffs or, in real-

space methods, extremely fine grids. PAW resolves this by introducing a linear transformation $\mathcal{T}$ that maps a smooth, computationally convenient pseudo-like wavefunction $|\Psi\rangle$ onto the corresponding AE wavefunction $|\Psi\rangle$[23],

$$|\Psi\rangle = |\Psi\rangle + \sum_i (|\phi_i\rangle - |\tilde{\phi}_i\rangle)\langle \tilde{p}_i|\Psi\rangle \tag{2.26}$$

where $|\phi_i\rangle$ and $|\tilde{\phi}_i\rangle$ are sets of AE and pseudo partial waves inside atom-centred augmentation spheres, and $\tilde{p}_i$ are a set of projector functions. This construction confines the rapid core-region oscillations to compact augmentation regions while keeping the interstitial description smooth, thereby allowing moderate plane-wave cutoffs and, at the same time, an exact reconstruction of AE-quality charge densities, forces, and matrix elements from the smooth solution.

## *Geometry Optimisation*

In computational chemistry, geometry structure optimisation is also known as energy minimisation or energy optimisation. It refers to a stationary point on the potential energy surface (PES) sought by a computational model of chemical bonds, at which the net interatomic forces of each atom are zero. The basic method for finding geometry optimisation is to sample randomly generated structures. The process of randomly filling space with atoms is likely to produce many physically unreasonable structures (such as thermodynamics, chemical kinetics, spectroscopy, etc.), so constraints are needed to remove known high energy regions from the PES.

In modern theoretical calculations, two methods are commonly used for constrained optimisation: Quasi-Newton algorithm[24] and Conjugate-gradient algorithms (CG)[25]. The Quasi-Newton algorithm algorith converges faster when the

input structure is close to the local minimum of the potential energy surface because it provides curvature information. However, if the initial guess structure is poor and far from the local minimum of the potential energy surface, the Quasi-Newton algorithm will take a long time. In this case, the CG algorithms is more suitable. The CG algorithm combines the simplicity of the gradient steepest descent method with the ability to search for minima at different measurement degrees, accelerating the search speed. CG algorithm is commonly used in DFT optimisation.

## *Transition State (TS) Searching*

For reactions and diffusion events on periodic solid surfaces, the TS is the special configuration that lies at the highest energy along the minimum-energy reaction path but remains a local minimum with respect to all coordinates orthogonal to that path. In other words, it is a first-order saddle point on the PES of the system. The study of transition states is an important means of exploring reaction mechanisms, and transition states also provide information on reaction kinetics, allowing reaction rates to be calculated through reaction barriers[26].

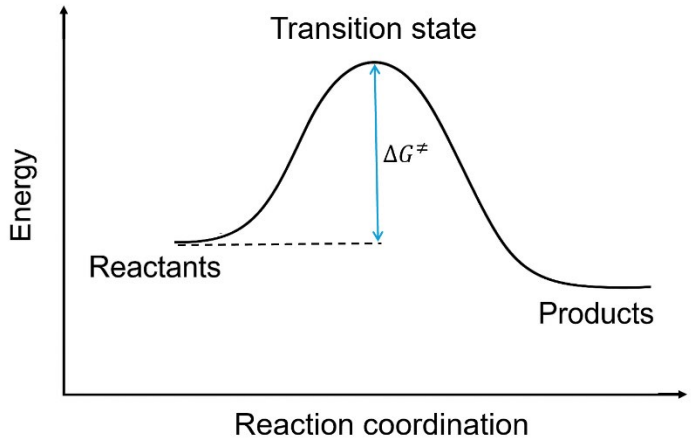


Figure 2.6 TS diagram of a chemical reaction[26]

Figure 2.6 schematically shows the potential energy (or free energy) of a reaction plotted against a reaction coordinate. The TS is the configuration at the maximum along the minimum-energy path but a minimum along all transverse directions, i.e., a first-order saddle point on the potential energy surface. The vertical arrow labelled $\Delta G^{\neq}$ denotes the activation energy, defined as the energy difference between the reactant minimum and the TS. Within transition state theory, the rate constant is

$$k = \frac{k_B \mathrm{T}}{h} e^{-\frac{-\Delta G^{\neq}}{k_B T}} \tag{2.27}$$

where $k_B$ is Boltzmann constant; $\hbar$ is Planck constant; T is the temperature.

## 2.2.4 Analysis of DFT

### *Charge Density Difference*

Charge density differences (CDD) are one of the most important methods for studying electronic structure[27,28]. By comparing the electron density of a combined system with that of its constituent fragments, or between different physical states. CDD provides an intuitive map of electron gain, loss, and redistribution, thereby illuminating the nature of chemical bonding[6,18]. Depending on the application, several equivalent CDD definitions can be employed. Eq (2.28-2.30) shows the definition of CDD.

Binding/interaction CDD, the total system subtracts the density of other segments:

$$\Delta\rho = \rho_{AB} - \rho_A - \rho_B \tag{2.28}$$

Deformation CDD, before and after self-consistent calculation:

$$\Delta\rho = \rho(AB_{self-consistent}) - \rho(AB_{atomic}) \quad (2.29)$$

State-to-state CDD, one electronic state subtracts density in another.:

$$\Delta\rho = \rho(AB_{state1}) - \rho(AB_{state0}) \quad (2.30)$$

## *Bader Charge Analysis*

Richard Bader, proposed a way to divide a molecule or solid into atoms using only the electron density[29]. This method of charge calculation utilizes zero-flux surfaces to partition atoms. A zero-flux surface is a two-dimensional surface where the charge density is minimized perpendicular to the surface. Beyond its value for visualizing "atoms in molecules," Bader's partitioning is a practical tool for quantitative charge analysis. The electron count integrated over a Bader volume gives a reliable estimate of an atom's total electronic charge. The real-space charge distribution obtained from this partition can be used to evaluate multipole moments for interacting atoms or molecules. The same framework has also been employed to define atomic hardness, offering a measure of the energetic cost of removing charge from a given atom.

## *Density of States*

The essence of the density of states (DOS) is the number of electrons occupying different states at specific energy levels, that is, the number of electron states per unit energy volume. Many bulk properties depend on it, such as heat capacity, paramagnetic susceptibility, and transport in conductors. DOS calculations show how states are distributed with energy. They also reveal the spacing between bands in semiconductors (the band gap)[30]. Usually, DOS in a material is continuous. In isolated systems, such as

gas-phase atoms or molecules, the DOS is discrete which looks like a spectrum. Spatial variations, often caused by distortions of the original system, are called the local density of states (LDOS).

## *Bond Order*

In classical chemistry, bond strength and type are labelled with integers (e.g., 1 for a single bond, 2 for a double bond). In DFT, by contrast, bond orders become continuous quantities, capturing partial bonding and relative strength. One can extract electron density information in the region between two atoms (regardless of whether a chemical bond is formed) and use it to estimate bond strength. Although these numbers typically track the familiar single/double bond trend, they are most valuable for qualitatively comparing changes in bonding along a pathway, thereby clarifying how bonds weaken, form, or rearrange during a reaction mechanism.

A commonly used calculation approach method employs an overlap matrix, which describes the degree of overlap between two atomic orbitals. Mayer bond order (Eq(2.31)), which is a wavefunction-based measure of bond order that handles complex systems, such as transition metal complexes and supramolecular assemblies[31].

$$I_{AB} = I_{AB}^{\alpha} + I_{AB}^{\beta} = 2\sum_{a\in A}\sum_{b\in B}\left[(P^{\alpha}S)_{ba}(P^{\alpha}S)_{ab} + (P^{\beta}S)_{ba}(P^{\beta}S)_{ab}\right] \quad (2.31)$$

where $P^{\alpha}$ and $P^{\beta}$ are alpha and beta density matrix; S is overlap matrix.

# References

(1) De Clercq, R.; Dusselier, M.; Makshina, E.; Sels, B. F. Catalytic Gas-Phase Production of Lactide from Renewable Alkyl Lactates. Angew. Chem. Int. Ed. 2018, 57 (12), 3074–3078. https://doi.org/10.1002/anie.201711446.

(2) De Clercq, R.; Dusselier, M.; Poleunis, C.; Debecker, D. P.; Giebeler, L.; Oswald, S.; Makshina, E.; Sels, B. F. Titania-Silica Catalysts for Lactide Production from Renewable Alkyl Lactates: Structure–Activity Relations. ACS Catal. 2018, 8 (9), 8130–8139. https://doi.org/10.1021/acscatal.8b02216.

(3) Kresse, G.; Furthmüller, J. Efficient Iterative Schemes for Ab Initio Total-Energy Calculations Using a Plane-Wave Basis Set. Phys. Rev. B 1996, 54 (16), 11169–11186. https://doi.org/10.1103/PhysRevB.54.11169.

(4) Kresse, G.; Furthmüller, J. Efficiency of Ab-Initio Total Energy Calculations for Metals and Semiconductors Using a Plane-Wave Basis Set. Comput. Mater. Sci. 1996, 6 (1), 15–50. https://doi.org/10.1016/0927-0256(96)00008-0.

(5) Frisch, M. J.; Trucks, G. W.; Schlegel, H. B.; Scuseria, G. E.; Robb, M. A.; Cheeseman, J. R.; Scalmani, G.; Barone, V.; Petersson, G. A.; Nakatsuji, H.; Li, X.; Caricato, M.; Marenich, A. V.; Bloino, J.; Janesko, B. G.; Gomperts, R.; Mennucci, B.; Hratchian, H. P.; Ortiz, J. V.; Izmaylov, A. F.; Sonnenberg, J. L.; Williams-Young, D.; Ding, F.; Lipparini, F.; Egidi, F.; Goings, J.; Peng, B.; Petrone, A.; Henderson, T.; Ranasinghe, D.; Zakrzewski, V. G.; Gao, J.; Rega, N.; Zheng, G.; Liang, W.; Hada, M.; Ehara, M.; Toyota, K.; Fukuda, R.; Hasegawa, J.; Ishida, M.; Nakajima, T.; Honda, Y.; Kitao, O.; Nakai, H.; Vreven, T.; Throssell, K.; Montgomery, J. A., Jr.; Peralta, J. E.; Ogliaro, F.; Bearpark, M. J.; Heyd, J. J.; Brothers, E. N.; Kudin, K. N.; Staroverov, V. N.; Keith, T. A.; Kobayashi, R.; Normand, J.; Raghavachari, K.; Rendell, A. P.; Burant, J. C.; Iyengar, S. S.; Tomasi, J.; Cossi, M.; Millam, J. M.; Klene, M.; Adamo, C.; Cammi, R.; Ochterski, J. W.; Martin, R. L.; Morokuma, K.; Farkas, O.; Foresman, J. B.; Fox, D. J. Gaussian˜16 Revision C.01, 2016.

(6) Lu, T. A Comprehensive Electron Wavefunction Analysis Toolbox for Chemists, Multiwfn. J. Chem. Phys. 2024, 161 (8). https://doi.org/10.1063/5.0216272.

(7) Huang, S.; Shang, C.; Kang, P.; Zhang, X.; Liu, Z. LASP: Fast Global Potential Energy Surface Exploration. WIREs Comput. Mol. Sci. 2019, 9 (6). https://doi.org/10.1002/wcms.1415.

(8) Yu, J.; Xu, S.; Liu, B.; Wang, H.; Qiao, F.; Ren, X.; Wei, Q. PLA Bioplastic Production: From Monomer to the Polymer. Eur. Polym. J. 2023, 193, 112076. https://doi.org/10.1016/j.eurpolymj.2023.112076.

(9) Hu, Y.; Daoud, W. A.; Fei, B.; Chen, L.; Kwan, T. H.; Ki Lin, C. S. Efficient ZnO Aqueous Nanoparticle Catalysed Lactide Synthesis for Poly(Lactic Acid) Fibre Production from Food Waste. J. Clean. Prod. 2017, 165, 157–167. https://doi.org/10.1016/j.jclepro.2017.07.067.

(10) Heo, S.; Park, H. W.; Lee, J. H.; Chang, Y. K. Design and Evaluation of Sustainable Lactide Production Process with an One-Step Gas Phase Synthesis Route. ACS Sustain. Chem. Eng. 2019, 7 (6), 6178–6184. https://doi.org/10.1021/acssuschemeng.8b06383.

(11) Mairizal, A. Q.; Sembada, A. Y.; Tse, K. M.; Haque, N.; Rhamdhani, M. A. Techno-Economic Analysis of Waste PCB Recycling in Australia. Resour. Conserv. Recycl. 2023, 190, 106784. https://doi.org/10.1016/j.resconrec.2022.106784.

(12) Perdew, J. P.; Wang, Y. Accurate and Simple Analytic Representation of the Electron-Gas Correlation Energy. Phys. Rev. B 1992, 45 (23), 13244–13249. https://doi.org/10.1103/physrevb.45.13244.

(13) Perdew, J. P.; Burke, K.; Ernzerhof, M. Generalized Gradient Approximation Made Simple. Phys. Rev. Lett. 1996, 77 (18), 3865–3868. https://doi.org/10.1103/physrevlett.77.3865.

(14) Dudarev, S. L.; Botton, G. A.; Savrasov, S. Y.; Humphreys, C. J.; Sutton, A. P. Electron-Energy-Loss Spectra and the Structural Stability of Nickel Oxide: An LSDA+U Study. Phys. Rev. B 1998, 57 (3), 1505–1509. https://doi.org/10.1103/physrevb.57.1505.

(15) Hohenberg, P.; Kohn, W. Inhomogeneous Electron Gas. Phys. Rev. 1964, 136, B864–B871. https://doi.org/10.1103/PhysRev.136.B864.

(16) Kohn, W.; Sham, L. J. Self-Consistent Equations Including Exchange and Correlation Effects. Phys. Rev. 1965, 140, A1133–A1138. https://doi.org/10.1103/PhysRev.140.A1133.

(17) Payne, M. C.; Teter, M. P.; Allan, D. C.; Arias, T. A.; Joannopoulos, J. D. Iterative Minimization Techniques for ab initio Total-Energy Calculations: Molecular Dynamics and Conjugate Gradients. Rev. Mod. Phys. 1992, 64, 1045–1097. https://doi.org/10.1103/RevModPhys.64.1045.

(18) Martin, R. M. Electronic Structure: Basic Theory and Practical Methods, 2nd ed.; Cambridge University Press: Cambridge, 2020.

(19) Cooley, J. W.; Tukey, J. W. An Algorithm for the Machine Calculation of Complex Fourier Series. Math. Comput. 1965, 19, 297–301. https://doi.org/10.1090/S0025-5718-1965-0178586-1.

(20) Bloch, F. Über Die Quantenmechanik Der Elektronen in Kristallgittern. Z. Für Phys. 1929, 52, 555–600. https://doi.org/10.1007/BF01339455.

(21) Monkhorst, H. J.; Pack, J. D. Special Points for Brillouin-Zone Integrations. Phys. Rev. B 1976, 13 (12), 5188–5192. https://doi.org/10.1103/PhysRevB.13.5188.

(22) Kresse, G.; Joubert, D. From Ultrasoft Pseudopotentials to the Projector Augmented-Wave Method. Phys. Rev. B 1999, 59 (3), 1758–1775. https://doi.org/10.1103/PhysRevB.59.1758.

(23) Blöchl, P. E. Projector Augmented-Wave Method. Phys. Rev. B 1994, 50 (24), 17953–17979. https://doi.org/10.1103/physrevb.50.17953.

(24) Pulay, P. CONVERGENCE ACCELERATION OF ITERATWE SEQUENCES. THE CASE OF SCF ITERATION.

(25) Hestenes, M. R.; Stiefel, E. Methods of Conjugate Gradients for Solving Linear Systems.

(26) Jensen, Frank. Introduction to Computational Chemistry; 1999.

(27) Milman, V.; Winkler, B.; White, J. A.; Pickard, C. J.; Payne, M. C.; Akhmatskaya, E. V.; Nobes, R. H. Electronic Structure, Properties, and Phase Stability of Inorganic Crystals: A Pseudopotential Plane-Wave Study. Int. J. Quantum Chem. 2000, 77 (5), 895–910. https://doi.org/10.1002/(SICI)1097-461X(2000)77:5%253C895::AID-QUA10%253E3.0.CO;2-C.

(28) Wang, V.; Xu, N.; Liu, J.-C.; Tang, G.; Geng, W.-T. VASPKIT: A User-Friendly Interface Facilitating High-Throughput Computing and Analysis Using VASP Code. Comput. Phys. Commun. 2021, 267, 108033. https://doi.org/10.1016/j.cpc.2021.108033.

(29) Bader, R. F. W. A Quantum Theory of Molecular Structure and Its Applications. Chem. Rev. 1991, 91 (5), 893–928. https://doi.org/10.1021/cr00005a013.

(30) Sachs, M.; Grosewald, P. Solid State Theory; 1975.

(31) Bridgeman, A. J.; Cavigliasso, G.; Ireland, L. R.; Rothery, J. The Mayer Bond Order as a Tool in Inorganic Chemistry†. J. Chem. Soc. Dalton Trans. 2001, No. 14, 2095–2108. https://doi.org/10.1039/b102094n.

(32) Råsander, M. A Theoretical Perspective on the Chemical Bonding and Structure of Transition Metal Carbides and Multilayers. phd, 2010.

# Chapter 3

# PLA Compared with Other Polymers: Properties and Recycling Potential

This chapter systematically evaluates the sustainability potential of polylactic acid (PLA) with other widely-used fossil-based and bio-based polymers. Seventeen commercially relevant polymers are benchmarked against a clear set of performance and sustainability metrics. Quantitative indicators are compiled from peer-reviewed literature and industrial technical sources, including mechanical strength, thermal properties, water and chemical resistance and their environmental impacts (including carbon footprint, recyclability and composability). This comparative evaluation is designed not to identify an abstract “best” plastic, but rather to determine which material offers the most informative balance of industrial relevance, property profile, and unresolved circularity challenges.

# 3.1 Methodology

## 3.1.1 Polymer Selection

Seventeen different polymers, including both fossil-based and bio-based materials, were selected for this comparative analysis. These materials were chosen based on their widespread use in various sectors (e.g., packaging, consumer goods, medical applications) and their representation of diverse polymer classes. For fossil-based polymers, high density polyethylene (HDPE), low density polyethylene (LDPE), polyethylene terephthalate (PET), polypropylene (PP), polyvinyl chloride (PVC), polystyrene (PS), polycarbonate (PC), polycaprolactone (PCL), polybutylene adipate terephthalate (PBAT), and polybutylene succinate (PBS) were selected. Among these, there are two types of PP considered since they have different properties. One is PP (homo), that is only produced by propylene monomer. Another one is PP (random), the co-polymer that is produced by polymerizing together ethene and propene. For bio-based polymers polylactic acid (PLA), poly(3-hydroxybutyrate-co-3-hydroxyvalerate) (PHBV), thermoplastic starch (TPS), cellulose acetate (CA), bio-based PA, bio-based PET, and bio-based PBS were selected. These polymers and their applications are shown in Table 3.1.

Table 3.1 The selected fossil- and bio-based polymers and their applications

| Polymer | Applications |
|---|---|
| Fossil-based | |
| HDPE | Bottles, corrosion-resistant piping, geomembranes, and plastic lumber[1,2] |
| LDPE | Packaging films, bags, sacks, other films, rigid packaging, and construction[3] |
| PET | Textiles, high-strength film, rigid packaging, flexible packaging, photovoltaic modules, and thermoplastic resins[4,5] |
| PP (homo) | Piping, packaging, sack, containers, fibers, transportation, electrical, and consumer goods[6] |
| PP (random) | Piping, packaging, sack, containers, fibers, transportation, electrical, and consumer goods, not preferable for food contact applications[6] |
| PVC | Food packaging, children toys, medical devices, wire and cable[7] |
| PS | Construction, packaging foam such as meat trays and egg cartons, and biaxially oriented film for food packaging[1] |
| PC | Drug delivery, orthopedic applications, lens, Electronic, 3D printing [8] |
| PCL | Drug delivery, film, fibers, and micro-particle [9,10] |
| PBAT | Packaging, biomedical sector, agriculture [11] |
| PBS | Packaging, tissue or bone repair [12,13] |
| Bio-based | |
| PLA | Rigid packaging, cold drink cups, bottles, injection molded products, extrusion coatings [14] |
| PHBV | Drugs, medical implants and repairs, specialty packaging, orthopedic devices and manufacturing bottles for costumers' goods [15] |
| TPS | Films for fresh produce and meat[16] |
| CA | Metalized cellulose film for snacks, trays [16] |
| PA (bio-based) | Automotive applications [16] |
| PET (bio-based) | Bottles (~86%), automotive interiors, construction goods, electronics [16] |
| PBS (bio-based) | Flexible packaging, coffee capsules [17] |

## 3.1.2 Performance Criteria and Data Extraction

Data for a range of key performance indicators were collected to form a holistic comparison. The criteria are grouped into four categories: 1. Mechanical Properties: Tensile strength, tensile elongation at break, Young's modulus, flexural modulus, and density were reviewed to assess material durability and suitability for various physical forms. 2. Thermal properties: Melting temperature (Tm) and glass transition temperature

(Tg) are assessed to determine the viable operating temperature range for consumer products. 3. Chemical properties: Water absorption and chemical resistance (to weak acids, weak alkalis, and UV radiation) are evaluated to gauge performance in common use environments. 4. Environmental Indicators: Key life cycle assessment (LCA) parameters, including $CO_2$ emissions, energy usage, and mechanical recyclability, are included to quantify the environmental footprint.

### 3.1.3 Multi-Criteria Decision Analysis (MCDA) Framework

To provide a structured and impartial overall evaluation, a MCDA framework is developed. MCDA is a methodology brings widely recognized for its effectiveness in complex material selection problems for sustainable design[18]. For the mechanical and thermal property, tensile strength, elongation and melting temperature are selected to compare, which is the lowest standard to avoid breakage and being melted. The evaluation order of rating from highest to lowest is excellent, good, fair, and poor. The score for the property parameters is divided into five grades, the best property is recorded as 5, and the scores are sorted to 1 in descending order. Materials that are unsuitable or have a property of concern are highlighted in yellow. If a material has a range of values for tensile strength, elongation at break, water adsorption, $CO_2$ emission, or energy usage, the middle value is used to represent the performance. To define a score, the maximum value is selected and the range is divided into five intervals, and then give them the score. For the chemical resistance, some data are still unavailable, for the final evaluation, some values are approximated. Some bio-based polymers didn't have detailed data for each property, but they had a total chemical medical resistance rank with others together, so a score based is given on it. The chemical resistance of PBAT, PBAT can be used as a substitute for polyethylene (PE) and is very similar to LDPE in its properties, so we use the value

of LDPE. For the LCA energy of bio-based PA and bio-based PBS, we choose the value of polyamide 11(PA 11), and PBS, because they have similar properties.

## 3.2 Results and Discussion

In this section the properties of the selected polymers are analyzed, and their mechanical, thermal and chemical properties are compared to determine which polymers would be suitable for modern life. Their environmental impacts are also assessed, so that the most environmentally friendly options can be selected.

### 3.2.1 Mechanical properties

The mechanical properties of a polymer are fundamental to its structural integrity and long-term durability in a wide range of consumer and industrial applications. Therefore, a comprehensive review of several key mechanical indicators is conducted to create a comparative performance baseline. This analysis includes tensile strength, tensile elongation at break, and Young's modulus to understand how materials respond to deformation and resist fracture. Flexural modulus is also evaluated to assess material stiffness and suitability for load-bearing designs. It should be noted that while this study does not target a specific product with pre-defined minimum design specifications, the comparative data presented provides a valuable framework for future material selection and the elimination of unsuitable candidates. All reviewed data is based on standardized testing methodologies, primarily ASTM D638/ISO 527 for tensile properties, ASTM D790/ISO 178 for flexural modulus, and ASTM D1505/D792-98/ISO 1183-2 for density measurements.

Figure 3.1a compares the tensile strengths across the different polymers[16,19]. It can be seen that PET and PLA have high tensile strength values which are over 60 MPa. The tensile strengths of LDPE, PBAT, and TPS are low, below 20 MPa. For most of other polymers, the value ranges from 20 to 60 MPa.

Figure 3.1b shows the results of tensile elongation at break. HDPE, PCL, and PBAT have a very high elongation of over 400%. PS, PHAs, PLA, TPS, and CA have weak elongation at break, less than 10%, with bio-based PA being slightly higher at about 59%. Other polymers range from 100% to 350%. Overall, bio-based polymers demonstrate weaker elongation at break, PLA is a representative brittle, high-strength member of this group.

Figure 3.1c presents the results of Young's modulus, bio-based polymers are good at this property. PHA has the highest value reaching 8.05 GPa, the values of other bio-based polymers (PLA, TPS, CA, and bio-based PA) are over 3 GPa. As for the fossil-based polymers, HDPE, LDPE PP (random), PS is the highest reaching 3.6 GPa, and then is PET reaching 3.1 GPa. PCL, PBAT, and PBS are weak at Young's modulus which are lower than 1 GPa. Other fossil-based polymers, PP (homo), PVC, and PC, are in the middle range (2.2-2.8 GPa). Taken together, PLA combines high modulus (>3 GPa) with low elongation, which makes it stiff but brittle without modification.

Figure 3.1d reports the results of flexural modulus, the value of PC is the highest reaching 2800 MPa, the following are PVC, PS and CA, which are around 2750, 2650, and 2405 MPa. Other polymers (like PLA) are lower than 2000 MPa, indicates moderate bending stiffness. The value of LDPE, PCL, PBAT are below 350 MPa, which shows that these materials are easier to deform.

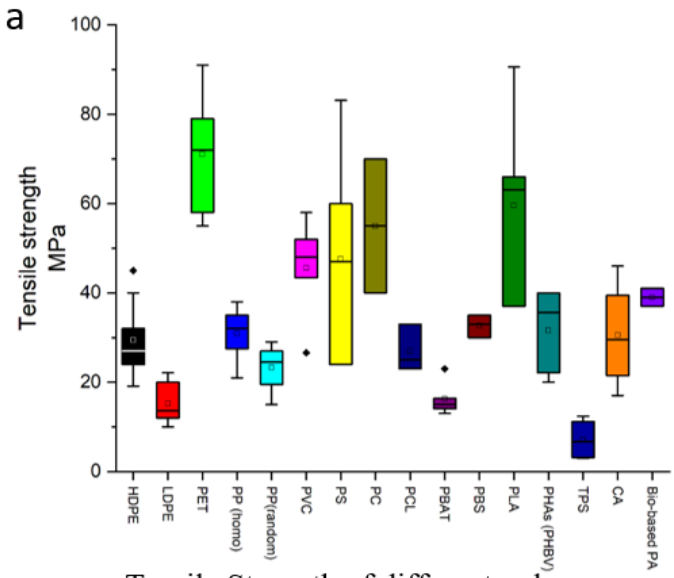


Tensile Strength of different polymers

(ref [7,16,19,20])

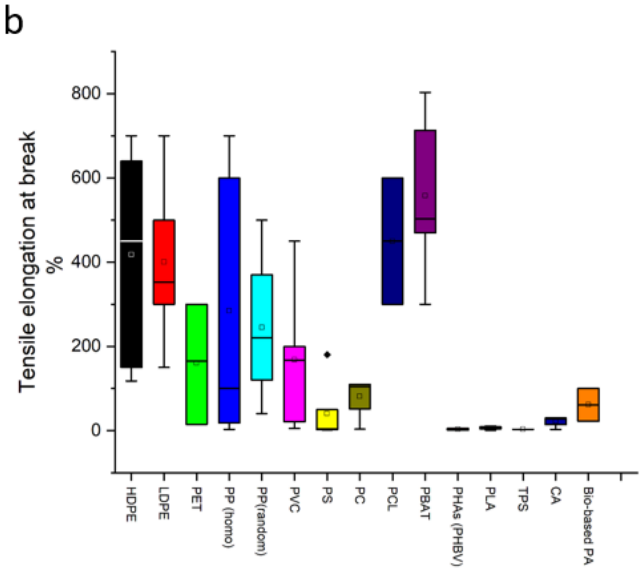


Tensile elongation at break of different polymers

(ref [7,16,19,20,22–31])

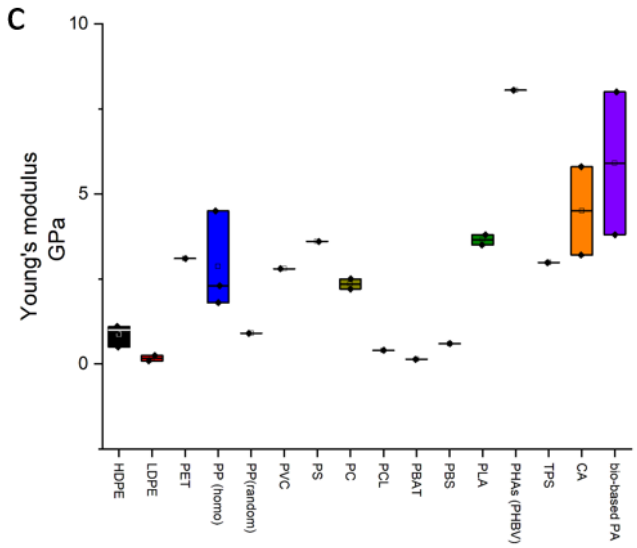


Young's modulus of different polymers

(ref [19,27,33–40])

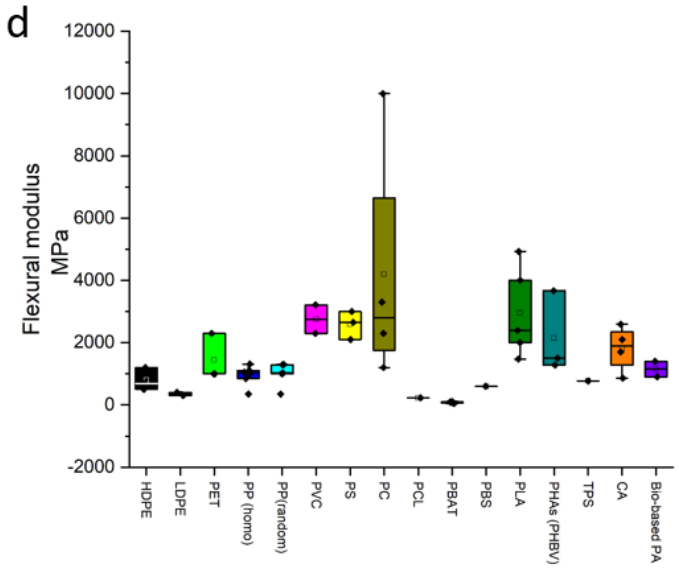


Flexural modulus of different polymers

(ref [16,20,22,25,27,28,30,39,42–44])

Figure 3.1 Mechanical properties of different polymers.

a. Tensile Strength; b. Tensile elongation at break; c. Young's modulus; d. Flexural modulus

## 3.2.2 Thermal properties

The thermal properties of a polymer are crucial for determining its suitability for consumer product applications, where materials may be exposed to a range of temperatures from sub-ambient up to 100°C. The polymers are discussed in this study fall into three structural categories: crystalline, semi-crystalline, and amorphous. Within this selection, only PBS is fully crystalline[49], while PLA, HDPE, LDPE, PET, PP, PCL, PBAT, PHBV, TPS, and bio-based PA are semi-crystalline. PVC, PS, PC, and CA are classified as amorphous polymers. Crystalline polymers have specific Tm or melting points. A melting temperature for the amorphous polymer is reported usually representing the average in the softening range. Amorphous polymers do not have a melt temperature and for these materials it is useful to consider the Tg, which is a transition from a more flexible to a more rigid state[49]. Semi-crystalline polymers are a mixture of both crystalline and amorphous structures, so both glass transition temperature and melting temperature are considered. Tg is definitely shown to decrease with increasing degree of crystallinity.

### *Melting temperature*

The melting temperature (Tm)of different polymers shows in Figure 3.2. It can be seen that the melting point of PLA lies within the medium-to-high temperature range (around 170°C), lower than that of PET/PC/CA/bio-PA, yet significantly higher than other polymers. Moreover, PLA exhibits minimal variation in its temperature distribution, indicating that the processing temperature window for different grades of PLA remains relatively controllable.

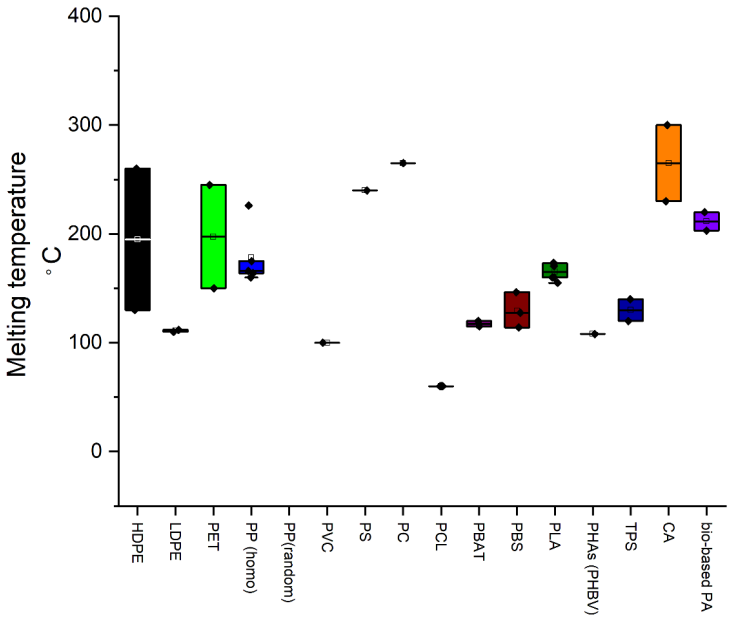


Figure 3.2 Melting temperature of different polymers (ref [19,25,34,37,39,41,42,46,47,50–54])

## *Glass transition temperature*

The glass transition temperature (Tg) of the different polymers are summarized in Figure 3.3. For the amorphous polymer, in order to ensure the normal using form, the use temperature should be lower than Tg[55]. The Tg of amorphous polymers (PVC, PS, PC and CA) are higher than 100 ℃ The stability of crystalline polymers is affected by the Tm more because they have a highly ordered molecular structure. For the semi-crystalline polymers, Tg can be affected the amorphous part, Tm affected the crystalline part, for the using temperature is between Tg and Tm. The glass transition temperature (Tg) of PLA ranges approximately between 55 and 65℃, rendering it unsuitable for applications involving excessively high temperatures.

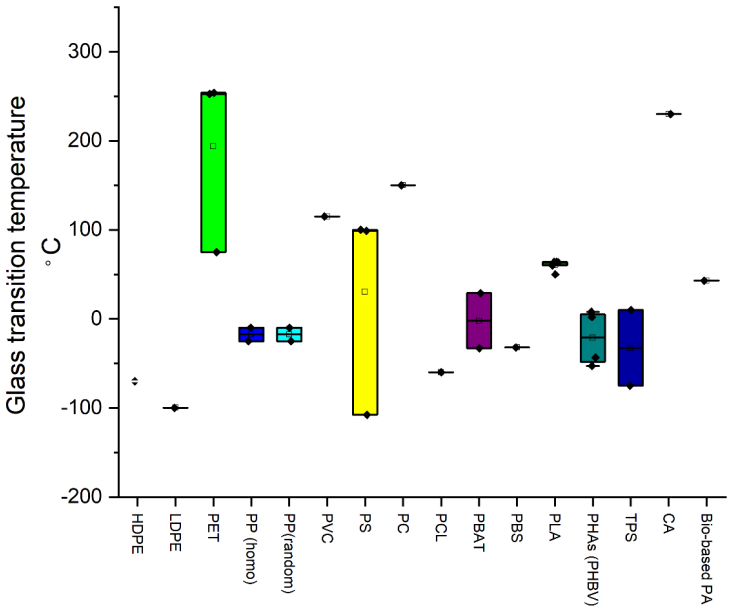


Figure 3.3 Glass transition temperature (ref [19,38,51,56–58-22,33,42,59–61])

## 3.2.3 Chemical properties

The chemical properties of a polymer are critical for determining its long-term durability, performance, and aesthetic stability in common consumer use environments. Therefore, evaluates the material's response to several key environmental factors. The resistance of moisture and water absorption is considered, a parameter particularly relevant for applications in high-humidity settings or where frequent contact with water is expected. Additionally, to address diverse usage conditions, the material's resilience to common household products, including substances under weakly acidic or alkaline conditions, is assessed. Finally, since many products may be exposed to direct or indirect sunlight over their lifespan, resistance to degradation from ultraviolet (UV) radiation is included as a crucial parameter for evaluating long-term material integrity.

### *Water absorption*

Water/moisture absorption is the capacity of a polymer to absorb moisture from its environment. Absorbed moisture shows to act as a plasticizer, reducing the polymer's glass transition temperature and strength. However, absorbed water also can lead to irreversible degradation of the polymer structure. Water/moisture absorption can be expressed as increase in weight percent or weight gain percent of a polymer specimen under the testing procedures. In this section, the water absorption results are summarized in different environments during 24h, which are immersed polymer specimen in water during 24 hours at 23°C and 100°C, exposed to a 50% relative humidity environment at 23°C for 24 hours[62]. Figure 3.4 shows the water absorption of different polymers, most polymers (HDPE, LDPE, PET, PP, PVC, PS, PC, PC, PBAT, and PBS) have a low water absorbance of below 0.35%. The data of PHAs is slightly high about 0.7%. PLA and bio-based PA are higher, which are 1%,1.3% respectively. CA and TPS are much higher than others, reaching 2.5% and 2%.

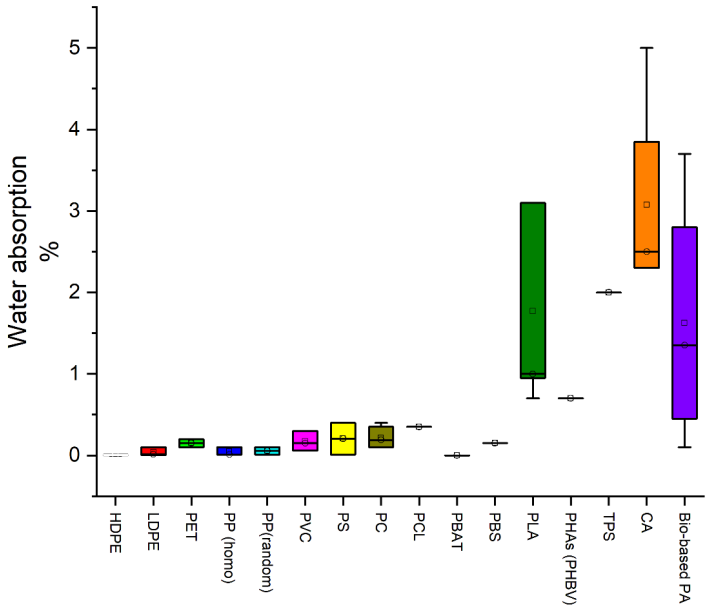


Figure 3.4 Water absorption of different polymers (ref [16,19,22,25,60,62–64-65])

## *Chemical resistance*

The chemical resistance of a polymer is a critical factor for products exposed to common household chemicals or environmental conditions like sunlight. Therefore, this analysis focuses on resistance to weak acids, weak alkalis, and UV radiation. A comparison of these properties for the selected polymers is presented in Figure 3.5. For this comparison, a scoring system is used where performance is graded on a scale of one to five, with five representing the best property. A review of existing literature[16,66–68] revealed that detailed chemical resistance data for weak acids, weak alkalis, and UV radiation is more readily available for fossil-based polymers than for many bio-based polymers. To facilitate a broader comparison, an overall chemical resistance level reported by Zhao et al. is utilize[16], which covers several of the selected fossil- and bio-based polymers. The overall scores presented in Figure 3.5 are based on the level system reported by Zhao et al.,[16] whereas the other properties are evaluated using specific data reported in the literature[16,66–68]. The analysis shows specific vulnerabilities for certain materials; for instance, PET demonstrates poor resistance to weak alkalis, while both HDPE and PS exhibit poor resistance to UV radiation. PLA exhibits moderate overall resistance to UV radiation.

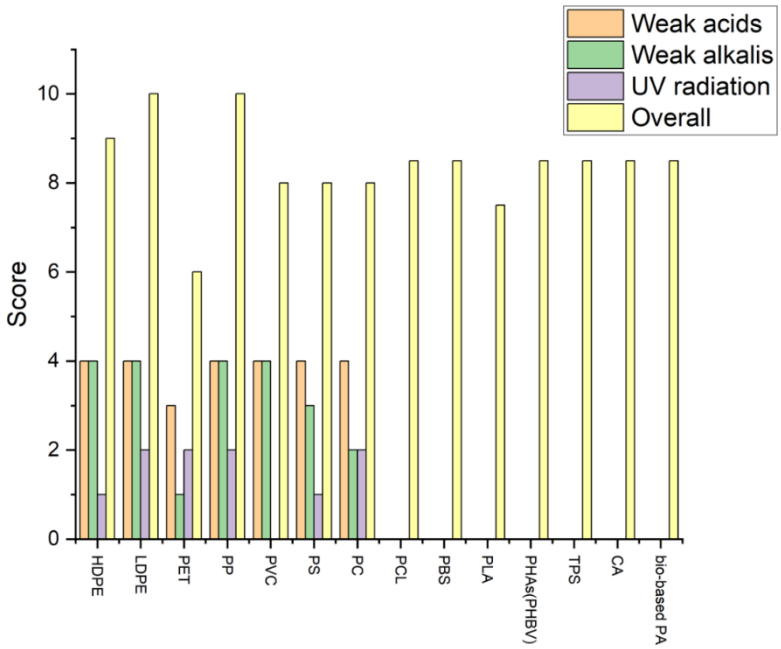


Figure 3.5 Chemical resistance of different polymers (ref [16,66–68])

### 3.2.4 Environmental analysis

LCA is used to determine the environmental impacts of products, processes or services, and all the stages of life cycle are considered (from cradle to grave) [14]. Among them, the key parameters are energy use, $CO_2$ emission and the number of times a polymer can be mechanically recycled, which are shown in Table 3.2. Generally, PCL is weak at $CO_2$ emission and energy use. PC, bio-based PA, and bio-based PBS are weak at $CO_2$ emission. HDPE and LDPE are the best at $CO_2$ emission (score 5) and performs at a medium level on the energy use (score 3). PC, PBAT, PBS, TPS, and CA are good at energy use (score 5), within which, PLA, PBAT, TPS, and CA are also good at $CO_2$ emission (score 4) with PC and PBS are weak at $CO_2$ emission (score 1 and 2 respectively).

## 3.3 Overall evaluation based on decision matrix

The decision matrix (Table 3.2) integrates mechanical, thermal, chemical, and life-cycle indicators into a single five-point scoring scheme in order to identify polymers that combine using performance with credible circular economy potential. The matrix reveals that several conventional fossil-based polymers exhibit excellent overall technical performance. For the mechanical and thermal property, tensile strength, elongation and melting temperature were chosen to compare, which is the lowest standard to avoid breakage and being melted. The score for the property parameters is divided into five grades, the best property is recorded as 5, and the scores are sorted to 1 in descending order. If a material has a range of values for tensile strength, elongation at break, water adsorption, $CO_2$ emission, or energy usage, the middle value is used to represent the performance. To define a score, the maximum value is selected and the range is divided into five intervals, and then gave them the score. For the chemical resistance, some data are still unavailable, for the final evaluation, some values were approximated. Some bio-based polymers didn't have detailed data for each property, but they had a total chemical medical resistance rank with others together, so a score was based on it. The chemical resistance of PBAT, PBAT can be used as a substitute for polyethylene (PE) and is very similar to LDPE in its properties, so we use the value of LDPE. For the LCA energy of bio-based PA and bio-based PBS, the value of PA 11 was chosen, and PBS, because they have similar properties. Notably, HDPE achieves the highest rating of 'E' (Excellent), while materials such as LDPE, However, from a strategic perspective focuses on advancing a truly sustainable circular economy, the reliance of these materials on non-renewable fossil fuels presents a fundamental limitation. For example, while PC has excellent thermal properties (Melting Temperature score of 5), its environmental profile is severely compromised by a very poor $CO_2$ score of 1. The inherent trade-offs suggest

that while fossil-based polymers serve as important performance benchmarks, for research aimed at developing next-generation sustainable technologies, focusing on bio-based alternatives is a more forward-looking approach.

Table 3.2 Decision matrix for the overall evaluation of polymer properties based on mechanical, thermal, chemical, and life-cycle analysis criteria[7,14,16,19,20,22-31,66-68]

| Polymers | Mechanical and thermal | | | Chemical | | | | Life-cycle analysis | | Evaluation* |
|---|---|---|---|---|---|---|---|---|---|---|
| | Tensile strength* | Elongation* | Melting temperature* | Weak Acids* | Weak Alkalis* | UV Radiation* | Water adsorption* | $CO_2$* | Energy* | |
| *Fossil-based* | | | | | | | | | | |
| HDPE | 2 | 5 | 4 | 4 | 4 | 1 | 4 | 5 | 3 | E |
| LDPE | 1 | 4 | 3 | 4 | 4 | 2 | 4 | 5 | 3 | G |
| PET | 5 | 2 | 4 | 3 | 1 | 2 | 4 | 4 | 2 | G |
| PP | 3 | 1 | 4 | 4 | 4 | 2 | 4 | 4 | 3 | G |
| PVC | 4 | 2 | 2 | 4 | 4 | NA | 4 | 4 | 3 | G |
| PS | 4 | 1 | 5 | 4 | 3 | 1 | 4 | 3 | 3 | G |
| PC | 4 | 2 | 5 | 4 | 2 | 2 | 4 | 1 | 5 | G |
| PCL (biodegradable) | 2 | 5 | 2 | >8 | | | 4 | 1 | 1 | F |
| PBAT (biodegradable) | 2 | 5 | 3 | NA | | | NA | 4 | 5 | >F |
| PBS (biodegradable) | 3 | 1 | 3 | >8 | | | 4 | 2 | 5 | G |
| *Bio-based* | | | | | | | | | | |
| **PLA** | **5** | **1** | **4** | **<8** | | | **3** | **4** | **3** | **G** |
| PHAs (PHBV) | 3 | 1 | 3 | <8 | | | 3 | 2 | 2 | F |
| TPS | 1 | 1 | 3 | >8 | | | 1 | 4 | 5 | P |
| CA | 3 | 1 | 5 | >8 | | | 1 | 4 | 5 | F |
| bio-based PA | 4 | 1 | 5 | >8 | | | 2 | 1 | NA | >P |
| bio-based PET | 5 | 2 | 4 | 3 | 1 | 2 | 4 | 3 | 2 | G |
| bio-based PBS | 3 | 1 | 3 | >8 | | | 4 | 1 | NA | >P |

*Tensile strength (MPa): "1": 0-14, "2": 15-29, "3":30-44, "4": 45-58,"5": 59-72
*Elongation (%): "1": 0-100, "2": 101-201, "3":202-302, "4": 303-403,"5": 404-504
*Melting temperature (℃): "1": 0-53, "2": 54-107, "3":108-161, "4": 162-215,"5": 216-269
*Weak Acids, weak alkalis, UV radiation (rank): "1": poor, "2": fair, "3": good. "4": excellent
*Water adsorption (%): "1": 2.5-1.875, "2": 1.874-1.249, "3":1.248-0.623, "4": 0.622-0
*$CO_2$ (kg): "1": 5.6-6.9, "2":4.2-5.5, "3":2.8-4.1, "4": 1.4-2.7,"5": 0-1.3
*Energy (MJ/kg): "1": 68-84, "2":51-67, "3":34-50, "4": 17-33,"5": 0-16
*Evaluation order: 'E' (Excellent)> 'G' (Good)>'F' (Fair)>'P' (Poor).

Turning to the bio-based polymers in Table 3.2, in terms of sustainability metrics (LCA), the overall performance is satisfactory. However, the material exhibits relative weakness in mechanical and thermal properties, particularly in elongation. This implies that the material is more brittle and prone to damage. PLA holds significant potential in conducting in-depth research within the field of advanced chemical recycling technologies. PLA matches high-performance fossil polymers such as PET with a tensile-strength score of 5, maintains an adequate melting-temperature score (4), and posts a comparatively favourable $CO_2$ score (4). The matrix also highlights PLA's principal drawback which is an elongation at break score of 1, signalling brittleness. It should not be ignored that the brittleness has impacted the application scenarios of PLA, yet various modification methods have also broadened its market scope.

## 3.4 Conclusions

This chapter conducts a systematic, multi-criteria comparative analysis of seventeen common fossil- and bio-based polymers to identify a primary candidate for advanced recycling research. The evaluation reveals that while conventional polymers such as HDPE and PVC exhibit excellent overall technical performance profiles, their utility in developing next-generation sustainable systems is constrained by their fossil-fuel origins and specific environmental trade-offs.

PLA is demonstrated as a unique combination of a renewable feedstock, a significant and growing market presence, strong baseline mechanical properties like high tensile strength, and a well-defined set of challenges, notably brittleness and the need for an efficient closed-loop recycling system. These identifies weaknesses, rather than being disqualifying, provide a clear and compelling motivation for the research presented herein.

Therefore, having established PLA as the most strategic material for this study, the subsequent chapters will now focus on the development, simulation, and analysis of a novel chemical recycling process designed to address these challenges and advance the circular economy for PLA.

# References


(1) MEHMET DEMIROR. STYRENE POLYMERS AND COPOLYMERS. Appl. Polym. Sci. 21st Century 2000, 93–106. https://doi.org/10.1016/B978-008043417-9/50009-X.

(2) Polyethylene - HDPE Market Report. https://www.ceresana.com/en/market-studies/plastics/polyethylene-hdpe/.

(3) Polyethylene LDPE Market Report. https://www.ceresana.com/en/market-studies/plastics/polyethylene-ldpe/.

(4) BASF Corporation, Mt. Olive, New Jersey, USA. Plasticizers. Encycl. Phys. Sci. Technol. Third Ed. 2003, 441–456. https://doi.org/10.1016/B0-12-227410-5/00586-X.

(5) G.L. Robertson. Food Packaging. Encycl. Agric. Food Syst. 2014, 232–249. https://doi.org/10.1016/B978-0-444-52512-3.00063-2.

(6) Polypropylene Market Report. https://www.ceresana.com/en/market-studies/plastics/polypropylene/polypropylene-market-share-capacity-demand-supply-forecast-innovation-application-growth-production-size-industry.html.

(7) Jia, P.; Feng, G.; Bo, C.; Hu, L.; Yang, X.; Zhang, L.; Zhang, M.; Zhou, Y. A Composition of Phosphaphenanthrene Groups-Containing Castor-Oil-Based Phosphate Plasticizer for PVC: Synthesis, Characterization and Property. J. Ind. Eng. Chem. 2018, 60, 192–205. https://doi.org/10.1016/j.jiec.2017.11.006.

(8) Hacker, M. C.; Mikos, A. G. Synthetic Polymers. In Principles of Regenerative Medicine; Elsevier, 2011; pp 587–622. https://doi.org/10.1016/B978-0-12-381422-7.10033-1.

(9) Mohit Singh. Biocompatible Thermoplastics as Implants/Scaffold. Ref. Module Mater. Sci. Mater. Eng. 2020. https://doi.org/10.1016/B978-0-12-820352-1.00012-2.

(10) Ranvijay Kumar. Hydrogel-Nanofiber Composites for Tissue Reconstruction Applications: A State of the Art Review. Ref. Module Mater. Sci. Mater. Eng. https://doi.org/10.1016/B978-0-12-820352-1.00251-0.

(11) Lule, Z. C.; Kim, J. Properties of Economical and Eco-Friendly Polybutylene Adipate Terephthalate Composites Loaded with Surface Treated Coffee Husk. Compos.

Part Appl. Sci. Manuf. 2021, 140, 106154. https://doi.org/10.1016/j.compositesa.2020.106154.

(12) Michael Niaounakis. Biopolymers: Applications and Trends; 3 - Packaging.

(13) Philippe Colomban. Handbook of Properties of Textile and Technical Fibres (Second Edition),5 - Silk: Fibers, Films, and Composites—Types, Processing, Structure, and Mechanics,; In The Textile Institute Book Series,.

(14) Cosate de Andrade, M. F.; Souza, P. M. S.; Cavalett, O.; Morales, A. R. Life Cycle Assessment of Poly(Lactic Acid) (PLA): Comparison Between Chemical Recycling, Mechanical Recycling and Composting. J. Polym. Environ. 2016, 24 (4), 372–384. https://doi.org/10.1007/s10924-016-0787-2.

(15) He, Y.; Hu, Z.; Ren, M.; Ding, C.; Chen, P.; Gu, Q.; Wu, Q. Evaluation of PHBHHx and PHBV/PLA Fibers Used as Medical Sutures. J. Mater. Sci. Mater. Med. 2014, 25 (2), 561–571. https://doi.org/10.1007/s10856-013-5073-4.

(16) Zhao, X.; Cornish, K.; Vodovotz, Y. Narrowing the Gap for Bioplastic Use in Food Packaging: An Update. Environ. Sci. Technol. 2020, 54 (8), 4712–4732. https://doi.org/10.1021/acs.est.9b03755.

(17) Helping to Revent Bioplastics. https://www.sukano.com/en/applications/biopolymers/bio-based-pbs.

(18) Zarandi, M. H. F.; Mansour, S.; Hosseinijou, S. A.; Avazbeigi, M. A Material Selection Methodology and Expert System for Sustainable Product Design. Int. J. Adv. Manuf. Technol. 2011, 57 (9–12), 885–903. https://doi.org/10.1007/s00170-011-3362-y.

(19) Rosenboom, J.-G.; Langer, R.; Traverso, G. Bioplastics for a Circular Economy. Nat. Rev. Mater. 2022, 7 (2), 117–137. https://doi.org/10.1038/s41578-021-00407-8.

(20) Crompton; Thomas Roy. Physical Testing of Plastics; Smithers Rapra, 2012.

(21) S.R. Djafari Petroudy,. Advanced High Strength Natural Fibre Composites in Construction; 3 - Physical and mechanical properties of natural fibers; Woodhead Publishing, 2017.

(22) Low Plasticizer CA. https://www.makeitfrom.com/material-properties/Low-Plasticizer-CA.

(23) Lu, N.; Swan, R. H.; Ferguson, I. Composition, Structure, and Mechanical Properties of Hemp Fiber Reinforced Composite with Recycled High-Density Polyethylene Matrix. J. Compos. Mater. 2012, 46 (16), 1915–1924. https://doi.org/10.1177/0021998311427778.

(24) Jung, C.-H.; Lee, D.-H.; Hwang, I.-T.; Im, D.-S.; Shin, J.; Kang, P.-H.; Choi, J.-H. Fabrication and Characterization of Radiation-Resistant LDPE/MWCNT Nanocomposites. J. Nucl. Mater. 2013, 438 (1–3), 41–45. https://doi.org/10.1016/j.jnucmat.2013.03.023.

(25) Maddah, H. A. Polypropylene as a Promising Plastic: A Review. 12.

(26) Zhu, A.; Cai, A.; Zhou, W.; Shi, Z. Effect of Flexibility of Grafted Polymer on the Morphology and Property of Nanosilica/PVC Composites. Appl. Surf. Sci. 2008, 254 (13), 3745–3752. https://doi.org/10.1016/j.apsusc.2007.11.042.

(27) Hongdilokkul, P.; Keeratipinit, K.; Chawthai, S.; Hararak, B.; Seadan, M.; Suttiruengwong, S. A Study on Properties of PLA/PBAT from Blown Film Process. IOP Conf. Ser. Mater. Sci. Eng. 2015, 87, 012112. https://doi.org/10.1088/1757-899X/87/1/012112.

(28) Zhou, X. Injection Molded Bioplastics From Plasticized Soy Meal And Biodegradable Polymer Blends. 91.

(29) Modi, S.; Koelling, K.; Vodovotz, Y. Assessing the Mechanical, Phase Inversion, and Rheological Properties of Poly-[(R)-3-Hydroxybutyrate-Co-(R)-3-Hydroxyvalerate] (PHBV) Blended with Poly-(l-Lactic Acid) (PLA). Eur. Polym. J. 2013, 49 (11), 3681–3690. https://doi.org/10.1016/j.eurpolymj.2013.07.036.

(30) Zhang, K.; Mohanty, A. K.; Misra, M. Fully Biodegradable and Biorenewable Ternary Blends from Polylactide, Poly(3-Hydroxybutyrate-Co-Hydroxyvalerate) and Poly(Butylene Succinate) with Balanced Properties. ACS Appl. Mater. Interfaces 2012, 4 (6), 3091–3101. https://doi.org/10.1021/am3004522.

(31) Elongation at Break. https://omnexus.specialchem.com/polymer-properties/properties/elongation-at-break.

(32) In Micro and Nano Technologies; 2019.

(33) Gindl, W.; Keckes, J. Tensile Properties of Cellulose Acetate Butyrate Composites Reinforced with Bacterial Cellulose. Compos. Sci. Technol. 2004, 64 (15), 2407–2413. https://doi.org/10.1016/j.compscitech.2004.05.001.

(34) Sobczak, L.; Lang, R. W.; Haider, A. Polypropylene Composites with Natural Fibers and Wood – General Mechanical Property Profiles. Compos. Sci. Technol. 2012, 72 (5), 550–557. https://doi.org/10.1016/j.compscitech.2011.12.013.

(35) Modi, S. J.; Cornish, K.; Koelling, K.; Vodovotz, Y. Fabrication and Improved Performance of Poly(3-Hydroxybutyrate-Co-3-Hydroxyvalerate) for Packaging by Addition of High Molecular Weight Natural Rubber. J. Appl. Polym. Sci. 2016, 133 (37). https://doi.org/10.1002/app.43937.

(36) Farah, S.; Anderson, D. G.; Langer, R. Physical and Mechanical Properties of PLA, and Their Functions in Widespread Applications — A Comprehensive Review. Adv. Drug Deliv. Rev. 2016, 107, 367–392. https://doi.org/10.1016/j.addr.2016.06.012.

(37) Aghvami-Panah, M.; Panahi-Sarmad, M.; Seraji, A. A.; Jamalpour, S.; Ghaffarian, S. R.; Park, C. B. LDPE/MWCNT and LDPE/MWCNT/UHMWPE Self-Reinforced Fiber-Composite Foams Prepared via Supercritical CO2: A Microstructure-Engineering Property Perspective. J. Supercrit. Fluids 2021, 174, 105248. https://doi.org/10.1016/j.supflu.2021.105248.

(38) Polycaprolactone (PCL). https://www.makeitfrom.com/material-properties/Polycaprolactone-PCL.

(39) Polylactic Acid (PLA, Polylactide). https://www.makeitfrom.com/material-properties/Polylactic-Acid-PLA-Polylactide.

(40) Young's Modulus. https://omnexus.specialchem.com/polymer-properties/properties/young-modulus.

(41) W. Brantley; D. Berzins; M. Iijima; E. Tufekçi; Z. Cai. Orthodontic Applications of Biomaterials; Woodhead Publishing, 2017.

(42) Teymoorzadeh, H.; Rodrigue, D. Biocomposites of Wood Flour and Polylactic Acid: Processing and Properties. J. Biobased Mater. Bioenergy 2015, 9 (2), 252–257. https://doi.org/10.1166/jbmb.2015.1510.

(43) Diop, M. F.; Burghardt, W. R.; Torkelson, J. M. Well-Mixed Blends of HDPE and Ultrahigh Molecular Weight Polyethylene with Major Improvements in Impact Strength Achieved via Solid-State Shear Pulverization. Polymer 2014, 55 (19), 4948–4958. https://doi.org/10.1016/j.polymer.2014.07.050.

(44) Flexural Strength Testing of Plastics. https://www.matweb.com/reference/flexuralstrength.aspx.

(45) Brown, P. H.; Balbo, A.; Zhao, H.; Ebel, C.; Schuck, P. Density Contrast Sedimentation Velocity for the Determination of Protein Partial-Specific Volumes. PLoS ONE 2011, 6 (10), e26221. https://doi.org/10.1371/journal.pone.0026221.

(46) Kwon, S.; Kim, K. J.; Kim, H.; Kundu, P. P.; Kim, T. J.; Lee, Y. K.; Lee, B. H.; Choe, S. Tensile Property and Interfacial Dewetting in the Calcite Filled HDPE, LDPE, and LLDPE Composites. Polymer 2002, 43 (25), 6901–6909. https://doi.org/10.1016/S0032-3861(02)00399-3.

(47) Limami, H.; Manssouri, I.; Cherkaoui, K.; Saadaoui, M.; Khaldoun, A. Thermal Performance of Unfired Lightweight Clay Bricks with HDPE & PET Waste Plastics Additives. J. Build. Eng. 2020, 30, 101251. https://doi.org/10.1016/j.jobe.2020.101251.

(48) Huang, S. Viscoelastic Property of an LDPE Melt in Triangular- and Trapezoidal-Loop Shear Experiment. Polymers 2021, 13 (22), 3997. https://doi.org/10.3390/polym13223997.

(49) Dominick Rosato. Plastics Engineered Product Design; 1 - OVERVIEW; Elsevier Science, 2003.

(50) Technical Information. https://www.daicel.com/cell_ac/en/detail/.

(51) Jiang, L.; Liu, B.; Zhang, J. Properties of Poly(Lactic Acid)/Poly(Butylene Adipate-Co -Terephthalate)/Nanoparticle Ternary Composites. Ind. Eng. Chem. Res. 2009, 48 (16), 7594–7602. https://doi.org/10.1021/ie900576f.

(52)Purohit, P. J.; Huacuja-Sánchez, J. E.; Wang, D.-Y.; Emmerling, F.; Thünemann, A.; Heinrich, G.; Schönhals, A. Structure–Property Relationships of Nanocomposites Based

on Polypropylene and Layered Double Hydroxides. Macromolecules 2011, 44 (11), 4342–4354. https://doi.org/10.1021/ma200323k.

(53) Clarizio, S. C.; Tatara, R. A. Tensile Strength, Elongation, Hardness, and Tensile and Flexural Moduli of Injection-Molded TPS Filled with Glycerol-Plasticized DDGS. J. Polym. Environ. 2013, 21 (3), 623–630. https://doi.org/10.1007/s10924-013-0607-x.

(54) Su, S.; Kopitzky, R.; Tolga, S.; Kabasci, S. Polylactide (PLA) and Its Blends with Poly(Butylene Succinate) (PBS): A Brief Review. Polymers 2019, 11 (7), 1193. https://doi.org/10.3390/polym11071193.

(55) Selection of Polymeric Materials; 3 - Thermal Properties of Polymeric Materials,; William Andrew Publishing, 2008.

(56) Maldas, D.; Kokta, B. V.; Daneault, C. Influence of Coupling Agents and Treatments on the Mechanical Properties of Cellulose Fiber–Polystyrene Composites. J. Appl. Polym. Sci. 1989, 37 (3), 751–775. https://doi.org/10.1002/app.1989.070370313.

(57) Xu, J.; Guo, B.-H. Poly(Butylene Succinate) and Its Copolymers: Research, Development and Industrialization. Biotechnol. J. 2010, 5 (11), 1149–1163. https://doi.org/10.1002/biot.201000136.

(58) Sharma, M.; Kumar, V.; Gupta, A. P. Thermoplastic Starch (TPS) Based Bio-Disintegrable Polymers - Combination of Modified Potato Starch with Polyolefins. 2013, 4 (10), 5.

(59) Bhushan, B.; Kumar, R. Plasma Treated and Untreated Thermoplastic Biopolymers/Biocomposites in Tissue Engineering and Biodegradable Implants. In Materials for Biomedical Engineering; Elsevier, 2019; pp 339–369. https://doi.org/10.1016/B978-0-12-816901-8.00011-0.

(60) Polycarbonate (PC). https://www.makeitfrom.com/material-properties/Polycarbonate-PC.

(61) Di Lorenzo, M. L.; Longo, A.; Androsch, R. Polyamide 11/Poly(Butylene Succinate) Bio-Based Polymer Blends. Materials 2019, 12 (17), 2833. https://doi.org/10.3390/ma12172833.

(62) Water Absorption 24 Hours. https://omnexus.specialchem.com/polymer-properties/properties/water-absorption-24-hours.

(63) Mohanty, S.; Verma, S.; Nayak, S. Dynamic Mechanical and Thermal Properties of MAPE Treated Jute/HDPE Composites. Compos. Sci. Technol. 2006, 66 (3–4), 538–547. https://doi.org/10.1016/j.compscitech.2005.06.014.

(64) High Plasticizer CA. https://www.makeitfrom.com/material-properties/High-Plasticizer-CA.

(65) Gáspár, M.; Benkő, Zs.; Dogossy, G.; Réczey, K.; Czigány, T. Reducing Water Absorption in Compostable Starch-Based Plastics. Polym. Degrad. Stab. 2005, 90 (3), 563–569. https://doi.org/10.1016/j.polymdegradstab.2005.03.012.

(66) Polyesters and Polyamides, 1. publ.; Deopura, B. L., Textile Institute, Eds.; Woodhead publishing in textiles; CRC Press: Boca Raton, 2008.

(67) Chemical & Environmental Resistance of Thermoplastics. https://www.rtpcompany.com/technical-info/chemical-resistance/.

(68) Chemical Charts. https://www.calpaclab.com/chemical-compatibility-charts/.

# Chapter 4

# One-pot Synthesis of MLA -to-LD Process

Chapter 3 has demonstrated that PLA is a good plastic for a plastic circular economy, in this chapter, the challenge step of PLA circular economy will be investigated, which is methyl lactate (MLA) to lactide (LD). A one-pot liquid-phase process from MLA to LD is built, which simply the reaction set-up, compared the catalytic performance of Titania-silica ($TiO_x/SiO_2$) and $TiO_2$. The $TiO_x/SiO_2$ and $TiO_2$ structure is explored, a series of catalyst characterisation to correlate the Ti active sites distribution, the relation between Ti and silica support, the valence states of Ti effect. Because of the better selectivity and conversion of $TiO_x/SiO_2$, Ti(III) active sites and Ti-O-Si bonds are found in $TiO_x/SiO_2$ catalyst, compares with $TiO_2$ catalyst, only exist Ti(IV) and no silica support, which suggests Ti(III)-O-Si structure play a key role in transesterification reaction. Based on the experiment outcomes, the $TiO_x/SiO_2$ catalyst was then selected for transition state (TS) searching and energy barrier calculations by DFT, thereby establishing the reaction pathway. This work explains the unique Ti(III)-O-Si structure for constructing efficient catalysts and the rate-limiting step of the MLA to LD reaction, the catalyst property and transesterification mechanism might bring some inspiration in the further reactor optimization, and widely catalytic esterification or transesterification reaction area.

# 4.1 Methodology

## 4.1.1 Catalyst Preparation

$TiO_x/SiO_2$ catalysts were prepared by wet impregnation of a high surface $SiO_2$ support with a titanium precursor solution, adapted from a reported procedure with minor modifications[1]. The details have been described in Section 2.1.2.

$TiO_2$ catalyst was purchased from Thermo Scientific Chemicals, anatase-phase powder, purity 98+%. Prior to use, the as-received powder was spread in a shallow glass dish and dried in the oven for 10 h to remove moisture[1,2]. After cooling to room temperature, the material was transferred to a sealed container to minimise moisture ingress.

## 4.1.2 Catalyst Characterization

The powder X-ray diffraction (XRD) patterns of samples were measured in a MiniFlex600 instrument, operated at 40kV-15mA, recorded in a 2θ angle ranging from 3° to 60° with a step size of 0.02°[3]. Scanning electron microscopy (SEM) was carried out on a HITACHI S4800. Transmission electron microscopy (TEM) and Scanning transmission electron microscopy with energy-dispersive X-ray spectroscopy (STEM-EDS) mapping were obtained by using a FEI Tecnai G2 F30 microscope. X-ray photoelectron spectroscopy (XPS) measurements were performed on a Thermo Escalab 250XI. The spectra were referenced to C(1s) at a binding energy of 284.8 eV[4]. The $N_2$ adsorption-desorption isotherms were measured at 77 K using ASAP 2460. The surface area was calculated by Brunauer–Emmett–Teller (BET) method using desorption data. The distribution of pore size and pore volume was calculated by the Barrett, Joyner, and

Halenda (BJH) method using adsorption data. The FT-IR spectrum of each sample was recorded using an MB3000 FT-IR Laboratory Analyzer from 700 to 1100 $cm^{-1}$ with a resolution of 7.7 $cm^{-1}$ [5].

### 4.1.3 Catalytic Reaction and Product Analysis

Reactions were carried out in a 50 mL three-neck round-bottom flask seated in an aluminium heating block on a hot plate. One neck was equipped with a $N_2$ inlet to purge the reactor and maintain an inert atmosphere, thereby minimizing moisture and air interference. Another neck was connected tubing to an absorption trap containing dichloromethane (DCM, 44 mL) spiked with o-xylene (1.0 mL, purity of 99%) as an internal standard, the outlet was positioned below the solvent surface so that gaseous/volatile products were continuously bubbled into the DCM solution for subsequent analysis. The third neck is for adding reactant and catalyst. After thoroughly purging the assembled system with dry $N_2$, the flask was charged with MLA (2.0 mL, 97%) and heated to the target temperature (170, 200, or 220 °C). The vaporized MLA was collected in the DCM/o-xylene trap. Once the setpoint was reached and stabilized, the catalyst (100 mg) was introduced rapidly, the reaction time was started, and the mixture was allowed to proceed for 30 min while maintaining the $N_2$ input and product collection through a new DCM/o-xylene trap. At the end of the run, heating was stopped and the system was allowed to cool to ambient temperature before work-up and analysis. All transfers and connections were kept dry, and the same reactor and trap configuration was used for each temperature to ensure comparability.

After the reaction for 2h, the collection products were tested by gas chromatography−mass spectrometry (GC−MS) with an HP-5 capillary column (30 m ×

320 μm × 0.25 μm) for qualitative inorganic analysis[6], and gas chromatograph equipped with a flame ionization detector (GC-FID) for quantitative analysis[7]. The conversion of MLA was calculated by internal standard method, calibration curves were established from standard solutions of MLA in the presence of the same internal standard concentration. Because several volatile products included unsure oligomeric for which authentic standards and reliable FID response factors were unavailable, product selectivity are reported as GC-FID area-normalized distributions. Calculation equations for conversion[8,9] and selectivity[10,11] are showed below:

$$\text{Conversion} = \frac{\text{mol}_{\text{initial MLA}} - \text{mol}_{\text{unreacted MLA}}}{\text{mol}_{\text{initial MLA}}} \quad (4.1)$$

$$\text{Selectivity (detec. products)} = \frac{\text{Area}_{\text{aim product}}}{\text{Area}_{\text{all produtcs}}} \quad (4.2)$$

## 4.1.4 Computational details

For the reaction pathway of MLA to LD part, DFT calculations were carried out by using VASP[12,13] and LASP code[14]. The GGA for the exchange–correlation functional were applied within the PBE formulation[15]. A PAW method[16] is used to depict the electron ion interactions. The valence electronic states were expanded in plane wave basis sets with energy cut-off of 400 eV and K-point grid in the Monkhorst-Pack scheme was used, which was set to (2×2×1). To overcome the issue related to underestimation and delocalize in GGA calculations due to the self-interaction error, DFT+U method[17] was adopted, a Hubbard U value of 4.2 eV was used for the Ti 3d states as well. TSs were searched using both Double-Ended Surface Walking (DESW) method and climbing image nudged elastic band (CI-NEB) method. Convergence criteria were set to $10^{-4}$ eV

per atom for the self-consistent field (SCF) iterations and 0.02 eV/Å for force convergence.

# 4.2 Results and Discussion

## 4.2.1 Catalysts Characterisation

To elucidate the role of the valence and dispersion of Ti control catalytic behaviour, the $TiO_x/SiO_2$ and $TiO_2$ catalysts are prepared for comparison. Figure 4.1 presents the powder XRD patterns of $SiO_2$ support, $TiO_2$, and $TiO_x/SiO_2$. The $SiO_2$ sample exhibits only a broad hump centred at 22° 2θ, characteristic of amorphous silica. The $TiO_2$ pattern, by contrast, displays a series of sharp reflections at 25.3°, 37.8°, 48.0°, 53.9° and 55.1° 2θ, which match well with the (101), (004), (200), (105) and (211) planes of anatase $TiO_2$ (JCPDS 21-1272), confirming its crystalline nature[12]. Notably, the $TiO_x/SiO_2$ catalyst shows no distinct anatase or rutile reflections, its diffraction profile is essentially the superposition of the amorphous-silica and a very weak, broad shoulder around 23° 2θ. The absence of $TiO_2$ peaks indicates that titanium is highly dispersed on the silica support, forming either nanocrystalline domains below the XRD detection limit (~3 nm) or isolated $TiO_x$ sites bonded as Ti–O–Si linkages. These results show that anchoring $TiO_x$ on $SiO_2$ effectively suppresses $TiO_2$ crystallite growth and yields highly dispersed Ti sites that are expected to be catalytically active.

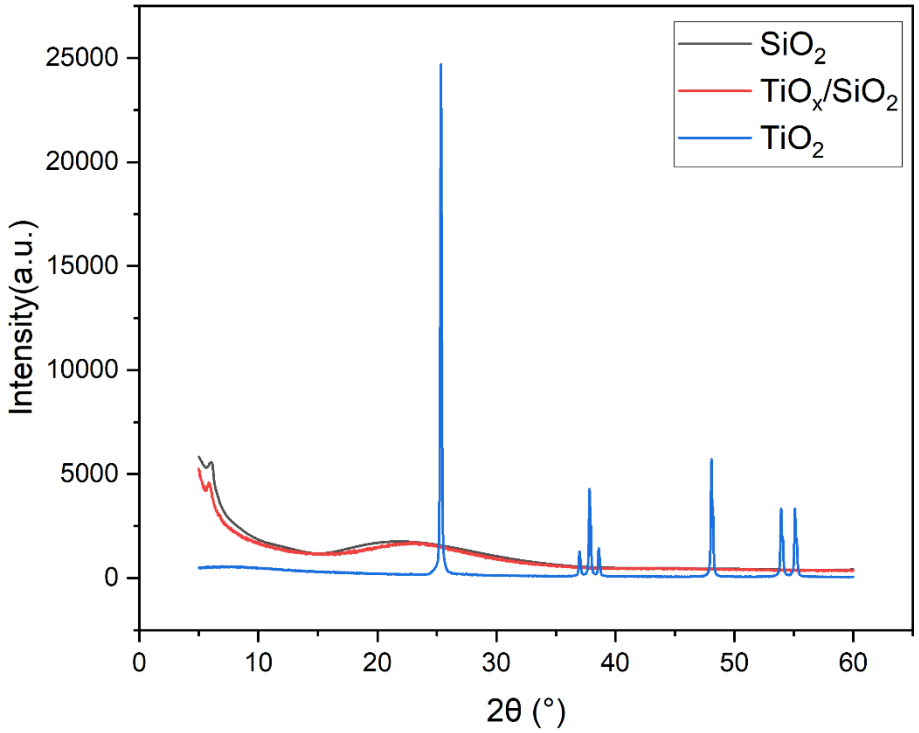


Figure 4.1 XRD patterns of $SiO_2$, $TiO_x/SiO_2$, and $TiO_2$

The SEM imagine of $TiO_x/SiO_2$ (Figure 4.2a) recorded at 3 kV (scale bar = 500 nm) displayed uniformly distributed nano-particles. No textural collapse or sintering is evident, indicating that the impregnation–drying–calcination sequence preserved the intrinsic morphology of the high surface area silica support. Combined the XRD results (no anatase phase in $TiO_x/SiO_2$), which retain the morphology of the silica support. Higher resolution TEM (200 kV, scale bar = 50 nm) was therefore carried out (Figure 4.2b). The micrograph reproduces the SEM observation of uniformly packed particles. Critically, no lattice fringes corresponding to anatase $TiO_2$ are observed anywhere in the field of view. The absence of crystalline fringes, together with the XRD amorphous halo, indicates that titanium is present as highly dispersed $TiO_x$ species on or within the silica (isolated Ti–O–Si sites or sub-nanometric domains) rather than as XRD/TEM-detectable Titania crystallites.

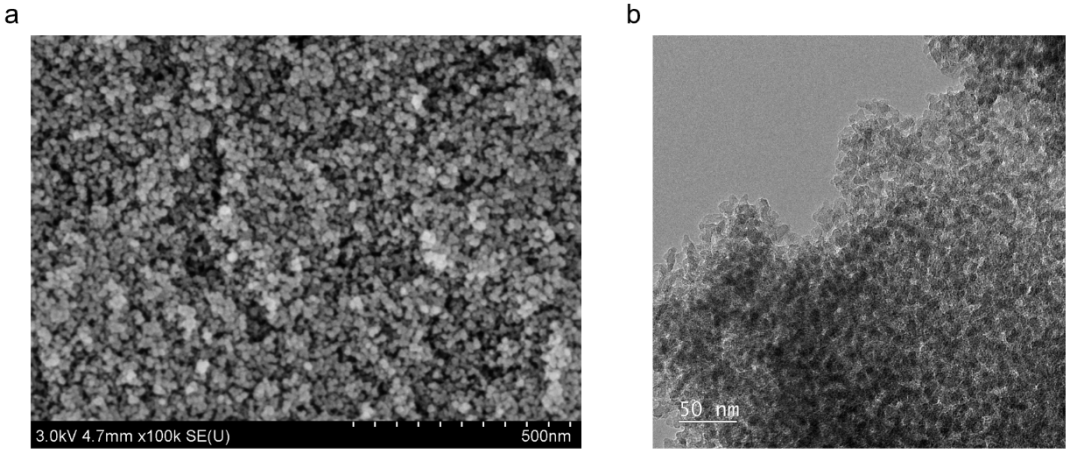


Figure 4.2 SEM and TEM imagines of $TiO_x/SiO_2$ catalyst

(a) SEM imagine; (b) TEM imagine.

Figure 4.3a–d present STEM–EDS elemental maps collected from a representative region of the $TiO_x/SiO_2$ catalyst (scale bar = 1 μm). The overlay (Figure 4.3a) shows that the O and Si signals (Figure 4.3b, c) are coextensive across the particle, consistent with an amorphous silica support. The Ti map (Figure. 4.3d) displays a low-intensity but pervasive signal that tracks the support topography, with no bright "hot spots" or distinct Ti-rich regions at the micron scale. No edge enrichment attributable to Ti nanoparticles is observed, indicating that Ti is distributed uniformly over the silica. Quantification performed over the same field of view (Table 4.1) gives 3.8 wt% Ti (1.61 at%), 44.0 wt% Si, and 52.2 wt% O, corresponding to a Ti/Si atomic ratio of 0.051. The Ti content agrees well with the nominal loading from impregnation (~3 wt%) within the expected uncertainty of local, standardless EDS quantification. The small reported net errors (≤1.7%) together with the absence of Ti-rich features in the maps support the conclusion that titanium is present as highly dispersed $TiO_x$ species throughout the silica support rather than as XRD-detectable Titania crystallites. These observations are fully consistent with the XRD (Figure 4.1, no anatase peaks) and SEM/TEM (Figure 4.2; no

lattice fringes) results, pointing to isolated Ti–O–Si structure or $TiO_x$ domains is the primary Ti environments.

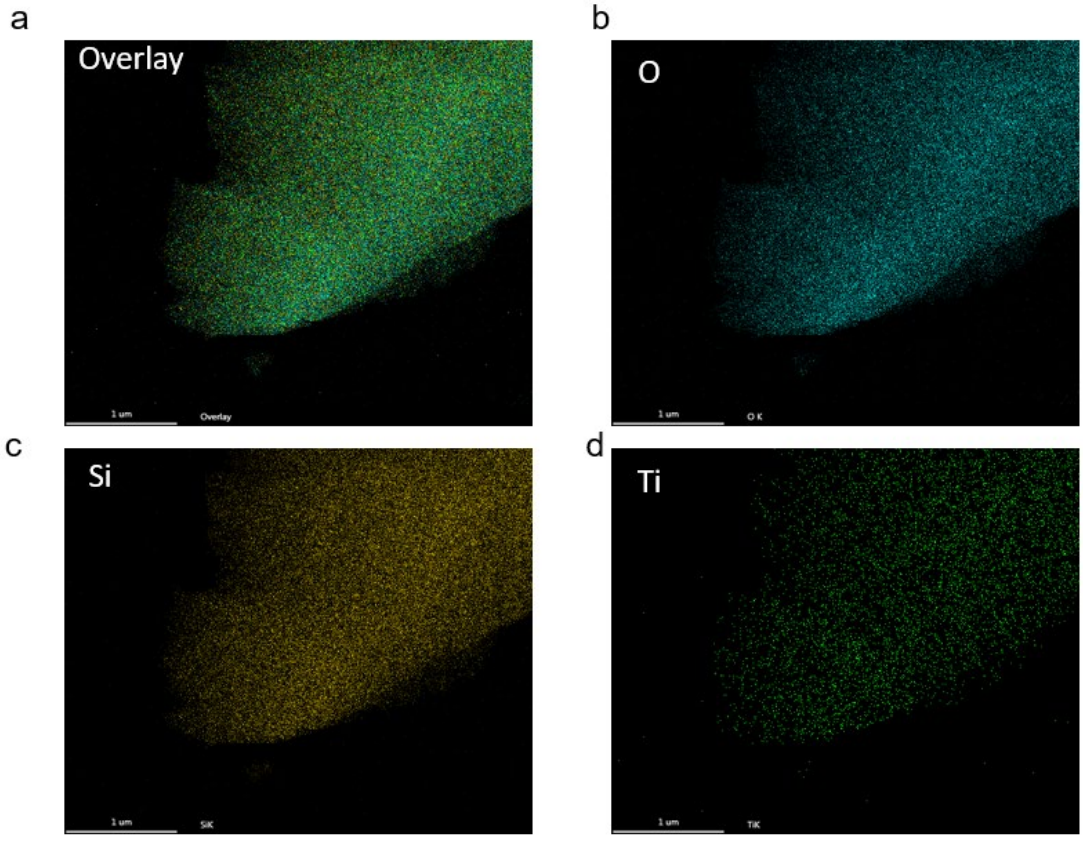


Figure 4.3 STEM-EDS elemental mapping of $TiO_x/SiO_2$

(a) Overlay mapping; (b) O mapping; (c) Si mapping; (d) Ti mapping.

Table 4.1 Quantitative STEM-EDS elemental composition of the $TiO_x/SiO_2$ catalyst

| Element | Weight % | Atomic % | Net Error % |
|---|---|---|---|
| O | 52.18 | 66.45 | 0.33 |
| Si | 44.02 | 31.93 | 0.31 |
| Ti | 3.8 | 1.61 | 1.7 |

XPS was collected for $TiO_x/SiO_2$ and $TiO_2$ to probe the valence of titanium (Figure 4.4). For the crystalline $TiO_2$ reference (Figure 4.4b), the Ti 2p envelope consists of a single spin–orbit doublet at 458.6 and 464.3 eV with a weak satellite at ~472 eV, in excellent agreement with literature values[4], confirming that surface Ti is fully oxidized as Ti(IV). In contrast, the $TiO_x/SiO_2$ spectrum (Figure 4.4a) is broader and asymmetric.

The Ti 2p resolves into four components: a dominant Ti(IV) doublet at 458.8/464.5 eV with its weak satellite, and a lower-binding energy doublet at 456.7/462.2 eV assigned to Ti(III)[4]. The +0.2 eV shift of the Ti(IV) position in $TiO_x/SiO_2$ relative to $TiO_2$ indicates a slightly more electron-deficient environment, consistent with isolated Ti–O–Si structure rather than bulk $TiO_2$. Peak-area integration shows that around 6 % of the surface Ti is present as Ti(III), the remaining 94 % as Ti(IV) in the $TiO_x/SiO_2$ catalyst. The synergy between highly dispersed Ti(IV)-O-Si and a small population of Ti(III)-O-Si sites is the reason of unique activity of $TiO_x/SiO_2$.

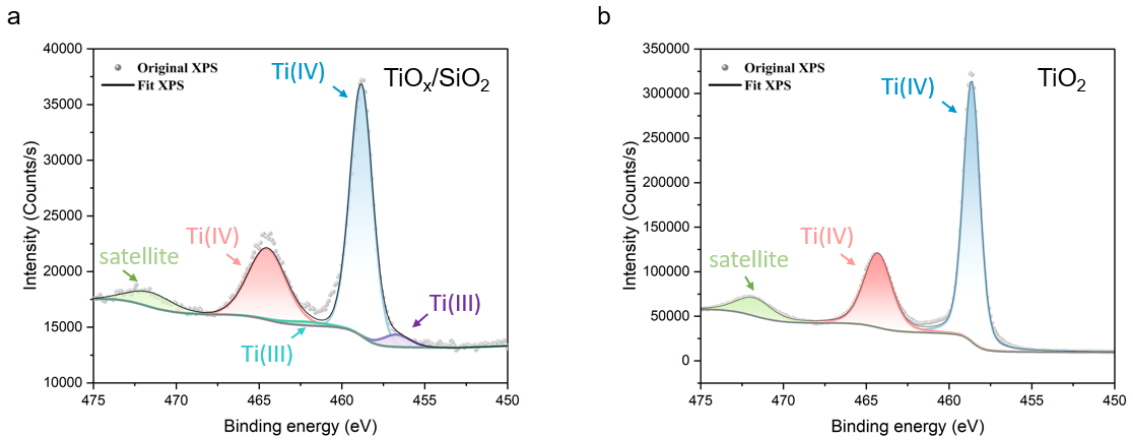


Figure 4.4 XPS spectra of Ti 2p of catalysts

(a) $TiO_x/SiO_2$ (b)$TiO_2$

The FTIR (700–1100 $cm^{-1}$) of $SiO_2$ and $TiO_x/SiO_2$ are compared in Figure 4.5. The $SiO_2$ support shows the expected strong band at ~1035 $cm^{-1}$ assigned to the asymmetric stretching of the Si–O–Si network[13], and a band at ~795 $cm^{-1}$ from the symmetric Si–O–Si stretch or ring-breathing mode[13]. $TiO_x/SiO_2$ (red trace), the band around 1000–900 $cm^{-1}$ broadens and a distinct shoulder/peak emerges at ~945 $cm^{-1}$ that is absent (or only weakly visible) for bare $SiO_2$[14]. This feature is commonly attributed to Ti–O–Si linkages formed by condensation of surface silanols with Ti precursors, indicating that Ti is incorporated as Si-bound $TiO_x$ rather than individual $TiO_2$ crystals.

Concomitantly, the main Si–O–Si band at ~1035 $cm^{-1}$ slightly decreases in relative intensity, and the ~795 $cm^{-1}$ band is modestly enhanced, consistent with a perturbed silica network after grafting. Taken together with previous characterisation, the FTIR data support the presence of highly dispersed Ti–O–Si species on the silica surface as the dominant Ti environment.

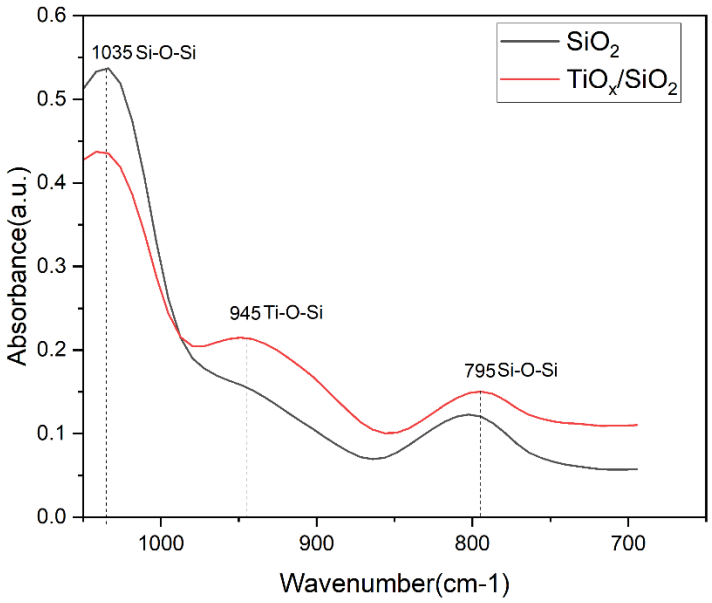


Figure 4.5 FTIR spectra of $TiO_x/SiO_2$ and $SiO_2$

## 4.2.2 Conversion and Selectivity of MLA to LD

Figure 4.6 shows the liquid-phase conversion and selectivity of MLA to LD over $Ti/SiO_2$ and $TiO_2$ at 170–220 °C. At every temperature the $TiO_x/SiO_2$ catalyst is markedly more active, reaching 53.8, 62.9 and 62.3 % MLA conversion (purple line in Figure 4.6), whereas $TiO_2$ cases never exceeds 34.6% and even drops to 25.6 % at 220 °C (pink line in Figure 4.6). The selectivity of products normalised to the GC-FID compounds, highlight the distribution of products. With $TiO_x/SiO_2$, LD selectivity increases from ~38.3 % to ~48.7 %, while the share of higher oligomers falls from ~34.6 % to ~18.1 %. The dimeric intermediate $ML_2A$ decreases only moderately (~21.4 % → ~13.1 %),

indicating that dimer formation is rapid and the ring-closing step becomes increasingly competitive as temperature rises. The small amount of methyl-2-methoxy propionate ($M_2MP$) appears above 200 °C. Methanol (MeOH) selectivity rises from 7.5% to 16.3% at 220 °C. Two factors account for the pronounced methanol build-up: (i) the higher conversion, including partial cleavage of $ML_2A$ and oligomer, produced methanol; (ii) Hydrogen bonding between methanol and surface pore structures of $SiO_2$, which inhibits methanol volatilization and enables its extraction (with DCM) and subsequent GC-FID detection methanol accumulation. The presence of methanol shifts the equilibrium of the key step (2 MLA ⇌ $ML_2A$ + MeOH) toward the left, thereby limiting further LD formation and promoting secondary alcoholysis that yields $M_2MP$. The higher methanol selectivity (16.3%) at 220 °C than the selectivity at 200°C.

$TiO_2$ catalyst behaves markedly differently in the reaction. MLA conversion never exceeds 34.6%, LD selectivity is lower than 13%, $ML_2A$ selectivity is over 79 %, and methanol is essentially absent from the chromatograms. The low methanol signal is attributable to the combination of limited generation (low conversion). These contrasting behaviours corroborate the structural insights from XPS, STEM-EDS and XRD: Ti(IV)-O-Si sites together with Ti(III)-O-Si sites on $TiO_x/SiO_2$ accelerate MLA consumption, steer the reaction toward LD, whereas fully oxidised lattice Ti(IV) in crystalline anatase remains largely inactive.

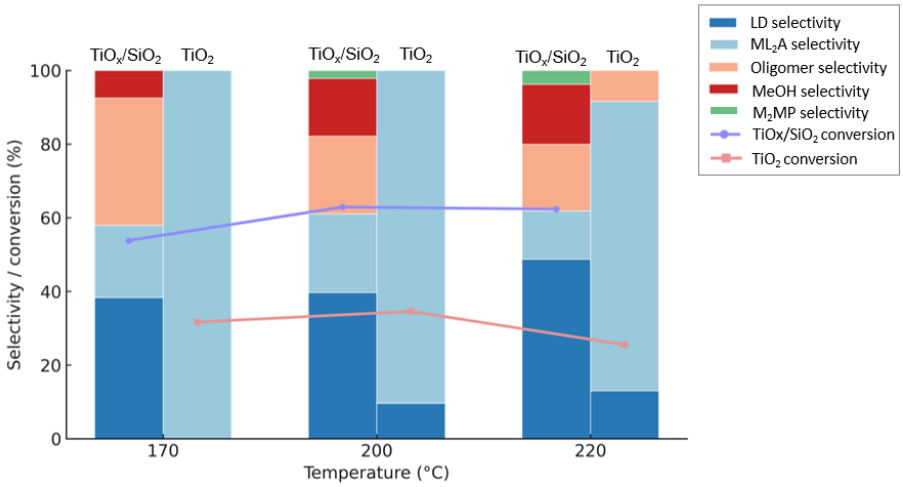


Figure 4.6 $TiO_x/SiO_2$ and $TiO_2$ catalysts performance in MLA conversed to LD reaction at different reaction temperature

## 4.2.3 Reaction pathway of MLA to LD

Guided by the results and analysis of experiments, the $Ti(III)O_x/SiO_2$ catalyst was selected for reaction pathway modelling. To meet the requirements of the pathway simulations, the surface model was enlarged and constructed with two exposed Ti centres so that configurations containing more than one Ti site could be represented.

Figure 4.7 illustrates the computational reaction coordination for the conversion of two MLA molecules to LD on Ti(III) $O_x/SiO_2$. Adsorption proceeds stepwise. First, the adsorption of 1$^{st}$ MLA on the catalyst surface is owing to Ti(III) of Ti(III) $O_x/SiO_2$ and O from carboxylic group of MLA and the hydrogen bonding interaction between MLA and silica support surface. The adsorption of 2$^{nd}$ MLA is on the same Ti(III) active point. For building the co-adsorbed reactant complex, several positions of the second MLA were evaluated: adsorption at the neighbouring Ti centre, association with the first adsorbed MLA, and co-adsorption at the same Ti centre as the first MLA. Considering both adsorption energetics and straightforward geometric feasibility for the subsequent

elementary steps, the configuration in which the two MLAs bind at the same Ti centre is preferred and is therefore adopted as the starting point for the reaction-pathway calculations. The dimerization occurs via nucleophilic C-O attack of 2nd MLA on the Ti-activated ester carbon of the 1st MLA. The associated TS1 lies only 0.63 eV above the adsorbed reactant complex and releases one methanol to give a linear configuration of $ML_2A$. The intramolecular ring closure proceeds through TS2, which requires 1.82 eV and liberates a second methanol molecule to furnish chemisorbed LD. Such a high barrier indicates that TS2 is difficult to overcome under the reaction conditions, the cyclisation step constitutes the rate-limiting step, rationalising the build-up of $ML_2A$ observed in the experiments.

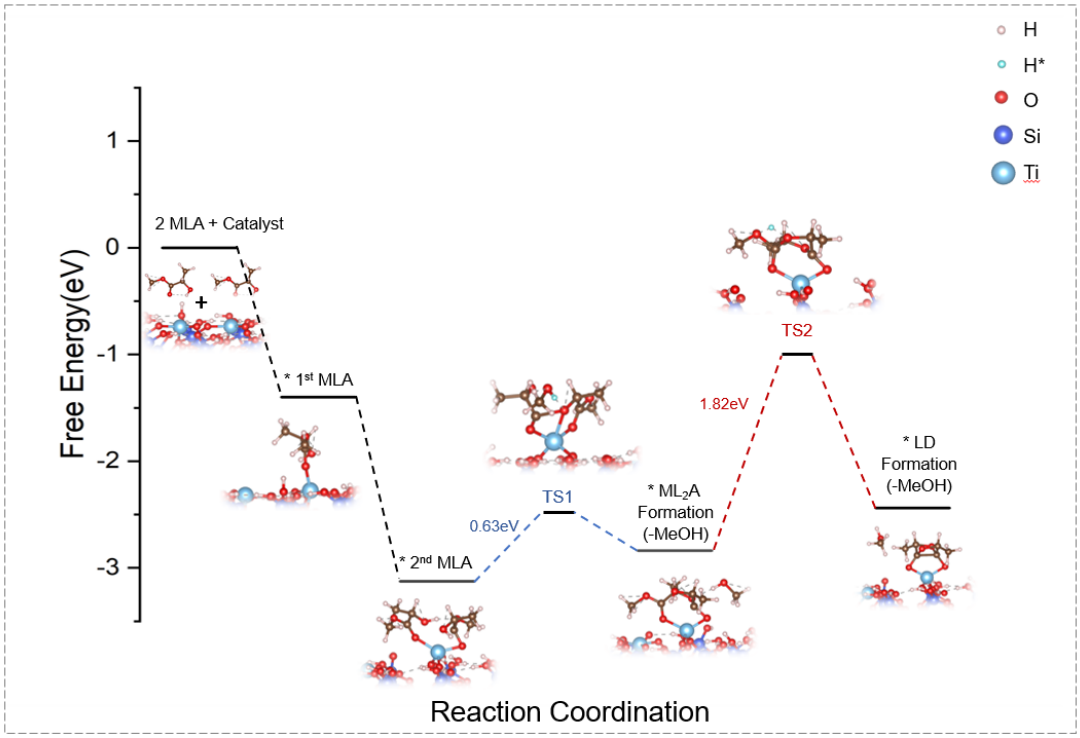


Figure 4.7 Reaction coordination from MLA to LD with Ti(III)$O_x$/SiO2 catalyst. Colour code atoms: Ti in blue, Si in navy, O in red, C in brown, H radical in light blue, H in white.

### 4.2.4 Consistency between experiment and DFT

Surface analyses establish that only $TiO_x/SiO_2$ contains a measurable fraction of Ti(III) (≈ 6 %) while bulk $TiO_2$ is entirely Ti(IV) (XPS, Figure 4.4). XRD/TEM/SEM show no crystalline Titania on $TiO_x/SiO_2$, STEM–EDS maps are featureless without Ti-rich domains, and FTIR displays a ~945 $cm^{-1}$ band characteristic of Ti–O–Si linkages (Figures 4.1–4.3, 4.5). These results indicate that titanium is present predominantly as highly dispersed $TiO_x$ species anchored to silica, i.e., isolated Ti–O–Si sites with a small population of Ti(III).

Catalytically, $TiO_x/SiO_2$ exhibits higher MLA conversion than $TiO_2$ at all temperatures, while the product distribution shows a pronounced build-up of the dimer $ML_2A$ and a delayed formation of LD (Figure 4.5). The DFT free-energy profile rationalises these trends: on an isolated Ti(III)–O–Si site, dimerization of a second MLA onto a Ti-activated first MLA proceeds via TS1 with a modest barrier (0.63 eV), releasing MeOH to form $ML_2A$; the subsequent intramolecular cyclisation to LD requires a much higher barrier (TS2, 1.82 eV) and constitutes the rate-limiting step. As a result, $ML_2A$ accumulates as the intermediate at lower temperatures, and substantial LD forms only when the temperature is high enough to overcome TS2, consistent with experiment.

## 4.3 Conclusions

The catalytic performance of $TiO_x/SiO_2$ is better than bulk $TiO_2$ across the temperature of 170–220 °C, reaching 62 % MLA conversion and 49 % LD selectivity at 220 °C, whereas $TiO_2$ never exceeds 34.6% MLA conversion and 13 % LD selectivity. The superior activity is because of Ti(III)–O–Si sites: XPS detects ~ 6 % Ti(III), STEM-EDS confirms atomic dispersion. However, two equivalents of methanol are released

along the pathway; their accumulation shifts equilibrium backwards and promotes secondary alcoholysis to $M_2MP$, particularly above 200 °C. Combined DFT results, shows the free-energy profile reveals a modest barrier for dimerization (0.63 eV) but a much higher barrier for ring closure (1.82 eV), identifying cyclisation as the rate-limiting step and rationalising the experimental $ML_2A$ build-up. Thus, high densities of Ti(III)–O–Si sites are necessary but not sufficient. The sustained LD yields will also require in-situ methanol removal (gas stripping, membranes, or sorbents). Together, these works establish a structure–reactivity blueprint for designing next generation Ti-based, single reactor systems for green LD production.

# References


(1) De Clercq, R.; Dusselier, M.; Makshina, E.; Sels, B. F. Catalytic Gas-Phase Production of Lactide from Renewable Alkyl Lactates. Angew. Chem. Int. Ed. 2018, 57 (12), 3074–3078. https://doi.org/10.1002/anie.201711446.

(2) De Clercq, R.; Dusselier, M.; Poleunis, C.; Debecker, D. P.; Giebeler, L.; Oswald, S.; Makshina, E.; Sels, B. F. Titania-Silica Catalysts for Lactide Production from Renewable Alkyl Lactates: Structure–Activity Relations. ACS Catal. 2018, 8 (9), 8130–8139. https://doi.org/10.1021/acscatal.8b02216.

(3) Holder, C. F.; Schaak, R. E. Tutorial on Powder X-Ray Diffraction for Characterizing Nanoscale Materials. ACS Nano 2019, 13 (7), 7359–7365. https://doi.org/10.1021/acsnano.9b05157.

(4) Sathasivam, S.; Bhachu, D. S.; Lu, Y.; Chadwick, N.; Althabaiti, S. A.; Alyoubi, A. O.; Basahel, S. N.; Carmalt, C. J.; Parkin, I. P. Tungsten Doped TiO2 with Enhanced Photocatalytic and Optoelectrical Properties via Aerosol Assisted Chemical Vapor Deposition. Sci. Rep. 2015, 5 (1), 10952. https://doi.org/10.1038/srep10952.

(5) De Clercq, R.; Dusselier, M.; Poleunis, C.; Debecker, D. P.; Giebeler, L.; Oswald, S.; Makshina, E.; Sels, B. F. Titania-Silica Catalysts for Lactide Production from Renewable Alkyl Lactates: Structure–Activity Relations. ACS Catal. 2018, 8 (9), 8130–8139. https://doi.org/10.1021/acscatal.8b02216.

(6) Sparkman, O. D.; Penton, Z.; Kitson, F. G. Gas Chromatography and Mass Spectrometry: A Practical Guide; Academic Press, 2011.

(7) McWILLIAM, I. G.; DEWAR, R. A. Flame Ionization Detector for Gas Chromatography. Nature 1958, 181 (4611), 760–760. https://doi.org/10.1038/181760a0.

(8) Agilent Technologies. Data Analysis Reference for OpenLab ChemStation, LTS 01.11.; manual D0013749 Rev. A.2; Agilent Technologies: Waldbronn, Germany, 2025. https://www.agilent.com/cs/library/usermanuals/public/CS-LTS_01.11_Reference_en.pdf.

(9) Zhuang, X.-W.; Feng, Y.-S.; Qiao, H.; Yu, H.-X.; Yang, W.-M.; Pan, X. Glucose Conversion Process to Methyl Lactate Catalyzed by SnCl4-Based Homogeneous Catalysis. BioResources 2024, 19 (2), 2436–2451. https://doi.org/10.15376/biores.19.2.2436-2451.

(10) Shimadzu Corporation. Analysis results of GC: Percentage peak area method. https://www.shimadzu.com/an/service-support/technical-support/analysis-basics/fundamentals/results.html (accessed 2025-09-12).

(11) Zhang, B.; Chen, Y.; Li, J.; Pippel, E.; Yang, H.; Gao, Z.; Qin, Y. High Efficiency Cu-ZnO Hydrogenation Catalyst: The Tailoring of Cu-ZnO Interface Sites by Molecular Layer Deposition. ACS Catal. 2015, 5 (9), 5567–5573. https://doi.org/10.1021/acscatal.5b01266.

(12) Kresse, G.; Furthmüller, J. Efficient Iterative Schemes for Ab Initio Total-Energy Calculations Using a Plane-Wave Basis Set. Phys. Rev. B 1996, 54 (16), 11169–11186. https://doi.org/10.1103/PhysRevB.54.11169.

(13) Kresse, G.; Furthmüller, J. Efficiency of Ab-Initio Total Energy Calculations for Metals and Semiconductors Using a Plane-Wave Basis Set. Comput. Mater. Sci. 1996, 6 (1), 15–50. https://doi.org/10.1016/0927-0256(96)00008-0.

(14) Huang, S.; Shang, C.; Kang, P.; Zhang, X.; Liu, Z. LASP: Fast Global Potential Energy Surface Exploration. WIREs Comput. Mol. Sci. 2019, 9 (6). https://doi.org/10.1002/wcms.1415.

(15) Perdew, J. P.; Burke, K.; Ernzerhof, M. Generalized Gradient Approximation Made Simple. Phys. Rev. Lett. 1996, 77 (18), 3865–3868. https://doi.org/10.1103/PhysRevLett.77.3865.

(16) Kresse, G.; Joubert, D. From Ultrasoft Pseudopotentials to the Projector Augmented-Wave Method. Phys. Rev. B 1999, 59 (3), 1758–1775. https://doi.org/10.1103/PhysRevB.59.1758.

(17) Dudarev, S. L.; Botton, G. A.; Savrasov, S. Y.; Humphreys, C. J.; Sutton, A. P. Electron-Energy-Loss Spectra and the Structural Stability of Nickel Oxide: An LSDA+U Study. Phys. Rev. B 1998, 57 (3), 1505–1509. https://doi.org/10.1103/PhysRevB.57.1505.

(18) El-Desoky, M. M.; Morad, I.; Wasfy, M. H.; Mansour, A. F. Synthesis, Structural and Electrical Properties of PVA/TiO2 Nanocomposite Films with Different TiO2 Phases Prepared by Sol–Gel Technique. J. Mater. Sci. Mater. Electron. 2020, 31 (20), 17574–17584. https://doi.org/10.1007/s10854-020-04313-7.

(19) Innocenzi, P. Infrared Spectroscopy of Sol–Gel Derived Silica-Based Films: A Spectra-Microstructure Overview. J. Non-Cryst. Solids 2003, 316 (2–3), 309–319. https://doi.org/10.1016/S0022-3093(02)01637-X.

(20) Gao, X.; Wachs, I. E. Titania–Silica as Catalysts: Molecular Structural Characteristics and Physico-Chemical Properties. Catal. Today 1999, 51 (2), 233–254. https://doi.org/10.1016/S0920-5861(99)00048-6

# Chapter 5

# Advancing Catalytic Performance: Catalyst Valence and Support

Chapter 4 has developed a transesterification process of methyl lactate (MLA) to lactide (LD) in one-step liquid phase process, Titania-silica catalyst exhibit better conversion (62%) and selectivity (49%) than $TiO_2$ catalyst. However, their significantly lower yield (30%) compares to the conventional industrial process of lactic acid (LA) to LD (LA→oligomers→LD) (85%) [3] remains a critical barrier to commercial viability. This performance gap suggests that the catalytic mechanism and the nature of the performance enhancement are not yet know. Specifically, the precise role of the silica support and the mechanistic influence of the titanium valence state (e.g., Ti(IV) vs Ti(III)) on catalytic activity remain poorly elucidated. Accordingly, in this chapter, the mechanism of catalyst action on MLA is explored at a deeper atomic level, focusing on the effects of different valence of surface Ti and with/without a silica support during the adsorption. The aim is to advance the catalyst performance.

# 5.1 Methodology

For the adsorption of MLA part, the geometry optimizations and electronic structure calculations were performed via the Vienna Ab Initio simulation package(VASP) [2,3]utilizing DFT within the generalized gradient approximation (GGA) method. Core electrons were described using the projected-augmented wave (PAW) method[4]. Perdew–Burke–Ernzerh (PBE) of parametrized GGA functionals are utilized to describe the exchange–correlation interaction. The cut-off energy of plane-wave basis sets was 400eV. The solution of the Kohn–Sham equations was iteratively refined until a convergence criterion of less than $10^{-4}$ eV was met between consecutive iterations. A Hubbard U value of 4.2 eV was used for the Ti 3d states to consider the effect of the onsite Coulomb interaction according to the previous reports[5]. Geometry was considered optimized when the energy on each atom was less than 0.001 eV/Å. For the Titania-silica catalysts, a (1 × 3 × 1) k-point grid of Monkhorst-Pack was used for optimization and energy calculation; for the $TiO_2$ and $TiO_2$-Ov (with O vacancy) catalysts, a $(2 \times 3 \times 1)$ k-point grid of Monkhorst-Pack was used. The adsorption energy ($E_{ads}$) of MLA on catalyst surface is defined by Eq(5.1), $E_{suf/gas}$ is the total energy of the MLA adsorbs on the catalyst surface, $E_{suf}$ is the energy of the catalyst surface, $E_{gas}$ is the energy of MLA molecule before adsorption.

$$E_{ads} = E_{suf/gas} - E_{suf} - E_{gas} \tag{5.1}$$

The oxygen vacancy formation energy ($E_{f(Ov)}$) is defined by Eq(5.2), $E_{tot(def)}$ is the total energy of a reduced (O-deficient) catalyst surface, $E_{tot(no\ def)}$ is the total energy of the anatase(101) surface, $\frac{1}{2}\mu O_2$ is a free O in the gas phase.

$$E_{f(Ov)} = E_{tot(def)-} E_{tot(no\ def)} + \frac{1}{2}\mu O_2 E_{gas} \quad (5.2)$$

The converged wavefunctions calculation for the Mayer bond order was computed by Gaussian 16 Package[6], the further Mayer bond order analysis was performed using the Multiwfn[7,8]. The extended basis set 6-311G(d,p) (for C, H, O, Si atoms) and LANL2DZ (for Ti atoms) basis sets were employed in this study.

# 5.2 Results and Discussion

## 5.2.1 Adsorption of MLA on catalyst systems

### *Titania-silica*

As a catalyst for the synthesis of LD by MLA liquid-phase transesterification, the surface structure of Titania-silica is diverse. The Titania-silica catalyst surface is primarily defined by a silicon foundation comprising silica-oxygen tetrahedra, to which titanium species are anchored, ranging from isolated mononuclear forms to multinuclear or aggregated structures. The particular configuration of these titanium based groups significantly influences the reactivity and selectivity of catalysts[9]. In this work, the catalyst support is based on β-cristobalite structure, commonly has employed to represent amorphous silica in literature[10]. The silica support surface is constructed by cutting the bulk to (001) planes, featuring dimensions of 17.02, 9.83 and 21.00 Å in the a-, b-, and c-directions, respectively. The oxygen atoms on the silica surface is terminated with hydrogen atoms.

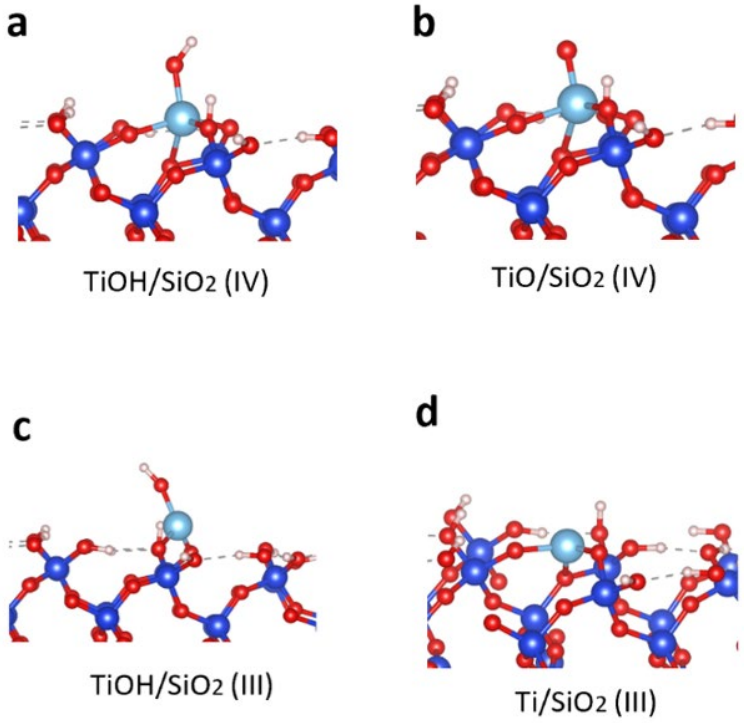


Figure 5.1 Optimized structure of different catalysts. a. TiOH/$SiO_2$(IV), TiOH supported on silica for the first position; b. TiO/$SiO_2$(IV), TiO supported on silica; c. TiOH/$SiO_2$(III), TiOH supported on silica for the second position; d. Ti/$SiO_2$(III). a, b, for Ti (IV); c, d for Ti (III). Colour code atoms: Ti in blue, Si in navy, O in red, H in white.

Within Titania-silica catalysts, the valence state of titanium is a pivotal parameter. While Ti(IV) is the dominant species, often exhibiting tetrahedral or octahedral coordination, Ti(III) can also materialize under certain conditions[11]. To investigate the influence of different valence states Ti on catalyst adsorption, four distinct Titania-silica catalyst structures are designed in this work, as depicted in Figure 5.1a to 5.1d. In Figure 5.1a and 5.1b, TiOH and TiO are loaded onto the silica surface with five Ti-O bonds, called TiOH/$SiO_2$(IV) and TiO/$SiO_2$(IV). In Figure 5.1c and 5.1d, another TiOH at different location is compared with TiOH/$SiO_2$(IV) and a Ti atom are loaded onto the

silica surface with three Ti-O bonds, called TiOH/$SiO_2$(III) and Ti/$SiO_2$(III). From the projected density of states (PDOS) in Figure 5.2, the valence of Ti in TiOH/$SiO_2$(IV) and TiO/$SiO_2$(IV) show Ti(IV) are observed, electrons occupy only a small amount below the Fermi energy level in the d-orbital of Ti; in TiOH/$SiO_2$(III) and Ti/$SiO_2$(III) cases, the apparent isolates peaks of electrons below the Fermi energy level provide support for Ti(III).

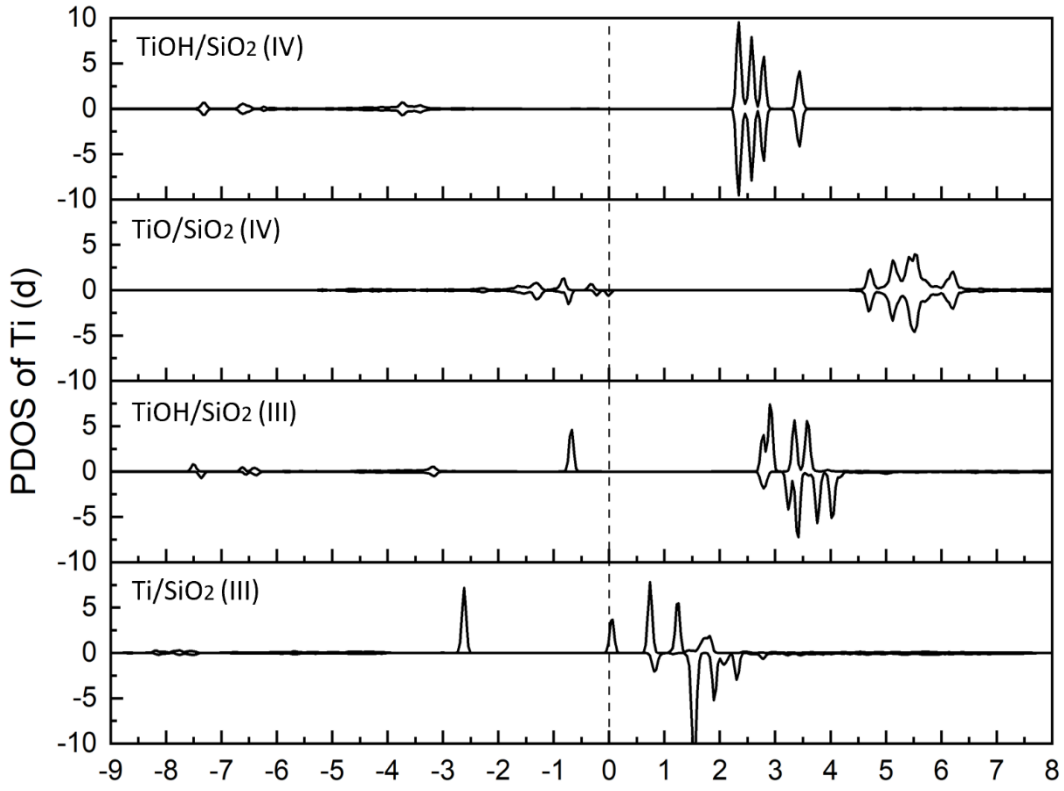


Figure 5.2 PDOS of Titania-silica catalysts

## *$TiO_2$/$TiO_2$-Ov (O vacancy)*

To evaluate the role of catalyst supports, $TiO_2$(101) surface and $TiO_2$ with O vacancy surface are considered for comparing with the performance of Titania-silica systems. It has been reported that the MLA conversion of anatase is higher than rutile in the synthesis LD from MLA by gas-phase transesterification process[12], in this work (101)

plane of anatase bulk is employed to build the $TiO_2$ surface ($TiO_2$(IV)), shows in Figure 5.3a, the crystallographic parameters are 16.33, 11.33, 22.89 Å in the a-, b-, and c-directions, respectively. Based on the perfect $TiO_2$ (101) surface, the $TiO_2$ catalyst surface with an oxygen vacancy ($TiO_2$-Ov(III)) was constructed by removing one oxygen atom, as shown in Figure 5.3b. In Figure 5.4, there are 3-fold (Ov-1) and 2-fold (Ov-2) oxygen in the upper surface of the stepped perfect $TiO_2$(101) surface, and two different 3-fold oxygen (Ov-3, Ov-4) in the subsurface. Based on the formation energies of systems with four different oxygen vacancy positions, the site of Ov-2 has the lowest formation energy with 4.91 eV, which is the most stable case. The results have the same trend as the literature reported[13].

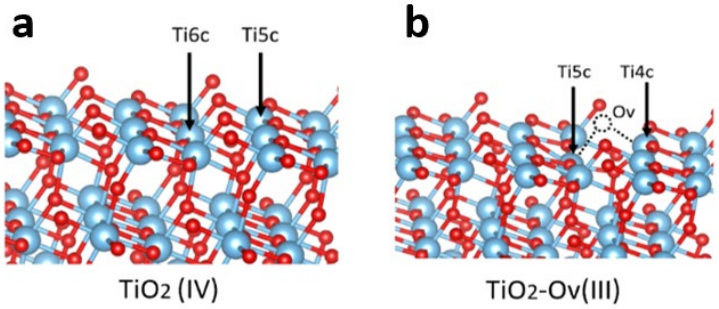


Figure 5.3 Optimized structure of different catalysts. a. $TiO_2$(IV), anatase $TiO_2$; b. $TiO_2$-Ov (III), anatase $TiO_2$ with one O vacancy. a for Ti (IV); b for Ti (III). Colour code atoms: Ti in blue, O in red.

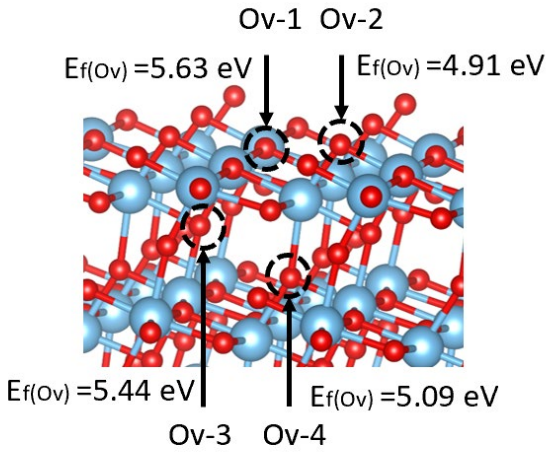


Figure 5.4 The sites of oxygen atoms removed on $TiO_2$. Colour code atoms: Ti in blue, O in red.

The density of states (DOS) of $TiO_2$(IV) surface shows in Figure 5.5a, an empty energy gap between the conduction and valence bands, which is consistent with typical $TiO_2$ features[14]. When an oxygen vacancy is constructed, a neutral oxygen atom is removed from the surface of anatase and two additional electrons occupy the Ti empty state, thus, the oxidation state of two Ti atoms are reduced from Ti(IV) to Ti(III). $TiO_2$ catalysts possess a distinct and broad band gap, with the valence band maximum (VBM) and conduction band minimum (CBM) markedly separated which is the typical of an intrinsic semiconductor. Figure 5.5b shows the DOS of $TiO_2$-Ov(III), comparing the DOS of $TiO_2$(IV), the VBM of $TiO_2$-Ov(III) catalyst is elevated, positioned at approximately -0.6 eV relative to the Fermi level, while the CBM shows a slight upward movement, indicating a reduced band gap compared to pristine $TiO_2$(IV). This reduction in band gap is indicative of new electronic states within the band structure, primarily attributed to the presence of Ti(III) ions resulting from the reduction of Ti(IV) due to the oxygen vacancy.

Moreover, a distinct isolated peak is in the energy gap, mainly contributed by 4-fold Ti, where the Ti(III) states exhibits localisation.

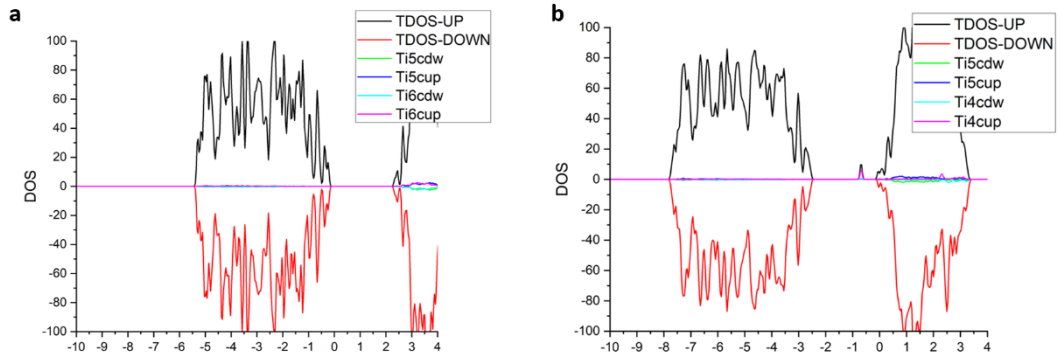


Figure 5.5 DOS of Ti-based catalysts. a. Total and projected DOS of $TiO_2$(IV). b. Total and projected DOS of $TiO_2$-Ov(III). Colour code lines: total DOS (TDOS) spin up in black, total DOS spin down in red, PDOS of Ti 5c spin down in green, PDOS of Ti 5c spin up in navy, PDOS of Ti 6c spin down in light blue, PDOS of Ti 6c spin down in light blue.

## 5.2.2 Effect of Titanium valence for the MLA adsorption

To identify the most stable structure for MLA adsorption on titanium-based catalysts, a thorough adsorption search is conducted on the Titania-silica catalyst surfaces. MLA presents three possible adsorption sites on titanium-based catalysts show in Figure 5.6, 1) oxygen atom of hydroxyl group(9O), 2) oxygen atom of ester group(1O), and 3) oxygen atom of ester group (10O). The chirality of MLA was considered in each position by rotating 90°.

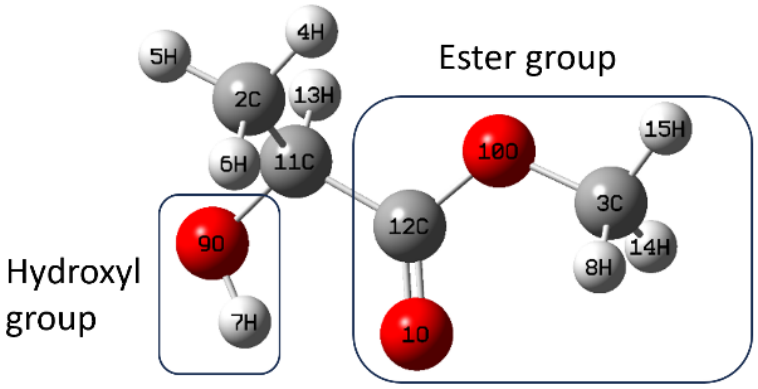


Figure 5.6 The structure of MLA. 9O and 7H are in hydroxyl group(-OH), 1O and 12C are in ester group(O=C), 10O and 12C are in ester group (O-C); Colour code atoms: O in red, C in grey, H in white.

The adsorption energy comparisons for different sites on various catalysts are illustrated in Figure 5.7. Across the four catalyst scenarios, the oxygen atom of the MLA ester group(O=C) as the adsorption site exhibited the highest adsorption energies. In $TiOH/SiO_2$(IV) and $TiO/SiO_2$(IV), where Ti(IV) is loaded onto the silica surface, the adsorption energies of the most stable structure are -0.71eV ($TiOH/SiO_2$(IV)) and -0.84eV ($TiO/SiO_2$(IV)), respectively. In $TiOH/SiO_2$(III) and $Ti/SiO_2$(III), where Ti(III) is loaded onto the silica surface, the highest adsorption energies are -1.34eV ($TiOH/SiO_2$(III)), and -1.69eV ($Ti/SiO_2$(III)). The adsorption energies indicate that the silica support loaded with Ti(III) exhibits a stronger adsorption capacity compared to the silica support loaded with Ti(IV), with the most stable configuration being MLA adsorption onto the $Ti/SiO_2$(III) catalyst.

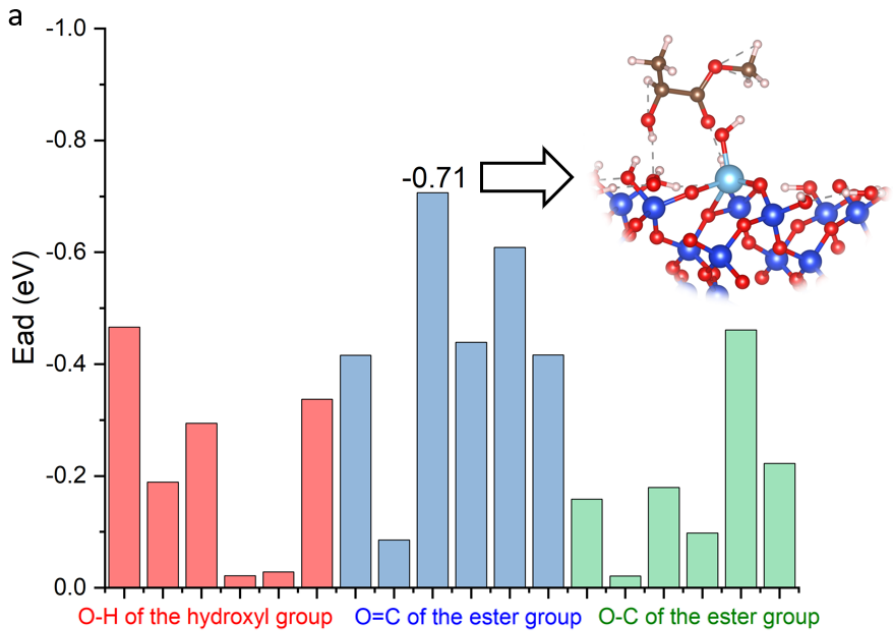


a. $TiOH/SiO_2(IV)$

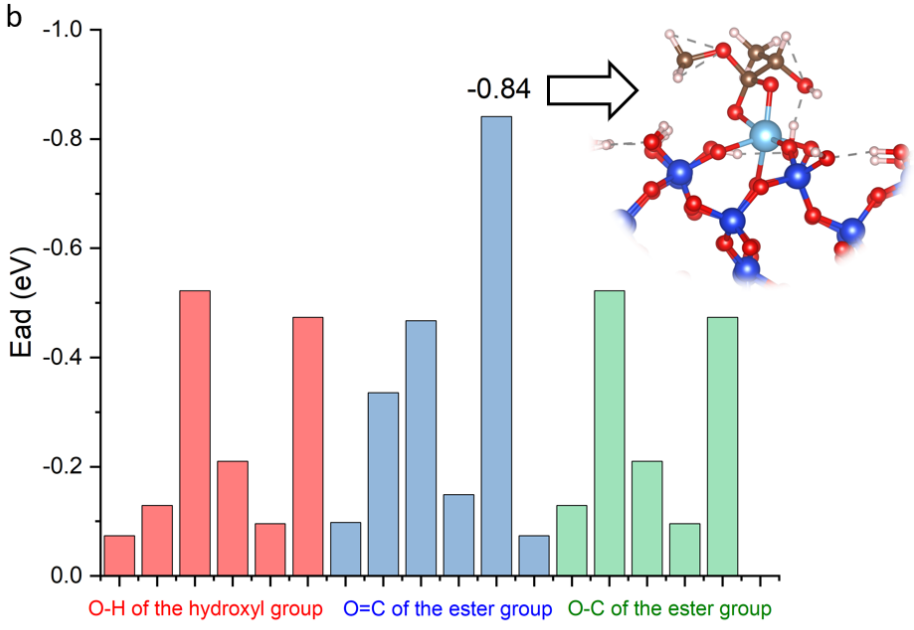


b. $TiO/SiO_2(IV)$

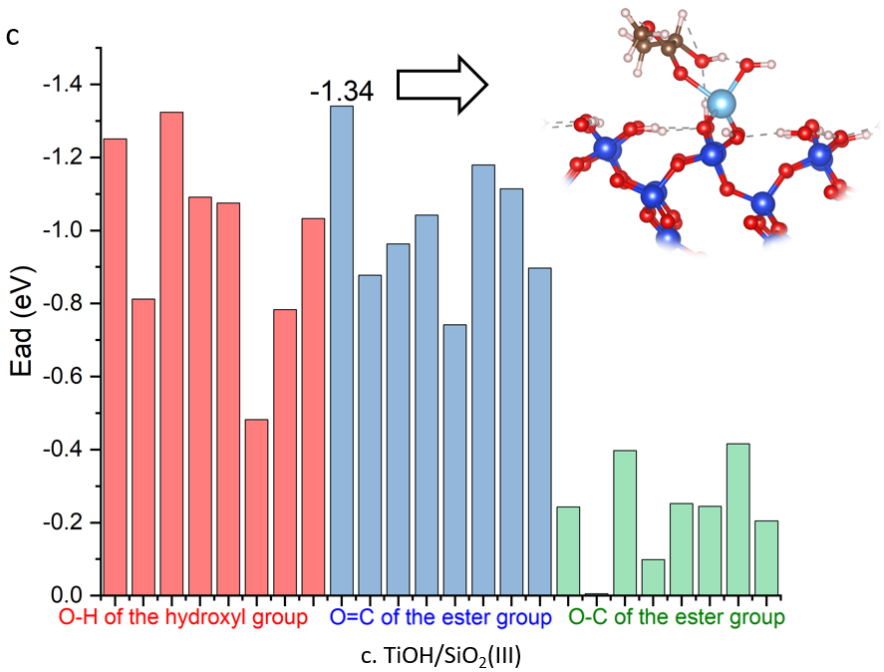


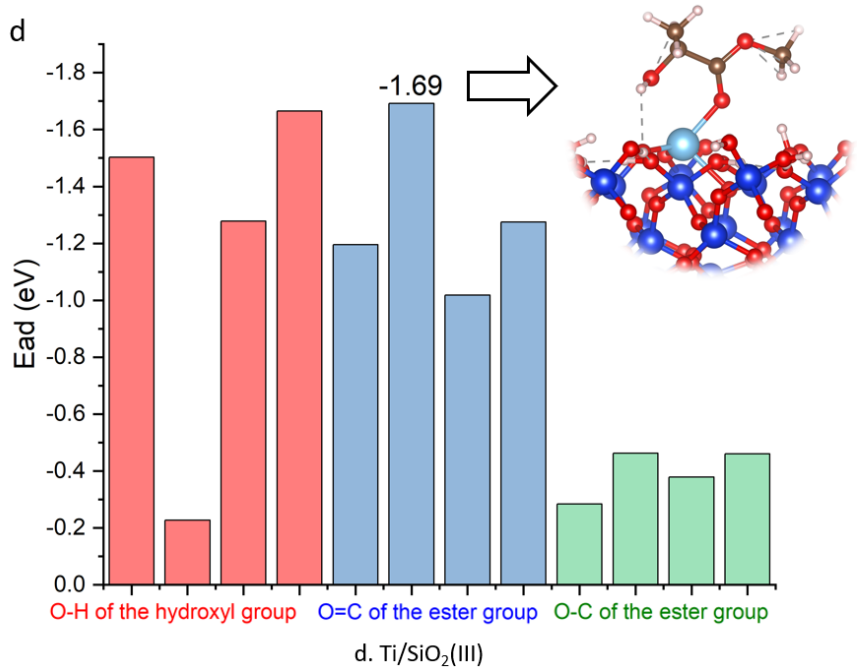


Figure 5.7 Adsorption energy and the most stable structure of MLA on four Titania-silica catalysts. a. $TiOH/SiO_2(IV)$; b. $TiO/SiO_2(IV)$; c. $TiOH/SiO_2(III)$; d. $Ti/SiO_2(III)$

The electronic structure of adsorption has been analysed within the most stable geometry of each adsorption of MLA on Titania-silica catalysts surface. Figure 5.8 shows

the Charge density difference (CDD) plots. In Figure 5.8a, the adsorption on $TiOH/SiO_2$(IV), Ti(IV) on the catalyst surface is a completely hydroxylated, covering the Ti atom and diminishing its electron affinity. Two hydrogen bonds adsorptions are perceived, one between the O of $SiO_2$ support from $TiOH/SiO_2$(IV) and the H of hydroxyl group(-OH) from MLA, the other one between the H of $SiO_2$ support from $TiOH/SiO_2$(IV) and the O of ester group(O=C) from MLA. The CDD plots in Figure 5.8a show no charge transfer between MLA and the catalyst, which illustrates the hydrogen bonding mechanism. In Figure 5.8b, adsorption case of $TiO/SiO_2$(IV), the surface of $TiO/SiO_2$(IV) has an unsaturated oxygen loaded on Ti, which forms an oxidising surface. After adsorption, MLA on the catalyst surface is with one Ti-O bond, one O-C bond, and one hydrogen bond. From the CDD plots (Figure 5.8b), around the Ti atom has no significant electron transfer, more electrons accumulated on the Ti-O bond between MLA and the catalyst surface, which contributes to a covalent bond by sharing of electrons between C and O. Hydrogen bonding has no electron transfer between MLA and catalyst. The adsorption is achieved by a combination of orbital and hydrogen bonding interactions. In Figure 5.8c, adsorption on $TiOH/SiO_2$(III), the activity of Ti is altered by the hydroxylated surface, one Ti-O bond and two hydrogen bonds are observed. The CDD results in Figure 5.8c reveal significant electron transfer between MLA and the Ti atom, driving the adsorption process. In Figure 5.8d ($Ti/SiO_2$(III)), the Ti atom is exposed to the catalyst surface, the adsorption structure displays one Ti-O bond and one hydrogen bond between MLA and $Ti/SiO_2$(III)catalyst. The CDD plot in Figure 5.8d reveals pronounced gain and loss of charge above the Ti atom. Combined with the results of adsorption energy, it is for Titania-silica catalysts, the adsorption energy of Ti(III) is stronger than that of Ti(IV), where Ti exposes on the surface of the catalyst is more likely

to form Ti-O bonds, thereby enhancing the overall adsorption effect. The CDD of all four Titanium-silica catalysts is concentrated on Ti or on surface hydrogen, with no significant change in the charge density of the $SiO_2$ support.

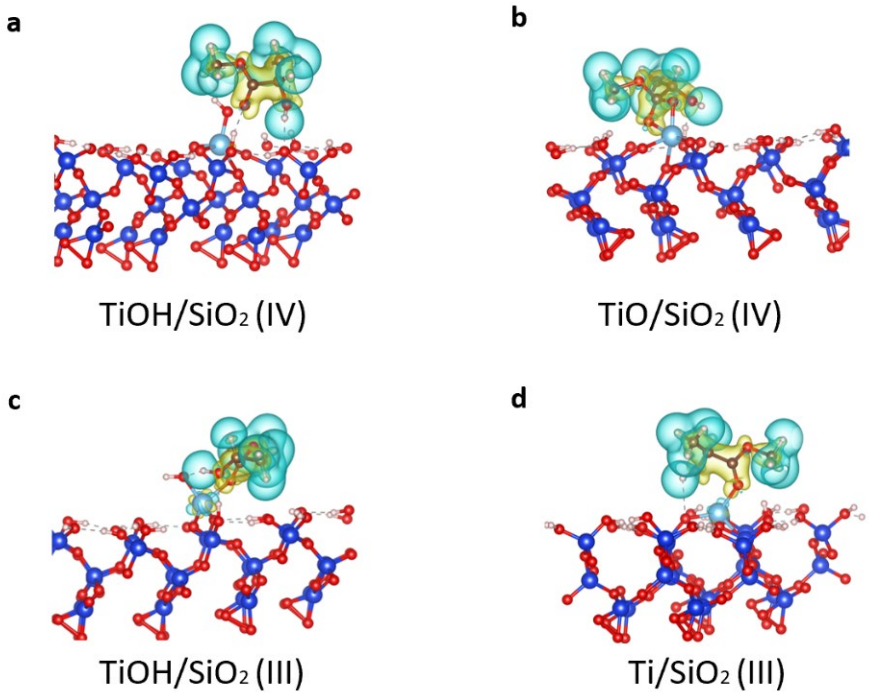


Figure 5.8 The CDD plots of MLA adsorption on Titania-silica catalysts surface. a. on $TiOH/SiO_2$(IV); b. on $TiO/SiO_2$(IV); c. on $TiOH/SiO_2$(III); d. on $Ti/SiO_2$(III). Charge depletion and accumulation are illustrated by blue and yellow, respectively. Grey dotted line shows the hydrogen bond. Colour code atoms: Ti in blue, Si in navy, O in red, C in brown, H in white.

The best performed catalyst ($Ti/SiO_2$(III)) is further validated by Bader charge analysis, as shown in Table 5.1 and DOS calculation, as shown in Figure 5.9. From the Bader charge of Ti/O/H, it is found that in the case of $TiOH/SiO_2$(IV), there is no significant charge change on the TiOH loaded before and after adsorption, which is due to the geometrical position of Ti that does not act as an active site for adsorption. In

$TiO/SiO_2$(IV), both Ti and O of TiO loaded have large charge variations, -0.1 and 0.13, respectively. Combined with the differential charge density results, the charge transfer between the catalyst and the MLA occurs mainly at the C-O bond. In $TiOH/SiO_2$(III) and $Ti/SiO_2$(III), Ti of $Ti/SiO_2$(III) transfers more charge after adsorption (-0.19), which is also consistent with the conclusion that the adsorption energy of Ti/SiO2(III) is stronger.

Table 5.1 Bader charge of Ti, O, and H atoms in different catalysts

| Items | $TiOH/SiO_2$(IV) | | | $TiO/SiO_2$(IV) | | $TiOH/SiO_2$(III) | | | $Ti/SiO_2$ (III) |
|---|---|---|---|---|---|---|---|---|---|
| Loaded on silica | Ti | O | H | Ti | O | Ti | O | H | Ti |
| Clean surface | -2.34 | 1.15 | -0.64 | -2.23 | 0.84 | -1.98 | 1.29 | -0.68 | -1.86 |
| After MLA adsorption | -2.34 | 1.16 | -0.65 | -2.33 | 0.97 | -2.04 | 1.28 | -0.64 | -2.05 |

To understand the adsorption mechanism of MLA on the $Ti/SiO_2$(III) catalyst surface under optimal adsorption conditions, a DOS calculation was performed, as shown in Figure 5.9. Two new features, labelled "A" and "B," emerged following the adsorption of MLA, indicating significant orbital interactions between the catalyst and MLA. The overlap between the Ti d orbital of the catalyst and the O p orbital of MLA suggests strong hybridisation. Feature A corresponds to σ-bonding, where the Lewis acid property of Ti(III) facilitates electron donation from the O of MLA. Feature B corresponds to π-backbonding, where electrons from the Ti d orbital are donated to the π* orbitals of O. These findings, corroborated by CDD and Bader charge analyses, demonstrate that Ti(III) atoms exhibit dual functionality, acting both as electron acceptors and electron donors during adsorption.

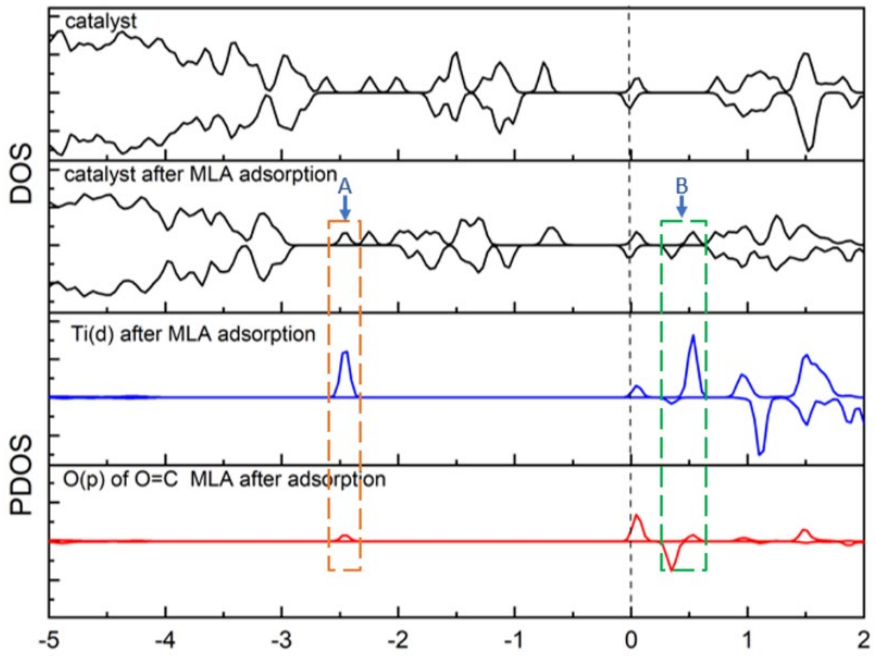


Figure 5.9 DOS of the adsorption of MLA on Ti/$SiO_2$(III) catalyst

Colour code lines: TDOS is in black. PDOS of Ti d orbital is in blue, PDOS of O p orbital is in red.

## 5.2.3 Effect of silica support for the MLA adsorption

To investigate the effect of the catalyst support on adsorption, $TiO_2$(IV) surface and $TiO_2$-Ov(III) surface are constructed to simulate Ti(IV) and Ti(III) in the absence of support. Figure 5.10 shows the adsorption energies on TiO2(IV) and TiO2-Ov(III), with the highest adsorption energy observed at the oxygen atom of the MLA ester group (O=C), at -0.67 and -0.77 eV, respectively. The most stable CDD plot cases are shown in Figure 5.10.

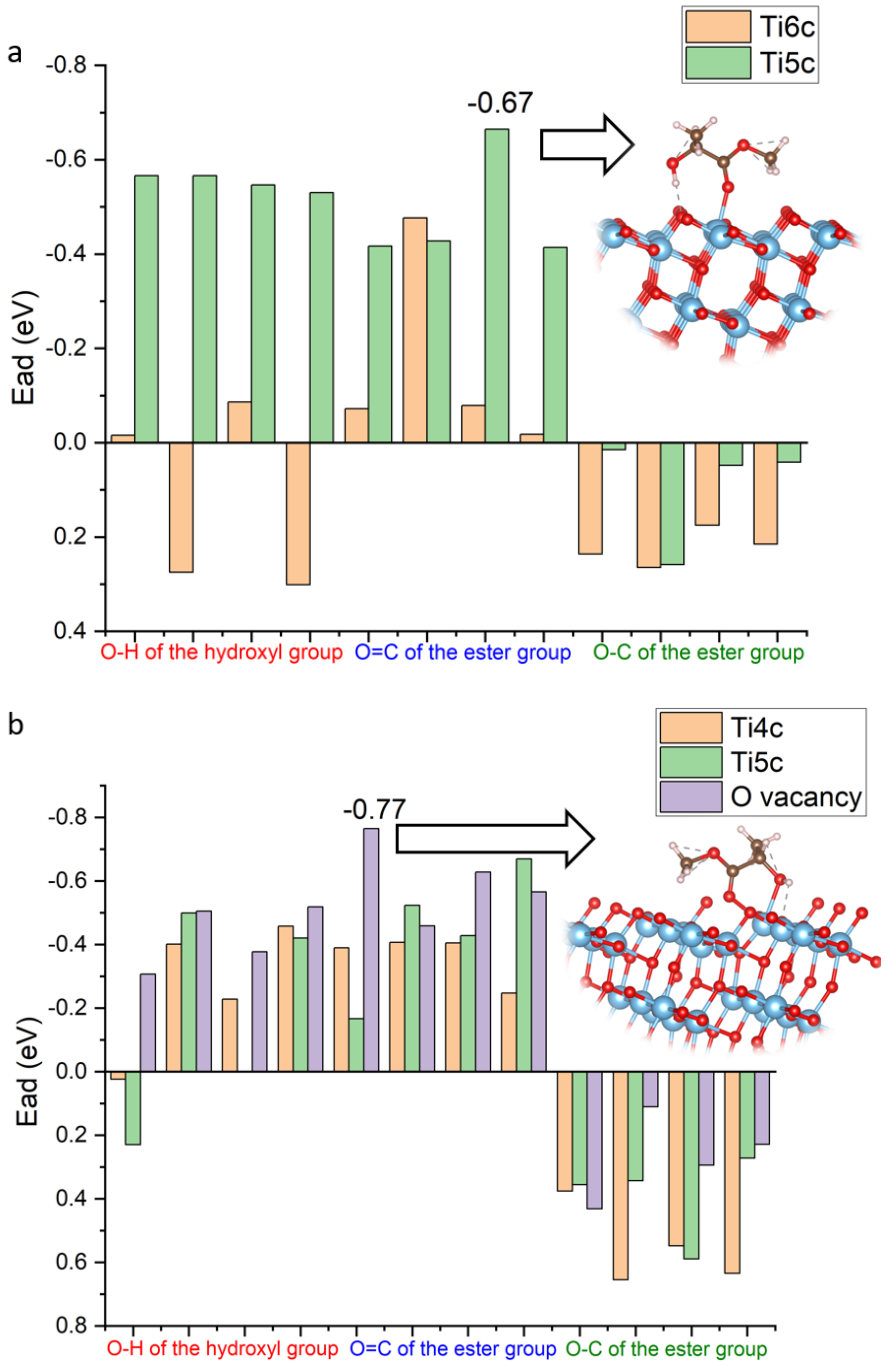


Figure 5.10 Adsorption energy and the most stable structure of MLA on a. $TiO_2$(IV) and b. $TiO_2$-Ov (III)

In $TiO_2$(IV) (Figure 5.11a), the most stable adsorption is located on Ti5c (Ti(IV)), with one Ti-O and one hydrogen bond. From the charge density difference plot, a large charge exchange between MLA and the top surface and the subsurface is observed, Ti5c both accepts and donates electrons, and the surface and deeper layers of the $TiO_2$ accept

electrons. In $TiO_2$-Ov(III) (Figure 5.11b), the oxygen atom of the MLA ester group(O=C) and the oxygen atom of the ester group (O-C) are bonded to Ti4c. Another hydrogen bond is observed. The CDD results show that only the top layer of catalyst has charge transfer with MLA, Ti not only depletes electrons, but also gains electrons from MLA mostly. Combining the Bader charge results (Table 5.2), Ti in $TiO_2$-Ov(III) undergoes a greater charge change (-0.12) after adsorption is observed than Ti in $TiO_2$(IV) (-0.09). Ti(III) exhibits a stronger charge transfer capacity in adsorption on $TiO_2$(IV) and $TiO_2$-Ov(III).

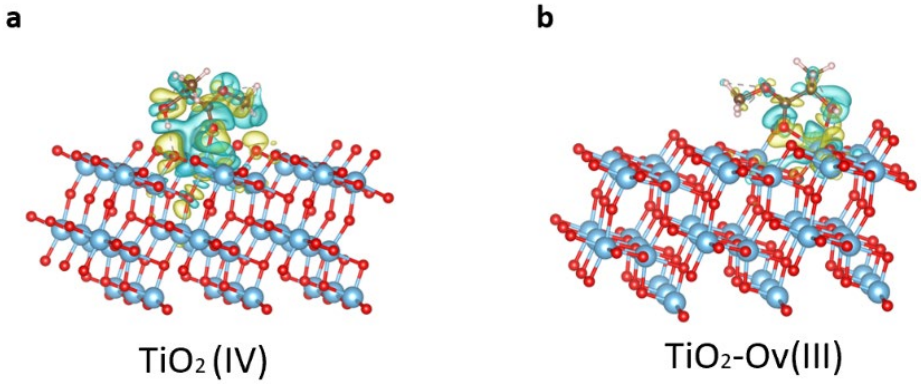


Figure 5.11 The CDD plots of MLA adsorption on a. $TiO_2$(IV) and b. $TiO_2$-Ov (III). Charge depletion and accumulation are illustrated by blue and yellow, respectively. Black dotted line shows the hydrogen bond between MLA and catalyst surface; grey dotted line shows the hydrogen bond. Colour code atoms: Ti in blue, O in red, C in brown, H in white.

Table 5.2 Bader charge of $TiO_2$(IV) and $TiO_2$-Ov(III)

| Items | $TiO_2$(IV) | | $TiO_2$-Ov(III) | |
|---|---|---|---|---|
| Ti position | Ti5c | Ti6c | Ti4c | Ti5c |
| Clean surface | -2.29 | -2.33 | -1.97 | -2.27 |
| After MLA adsorption | -2.38 | -2.32 | -2.09 | -2.28 |

## 5.2.4 Comparison of MLA adsorption on $TiO_2$(IV)/$TiO_2$-Ov(III)and Ti/$SiO_2$(III) catalysts

In this adsorption work, the adsorption of MLA on titanium-based catalysts is investigated to explore the adsorption mechanism of Ti as an active site. Three catalyst/support structures are selected based on adsorption energy, and the schematic illustrations of their proposed mechanisms are shown in Figure 5.12. The electron configurations of titanium ions are Ti(III): $(Ar)3d^1$ and Ti(IV): $(Ar)3d^0$, respectively, which result in different bonding interactions between the ester oxygen (O=C) of MLA and Ti. As shown in Figure 5.12a, the O of the O=C group of MLA has lone pairs of electrons, which are shared with Ti, forming σ-bonding. In the case of Ti(III), the partially occupied d orbital further donates electrons to the π* orbital of the oxygen, forming a d-p π-backbonding interaction. In contrast, Ti(IV) has an empty d-orbital, limiting the interaction to σ-bonding only (Figure 5.12b). These electronic differences between Ti(III) and Ti(IV) significantly influence the adsorption strength and bonding mechanism.

To investigate the effect of different valence states of titanium and the influence of catalyst supports on adsorption, $Ti/SiO_2$(III) (Figure 5.12c) from Titanium-silica catalysts is selected, which exhibits the highest adsorption energy and directly utilises titanium as the active site. For comparison, $TiO_2$(IV) and $TiO_2$-Ov(III) catalysts, shows in Figures 5.12d and 5.12e, are also selected to evaluate the impact of both titanium valence state and support structure on the adsorption mechanism. For MLA adsorption on $Ti/SiO_2$(III), both σ-bonding and π-backbonding contribute to the interaction between the Ti(III) site and O. This synergistic effect is evidenced by the appearance of new peaks on both sides of the Fermi level in the DOS analysis. Additionally, the elongation of the C=O bond length (Table 5.3) and the decrease in bond order (Table 5.4) suggest that the π-backbonding weakens the internal C=O π-bonding while enhancing the overall adsorption strength of MLA on the Ti(III) site. Furthermore, the $SiO_2$ support plays a

crucial role by anchoring the Ti(III) site through strong Si-O-Ti bonds, which stabilize the active site and prevent excessive electron transfer to the support. This anchoring effect helps maintain the electronic properties of Ti(III), further strengthening the interaction between MLA and the catalyst surface.

For MLA adsorption on $TiO_2$-Ov, although Ti(III) has the potential to form π-backbonding, DOS analysis (Figure 5.13b) shows only orbital overlap without the generation of new peaks near the Fermi level, indicating a weaker π-backbonding effect. CDD analysis further reveals that Ti transfers electrons to the surface atoms of the catalyst, thereby diminishing the adsorption strength and the possibility of forming π-backbonding. On the $TiO_2$ surface, where Ti exists primarily as Ti(IV), adsorption is dominated solely by σ-bonding, DOS shows no π-backbonding formed in Figure 5.13a. Compared to the synergistic effect of σ-bonding and π-backbonding of Ti/$SiO_2$(III) case, the adsorption strength is significantly weaker. Charge density difference analysis revealed that Ti(IV) not only transfers electrons to the surface but also to deeper layers within the $TiO_2$ lattice, further reducing the adsorption strength.

These findings demonstrate that the synergistic effect of σ-bonding and π-backbonding of Ti(III), supported by the anchoring role of $SiO_2$, makes Ti/$SiO_2$(III) the most effective catalyst for MLA adsorption. In contrast, the limited or absent π-backbonding in $TiO_2$-Ov and $TiO_2$ significantly weakens their adsorption capacity, underscoring the critical role of both titanium valence state and support structure in optimizing adsorption performance.

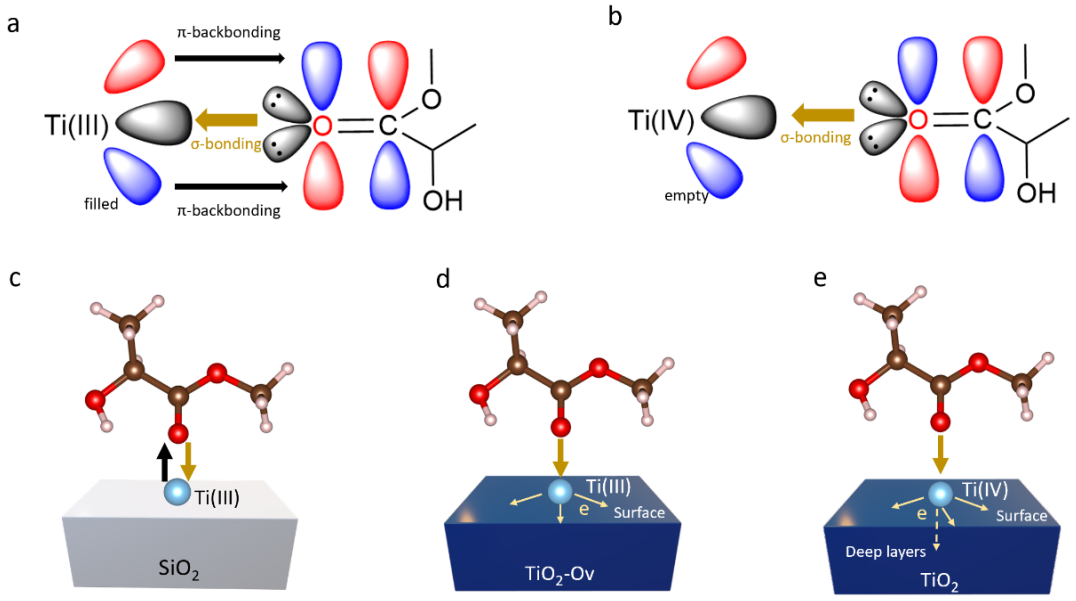


Figure 5.12 Schematic illustration of adsorption mechanisms between catalysts and MLA

Table 5.3 Bond length of MLA before and after adsorption on different catalysts (Å)

| | Isolated MLA | $TiOH/SiO_2$ (IV) | $TiO/SiO_2$ (IV) | $TiOH/SiO_2$ (III) | $Ti/SiO_2$ (III) | $TiO_2$ (IV) | $TiO_2$-Ov (III) |
|---|---|---|---|---|---|---|---|
| 1O-12C | 1.23 | 1.23 | 1.34 | 1.25 | 1.26 | 1.24 | 1.24 |
| 12C-10O | 1.35 | 1.34 | 1.41 | 1.32 | 1.32 | 1.33 | 1.32 |
| 10O-3C | 1.45 | 1.46 | 1.43 | 1.46 | 1.45 | 1.46 | 1.46 |
| 3C-14H | 1.10 | 1.10 | 1.10 | 1.10 | 1.10 | 1.10 | 1.10 |
| 3C-8H | 1.10 | 1.10 | 1.10 | 1.10 | 1.10 | 1.10 | 1.09 |
| 3C-15H | 1.10 | 1.09 | 1.10 | 1.09 | 1.09 | 1.09 | 1.10 |
| 11C-12C | 1.53 | 1.53 | 1.64 | 1.52 | 1.52 | 1.52 | 1.52 |
| 11C-9O | 1.42 | 1.42 | 1.41 | 1.43 | 1.43 | 1.40 | 1.43 |
| 9O-7H | 0.98 | 0.98 | 0.99 | 1.00 | 0.98 | 1.00 | 0.98 |
| 11C-13H | 1.11 | 1.11 | 1.11 | 1.11 | 1.11 | 1.10 | 1.10 |
| 11C-2C | 1.53 | 1.52 | 1.51 | 1.53 | 1.53 | 1.54 | 1.53 |
| 2C-4H | 1.10 | 1.10 | 1.10 | 1.10 | 1.10 | 1.10 | 1.10 |
| 2C-6H | 1.10 | 1.10 | 1.10 | 1.10 | 1.10 | 1.10 | 1.10 |
| 2C-5H | 1.10 | 1.10 | 1.10 | 1.10 | 1.10 | 1.10 | 1.10 |

* Serial number corresponds to Figure 5.6

Table 5.4 Bond order of MLA before and after adsorption on different catalysts

| | Isolated MLA | $TiOH/SiO_2$ (IV) | $TiO/SiO_2$ (IV) | $TiOH/SiO_2$ (III) | $Ti/SiO_2$ (III) | $TiO_2$ (IV) | $TiO_2$-Ov (III) |
|---|---|---|---|---|---|---|---|
| 1O-12C | 1.91 | 1.77 | 1.13 | 1.55 | 1.44 | 1.68 | 1.60 |
| 12C-10O | 0.96 | 0.96 | 0.96 | 0.96 | 0.96 | 0.95 | 0.96 |
| 10O-3C | 0.97 | 0.97 | 0.96 | 0.97 | 0.96 | 0.96 | 0.96 |
| 3C-14H | 0.97 | 0.96 | 0.96 | 0.96 | 0.96 | 0.96 | 0.95 |
| 3C-8H | 0.96 | 1.00 | 1.00 | 0.99 | 1.00 | 0.97 | 0.99 |
| 3C-15H | 0.96 | 0.96 | 0.95 | 0.94 | 0.95 | 0.94 | 0.93 |
| 11C-12C | 0.89 | 0.88 | 0.92 | 0.85 | 0.89 | 0.85 | 0.82 |
| 11C-9O | 0.97 | 0.96 | 0.94 | 0.96 | 0.95 | 0.95 | 0.96 |
| 9O-7H | 0.97 | 0.97 | 0.97 | 0.97 | 0.97 | 0.97 | 0.97 |
| 11C-13H | 0.92 | 0.86 | 0.88 | 0.84 | 0.89 | 0.82 | 0.87 |
| 11C-2C | 1.03 | 1.03 | 0.96 | 0.99 | 0.98 | 1.07 | 0.91 |
| 2C-4H | 1.15 | 1.18 | 0.97 | 1.25 | 1.12 | 1.22 | 1.27 |
| 2C-6H | 0.96 | 0.94 | 0.79 | 0.94 | 0.96 | 0.94 | 0.96 |
| 2C-5H | 0.93 | 0.92 | 0.92 | 0.93 | 0.92 | 0.94 | 0.94 |

*Serial number corresponds to Figure 5.6

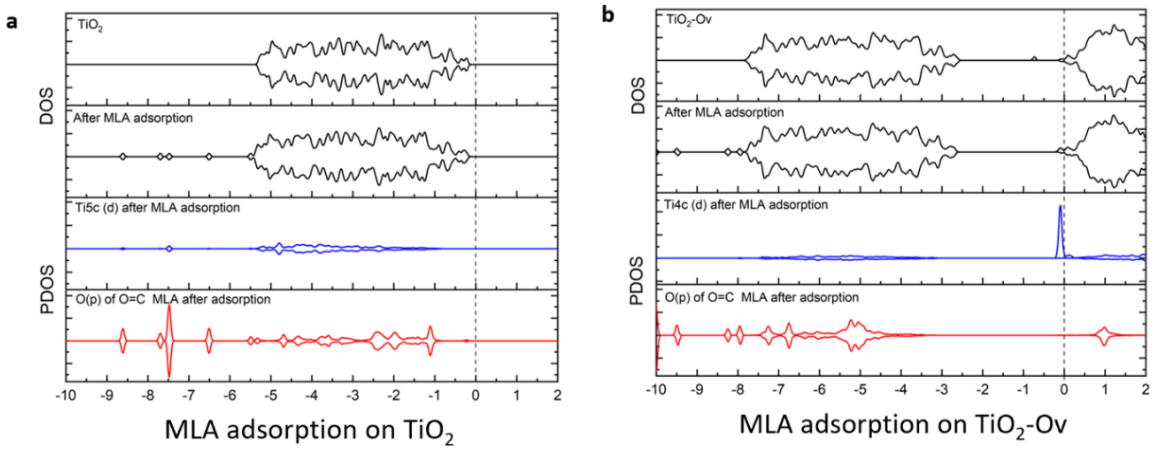


Figure 5.13 DOS of the adsorption of MLA on a. $TiO_2$(IV) and b. $TiO_2$-Ov (III)

Colour code lines: TDOS is in black. PDOS of Ti d orbital is in blue, PDOS of O p orbital is in red.

From this adsorption research, $Ti/SiO_2$(III) catalysts are designed and optimized for the adsorption of MLA, which enhances adsorption strength of catalysts to the MLA by the synergistic effect of σ-bonding and π-backbonding, thereby intensifying the adsorption interactions. This investigation elucidates the underlying adsorption mechanisms, supporting the experimental findings related to MLA conversion to LD and

advancing the feasibility of realizing a circular economy for polylactic acid. Additionally, the design principles that apply to these metal catalysts hold promise for broader applications, including the adsorption of various carbon oxides, underscoring their potential utility in addressing environmental challenges.

## 5.3 Conclusions

In this chapter, the influence of catalyst valence states and the silica support on catalytic performance is demonstrated using DFT calculations. For the adsorption behaviour, the key effects of the valence of Titanium and the catalyst support. The Ti(IV) catalysts are constructed by $TiOH/SiO_2$(IV), $TiO/SiO_2$(IV), and $TiO_2$(IV); the Ti(III) catalysts are represented by $TiOH/SiO_2$(III), $Ti/SiO_2$(III), and $TiO_2$-Ov(III). In the Titania-Silica catalysts, Ti(III) has a better adsorption capacity than Ti(IV). The highest adsorption energy is $Ti/SiO_2$(III) catalyst with -1.69eV. By CDD analysis, it is found that $SiO_2$ as a support reduces the electron loss of Ti to the deeper layers of the support. Combining the density of states result of the adsorption on $Ti/SiO_2$(III), the adsorption mechanism is a mixture of hydrogen bonding and Ti-O σ-bonding and π-backbonding synergistic effect. $TiO_2$/$TiO_2$-Ov catalysts have a lower adsorption energy than that of the Titania-silica catalysts, the adsorption energy is less than -0.77eV, even the $TiO_2$-Ov(III) with a Ti(III) active point. By the CDD plots analysis, it is found that the charge transfer is not only in the top catalyst surface but also in the subsurface specifically in $TiO_2$(IV) case, which weakens adsorption strength. Comparative analysis of bonding mechanisms reveals that the stronger σ-bonding and π-backbonding synergistic effect on $Ti/SiO_2$(III) is the key factor contributing to its higher adsorption energy. Combined with the

experimental results, a closed-loop PLA recycling cycle (Waste PLA - MLA- LD-New PLA) can be formed, which has the opportunity to acheive the PLA circular economy.

# References


(1) Dusselier, M.; Van Wouwe, P.; Dewaele, A.; Jacobs, P. A.; Sels, B. F. Shape-Selective Zeolite Catalysis for Bioplastics Production. Science 2015, 349 (6243), 78–80. https://doi.org/10.1126/science.aaa7169.

(2) Kresse, G.; Furthmüller, J. Efficient Iterative Schemes for Ab Initio Total-Energy Calculations Using a Plane-Wave Basis Set. Phys. Rev. B 1996, 54 (16), 11169–11186. https://doi.org/10.1103/PhysRevB.54.11169.

(3) Kresse, G.; Furthmüller, J. Efficiency of Ab-Initio Total Energy Calculations for Metals and Semiconductors Using a Plane-Wave Basis Set. Comput. Mater. Sci. 1996, 6 (1), 15–50. https://doi.org/10.1016/0927-0256(96)00008-0.

(4) Dudarev, S. L.; Botton, G. A.; Savrasov, S. Y.; Humphreys, C. J.; Sutton, A. P. Electron-Energy-Loss Spectra and the Structural Stability of Nickel Oxide: An LSDA+U Study. Phys. Rev. B 1998, 57 (3), 1505–1509. https://doi.org/10.1103/PhysRevB.57.1505.

(5) Zhang, J.; Peng, C.; Wang, H.; Hu, P. Identifying the Role of Photogenerated Holes in Photocatalytic Methanol Dissociation on Rutile TiO2 (110). ACS Catal. 2017, 7 (4), 2374–2380. https://doi.org/10.1021/acscatal.6b03348.

(6) Frisch, M. J.; Trucks, G. W.; Schlegel, H. B.; Scuseria, G. E.; Robb, M. A.; Cheeseman, J. R.; Scalmani, G.; Barone, V.; Petersson, G. A.; Nakatsuji, H.; Li, X.; Caricato, M.; Marenich, A. V.; Bloino, J.; Janesko, B. G.; Gomperts, R.; Mennucci, B.; Hratchian, H. P.; Ortiz, J. V.; Izmaylov, A. F.; Sonnenberg, J. L.; Williams-Young, D.; Ding, F.; Lipparini, F.; Egidi, F.; Goings, J.; Peng, B.; Petrone, A.; Henderson, T.; Ranasinghe, D.; Zakrzewski, V. G.; Gao, J.; Rega, N.; Zheng, G.; Liang, W.; Hada, M.; Ehara, M.; Toyota, K.; Fukuda, R.; Hasegawa, J.; Ishida, M.; Nakajima, T.; Honda, Y.; Kitao, O.; Nakai, H.; Vreven, T.; Throssell, K.; Montgomery, J. A., Jr.; Peralta, J. E.; Ogliaro, F.; Bearpark, M. J.; Heyd, J. J.; Brothers, E. N.; Kudin, K. N.; Staroverov, V. N.; Keith, T. A.; Kobayashi, R.; Normand, J.; Raghavachari, K.; Rendell, A. P.; Burant, J. C.; Iyengar, S. S.; Tomasi, J.; Cossi, M.; Millam, J. M.; Klene, M.; Adamo, C.; Cammi, R.; Ochterski, J. W.; Martin, R. L.; Morokuma, K.; Farkas, O.; Foresman, J. B.; Fox, D. J. Gaussian˜16 Revision C.01, 2016.

(7) Lu, T.; Chen, F. Multiwfn: A Multifunctional Wavefunction Analyzer. J. Comput. Chem. 2012, 33 (5), 580–592. https://doi.org/10.1002/jcc.22885.

(8) Lu, T. A Comprehensive Electron Wavefunction Analysis Toolbox for Chemists, Multiwfn. J. Chem. Phys. 2024, 161 (8). https://doi.org/10.1063/5.0216272.

(9) Chen, X.; Liu, L.; Liu, Z.; Marcus, M. A.; Wang, W.-C.; Oyler, N. A.; Grass, M. E.; Mao, B.; Glans, P.-A.; Yu, P. Y.; Guo, J.; Mao, S. S. Properties of Disorder-Engineered Black Titanium Dioxide Nanoparticles through Hydrogenation. Sci. Rep. 2013, 3 (1), 1510. https://doi.org/10.1038/srep01510.

(10) Handzlik, J.; Grybos, R.; Tielens, F. Structure of Monomeric Chromium(VI) Oxide Species Supported on Silica: Periodic and Cluster DFT Studies. J. Phys. Chem. C 2013, 117 (16), 8138–8149. https://doi.org/10.1021/jp3103035.

(11) Iwaszuk, A.; Nolan, M.; Jin, Q.; Fujishima, M.; Tada, H. Origin of the Visible-Light Response of Nickel(II) Oxide Cluster Surface Modified Titanium(IV) Dioxide. J. Phys. Chem. C 2013, 117 (6), 2709–2718. https://doi.org/10.1021/jp306793r.

(12) De Clercq, R.; Dusselier, M.; Poleunis, C.; Debecker, D. P.; Giebeler, L.; Oswald, S.; Makshina, E.; Sels, B. F. Titania-Silica Catalysts for Lactide Production from Renewable Alkyl Lactates: Structure–Activity Relations. ACS Catal. 2018, 8 (9), 8130–8139. https://doi.org/10.1021/acscatal.8b02216.

(13) Zheng, M.; Yang, J.; Fan, W.; Zhao, X. Oxygen Vacancy and Nitrogen Doping Collaboratively Boost Performance and Stability of TiO2 -Supported Pd Catalysts for CO2 Photoreduction: A DFT Study. Phys. Chem. Chem. Phys. 2021, 23 (43), 24801–24813. https://doi.org/10.1039/D1CP03693A.

(14) Portillo-Vélez, N. S.; Olvera-Neria, O.; Hernández-Pérez, I.; Rubio-Ponce, A. Localized Electronic States Induced by Oxygen Vacancies on Anatase TiO2 (101) Surface. Surf. Sci. 2013, 616, 115–119. https://doi.org/10.1016/j.susc.2013.06.006.

# Chapter 6
# Techno-Economic Analysis of a Closed-loop Circular Economy for PLA

The preceding chapters of this thesis have established a PLA circular economy route as shown in Section 5.2.5. To translate these insights into an assessment of industrial-scale viability, a complete process flowsheet with detailed mass and energy balances is required. In this chapter, the full process schemes with different recycling method for a polylactic acid (PLA) circular economy are developed; second, the potential economic impact of catalyst improvements to the MLA to LD process proposed in this thesis is discussed and evaluated.

The content of this chapter has been published in a journal (ACS Sustainable Chemistry & Engineering)[1].

# 6.1 Methodology

## 6.1.1 End-of-life PLA Feedstock Preparation

Effective chemical recycling of post-consumer waste PLA (WPLA) first requires a pretreatment stage to reduce pollution from additives and other materials commonly found in waste streams[1,2]. Although additives are typically present in small quantities and do not chemically bond with the polymer, their removal is essential for producing a high purity feedstock[3,4]. For the WPLA, it is assumed to begin with collection and transport to a materials recovery facility. The PLA fraction is isolated from mixed plastics by near-infrared (NIR) spectroscopy based sorting[1]; the sorted material is then washed in 2% (w/v) aqueous NaOH at 70 °C to remove surface residues, reducing total impurities to below 5%; finally, the purified WPLA is dried and shredded to yield feedstock suitable for subsequent chemical conversion.

## 6.1.2 Processing routes for PLA recycling

To evaluate different recycling strategies, three primary process routes for converting WPLA into new polymer were simulated (Figure 6.1). Process 1 (conventional hydrolysis route) represents the common industrial method. It involves the hydrolysis of WPLA to produce lactic acid (LA), which is then converted to lactide (LD) via a two-step process[5]. The resulting LD is polymerized by ring-opening polymerization (ROP) to produce the final PLA product[6]. Process 2 (direct alcoholysis route) explores a novel one-step alcoholysis route where WPLA is first converted to MLA[7 8]. MLA is then directly transformed into LD in a one-step gas-phase process. The final PLA product is synthesized via ROP, similar to Process 1. To investigate the effect of the catalyst, two

scenarios were defined (2a, 2b) corresponding to the use of $TiO_2/SiO_2$ and $TiO_2$ catalysts, respectively[9]. Process 3 (optimised alcoholysis with recycle) builds upon the second route with a key optimisation. To address the conversion of MLA to LD (~42%) observed in Process 2, which leads to material loss, Process 3 was designed to include a recycle loop for unreacted MLA[8,10,11]. This modification aims to enhance the overall LD yield. As with Process 2, this route was also evaluated using the two distinct process systems ($TiO_2/SiO_2$ and $TiO_2$), creating scenarios 3a, 3b[9].

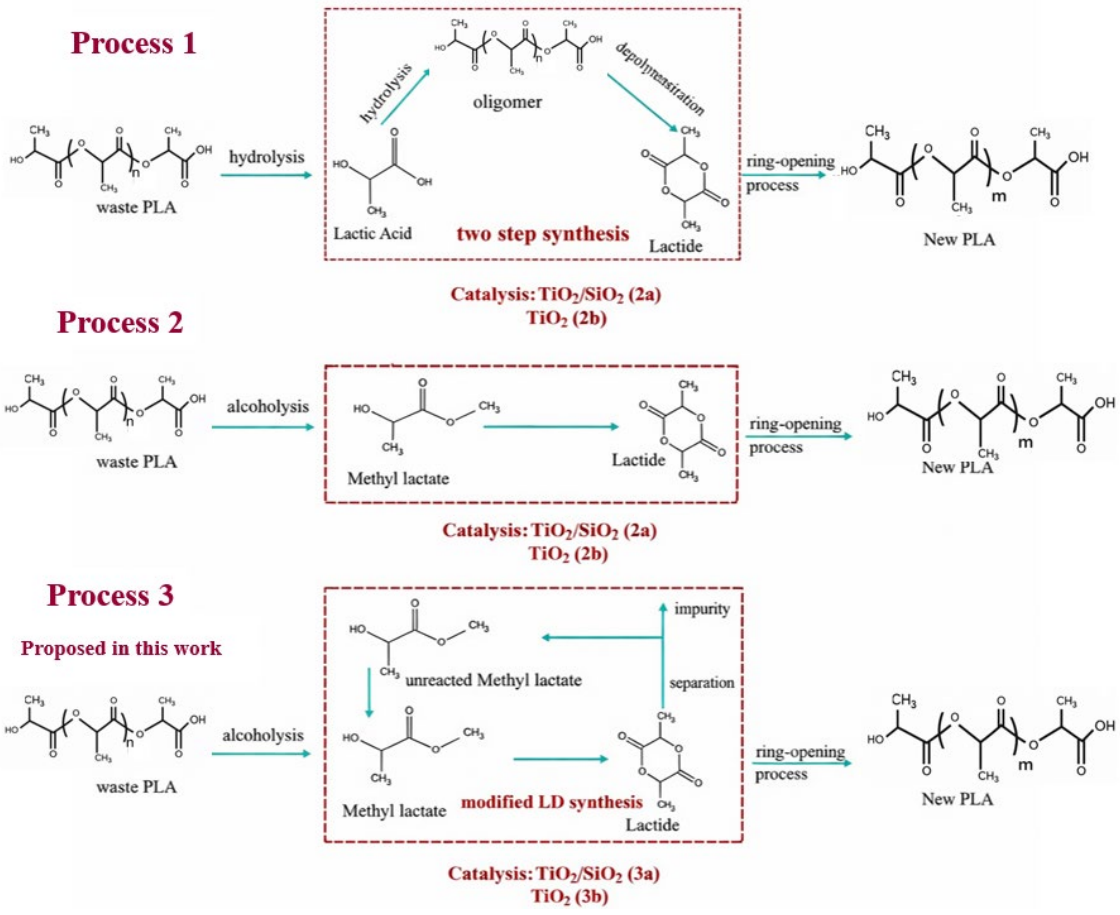


Figure 6.1 Three recycling routes of PLA waste treatment

## 6.1.3 Process modelling details

All process modelling was executed in Aspen Plus®, with the Non-Random Two-Liquid (NRTL) thermodynamic model for property calculations. The missing parameters for PLA and WPLA were estimated via the UNIFAC group contribution method[12,13]. The difference between new PLA products and WPLA was assumed to be a lower average molecular weight for the latter[14]. To ensure a consistent basis for comparison, all process models were designed for a WPLA feed rate of 20,000 kg/hr. Critical performance data, including reaction yield and selectivity for each step, were sourced from literature[5,15] and integrated into the simulations.

## 6.1.4 Techno-Economic Analysis

The economic viability of each scenario was evaluated by estimating the total capital investment and annual operating costs[16]. All financial assumptions and cost data were derived from a comprehensive review of academic literature and industry reports (Table 6.1)[16,17].

### *Capital cost estimation*

The total capital investment was determined as the sum of the fixed capital investment (FCI) and working capital. The FCI covers both direct and indirect cost associated with building and commissioning the plant. Direct costs include equipment procurement and installation as well as ancillary items, such as piping, instrumentation, electrical work, buildings, yard improvements, service utilities, and land. The value of equipment was calculated, following the methodology of Heo[18] and the factors listed in Table 6.1. Indirect costs include engineering and construction services, such as legal fees, the contractor's fee, and contingencies were expressed as fractions of the equipment

purchase cost[18]. After the total capital cost had been obtained, it was annualized with the capital-recovery factor $A_{i,n}$, defined by Eq6.1:

$$A_{i,n} = \frac{i(1+i)^N}{(1+i)^N - 1} \quad (6.1)$$

where *i* is the interest rate and *N* is the lifetime of the equipment. Consistent with previous studies, values of $i = 8$ % and $N = 20$ years were assumed[17]. Working capital was taken as 15% of the FCI to cover start-up requirements, such as the cost of raw materials, utilities, and equipment shakedown expenses[19].

## *Operating cost estimation*

The annual operating cost for each scenario was calculated as the sum of several key components: raw materials, utilities, labour, and various fixed expenses. The consumption rates for raw materials and utilities were quantified directly from the mass and energy balances generated by the Aspen Plus® simulations. Fixed expenses were defined to include costs such as equipment maintenance incurred during routine production and operation[20]. A budget for further research and development was also factored into the total operational expenditure.

To establish a realistic labour cost, data was sourced from the 2023 annual report of a key industry company specializing in PLA production, Zhejiang Hiseng Biomaterials Co., LTD. This report provided a basis for an average weekly labour cost of $413, which translates to an hourly wage of $10.325 based on a standard 40-hour workweek (8 hours/day, 5 days/week). For this study, the baseline labour cost was adjusted to reflect the varying production scales across the different scenarios.

## *Production cost*

The final unit production cost for PLA, expressed in $/kg, was determined using the formula presented in Eq6.2:

$$PLA\ production\ cost = \frac{\text{annual cost}}{\text{annual production rate of PLA}} \quad (6.2)$$

Annual production rate of PLA, was derived from the final product mass flow calculated by the Aspen Plus® simulation. Annual cost represents the summation of the annualised capital cost, total operating cost, and all other fixed expenses, with these components being itemised in Table 6.1.

Table 6.1 Summary of the economic parameters in production cost estimation

| Items | Estimation assumption | Data source |
|---|---|---|
| Plant location | China | assumed |
| Design on-stream factor | 365day*24h*0.95 | assumed |
| Reference year | 2024 | assumed |
| Catalytic | Different catalysts of different scenario | assumed |
| Capital cost | Capital cost=FCI +working capital | |
| Direct cost (DC) | | |
| Equipment purchase cost (EC) | Aspen plus® | Measured |
| Installation | Aspen plus® | Measured |
| piping | 0.31*EC | Mairizal et al., 2023[21] |
| instrumentation | 0.43*EC | Mairizal et al., 2023[21] |
| electrical | 0.10*EC | Mairizal et al., 2023[21] |
| buildings | 0.15*EC | Mairizal et al., 2023[21] |
| yard improvement | 0.12*EC | Mairizal et al., 2023[21] |
| service facilities | 0.55*EC | Mairizal et al., 2023[21] |
| Land | 0.06*EC | Mairizal et al., 2023[21] |
| Indirect Cost (IC) | | |
| Engineering and supervision | 0.32*EC | Mairizal et al., 2023[21] |
| construction expense | 0.34*EC | Mairizal et al., 2023[21] |
| legal expenses | 0.04*EC | Mairizal et al., 2023[21] |
| Contractor's fee | 0.19*EC | Mairizal et al., 2023[21] |
| Contingency | 0.37*EC | Mairizal et al., 2023[21] |
| Fixed capital investment (FCI) | FCI=DC+IC | Mairizal et al., 2023[21] |
| Working capital | 0.15*FCI | Mairizal et al., 2023[21] |
| Operating cost | | |

| | | |
|---|---|---|
| raw materials cost | The sum of feed stock cost and catalyst cost | measured |
| labor cost | Administrative costs and labor cost | measured |
| Utility cost | Aspen plus® | Aryan et al., (2021) [22] |
| Fixed expenses (FE) | | |
| startup costs | 0.09*FCI | Kwan et al.,2018[23] |
| Laboratory cost for QC and QA | 0.15* total labor cost | Kwan et al.,2018[23] |
| equipment maintenance and repair | 0.07*FCI | Kwan et al.,2018[23] |
| operating supplies | 0.15*equipment maintenance and repair cost | Kwan et al.,2018[23] |
| Depreciation (20 year straight line) | 0.05*FCI | Kwan et al.,2018[23] |
| insurance | 0.01*FCI | Kwan et al.,2018[23] |
| Plant overhead costs | 0.5*equipment maintenance and repair cost | Kwan et al.,2018[23] |
| Distribution and marketing costs | 0.02*total operating cost | Kwan et al.,2018[23] |
| Research & Development | 0.05*total operating cost | Kwan et al.,2018[23] |

# 6.2 Results and Discussion

## 6.2.1 Process systems

Process 1, serving as the baseline scenario for the chemical recycling of WPLA, models the conventional hydrolysis pathway. The process flow is detailed in Figure 6.2 with key parameters presented in Table 6.2, which comprises several key unit operations. The main reactors are designated as A2, A4, A6, and A9. Purification is achieved using a series of flash tanks (A3, A5, A7, A10), and a distillation column (A8) is employed for final LD refining[24].

The initial step involves feeding WPLA and water into reactor A2, where hydrolysis occurs at 18℃ for 1.5 hours[25–27]. This stage achieves a high conversion of 85.9% to the LA solution. The efficiency of this conversion is attributed to the use of Diphenyl

phosphate (DPP) as an acidic organocatalyst[5]. Priced commercially between $70–150 per kilogram, DPP facilitates a rapid and stochastic hydrolysis of PLA. As proposed by Wanhua Wu[28], the mechanism involves a dual activation of both the PLA ester bonds and water, a mode of action analogous to the bifunctional activation seen in other DPP-catalyzed reactions like the ROP of cyclic esters[29].

Following the hydrolysis, the process models the traditional two-step method for converting LA to LD. First, in flash tank A3, water is removed from the LA solution to generate a low molecular weight prepolymer, commonly known as an oligomer[30]. Subsequently, in reactor A4, this oligomerization is advanced through an autocatalytic esterification reaction at high temperature (200°C) and low pressure (0.07-0.33 bar). The temperature control is essential in this reactor because the average molecular weight (Mn) of the resulting oligomer depends on temperature. Moreover, the Mn also directly influences the efficiency of the subsequent depolymerization step, which proceeds with a reported yield of 80–95%[31,32].

The solvent of oligomer is then transferred to the depolymerization reactor (A6). The oligomers are converted into cyclic dimers (LD) under high vacuum (10-50 torr) and high temperature (200-240°C) with $Sn(Oct)_2$ catalyst[33,34]. The catalyst plays a crucial role in improving both the conversion rate and the stereoselectivity towards the desired l-lactide (L-LD) over the meso-lactide (meso-LD) by-product. After reaction, unreacted oligomers are removed via another flash separation step. The crude LD stream is then purified in a distillation column (A8), specified with 30 stages and a reflux ratio of 15. The final step involves the polymerization of the purified L-LD in reactor A9 to produce the final PLA product, which is recovered with 100% efficiency through separation based on boiling point differences[19,35,36].

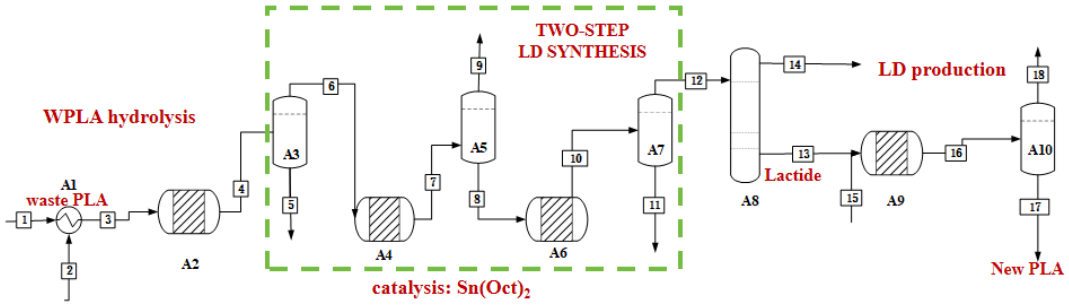


Figure 6.2 Process flow of Process 1

Table 6.2 Key parameters for Process 1

| variable | value | variable | value |
|---|---|---|---|
| A2 temperature | 180°C [37] | A4 temperature | 200°C[5] |
| A2 pressure | 1bar [37] | A4 pressure | 0.33bar [5] |
| A3 temperature | 200°C [5,18] | A6 pressure | 0.01bar [6] |
| A3 pressure | 0.33bar [5] | A8 stage | 30 [7] |
| A5 temperature | 220°C [5] | A9 temperature | 80°C [8] |
| A5 pressure | 0.01bar [5] | A9 pressure | 1 bar [8] |
| oligomer PLA | 594g/mol [5] | A10 temperature | 220°C [11] |
| catalyst | $Sn(Oct)_2$,0.2wt% | A10 pressure | 0.1 bar[11] |

In contrast to Process 1 (conventional hydrolysis route), Processes 2 and 3 are based on the alcoholysis of PLA to produce value-added products. The initial step for both processes (in Figure 6.3 and Figure 6.4), is the transesterification of WPLA with methanol in reactor B2 to produce MLA[38]. This solvent-free reaction is conducted at 130°C to ensure the polymer fully dissolves in the methanol with Zinc (II) Octoate catalyst[7,8]. The resulting stream (24) is then sent to a flash separator (B3) to remove water and impurities. The purified, evaporated MLA (stream 25) is subsequently mixed with a nitrogen carrier stream (1.19 kg/h, 1.00 bar) in a mixer (B4) before entering the next stage [39,40].

The MLA/$N_2$ mixture (stream 28) is then fed into a fixed-bed reactor (B5) for the gas-phase conversion to LD. The simulation models a custom reactor setup involving

parallel quartz tubes (480 mm length, 4 mm ID) packed with 10-300 mg of catalyst (5 wt%) on a quartz support. The catalysts considered in the different scenarios are $TiO_2/SiO_2$ and $TiO_2$. Prior to the reaction, the catalyst is pretreated in a 20 ml/min $N_2$ flow at 300°C for 1 hour. The reaction is conducted at a carefully controlled 220°C to ensure stable operation.

The reactor effluent (stream 29) enters a flash tank (B6) operating at 70°C and 0.1 bar. This step is designed to separate the volatile methanol (boiling point 64.7°C) from the high temperate boiling point LD products (L-LD and meso-LD, boiling point ~230°C)[35]. A key challenge in Process 2 is the relatively low conversion of MLA to LD cited at only 42%, which results in significant feedstock waste[9]. To address this, Process 3 (Figure 6.4) shows a critical modification: the unreacted MLA separated downstream is recycled back to the inlet of reactor B5. In the final purification stage, common to both processes, the crude LD stream (stream 54) enters a distillation column (B7). Operating with a reflux ratio of 6.11, this column is designed to produce L-LD at 99% purity as the bottom product (stream 55)[41]. The use of a low temperature coolant is specified to minimize the formation of meso-LD during purification. Final polymerization to PLA occurs in reactors B8 and B9. The key operating parameters for these processes are summarized in Table 6.3.

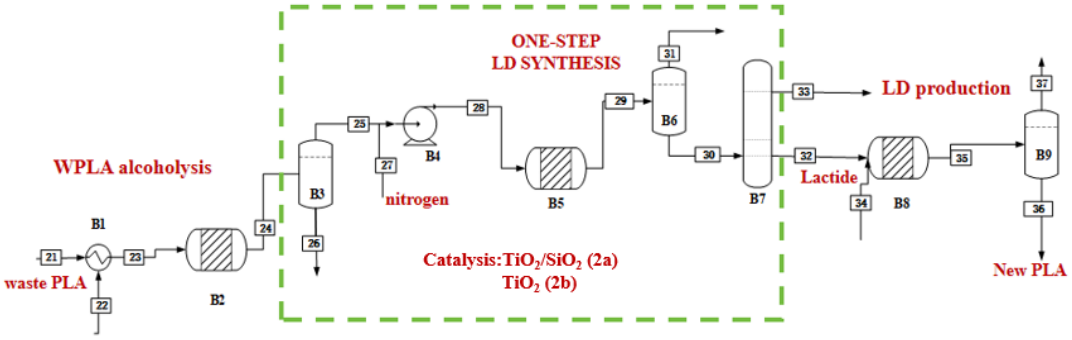


Figure 6.3 Process 2a, 2b flow of PLA synthesis

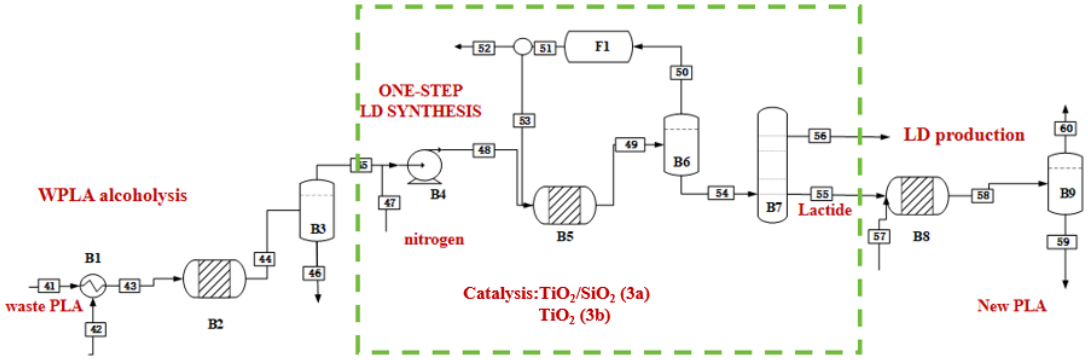


Figure 6.4 Process 3a, 3b flow of the modified one-step PLA synthesis

Table 6.3 Key parameters for Process 2 and Process 3

| variable | value | variable | value |
|---|---|---|---|
| B2 temperature | 130°C [42] | B6 temperature | 70°C [43] |
| B2 pressure | 1 bar [42] | B6 pressure | 0.1bar [43] |
| B3 temperature | 140°C [44] | B7 lactide product | 0.99 [18] |
| B3 vapor | 0.999 [44] | B7 stage | 30 [18] |
| B5 reaction number | 6 [44] | B8 temperature | 80°C [45] |
| B5 temperature | 220°C [44] | B8 pressure | 1 bar [45] |
| catalyst | $TiO_2/SiO_2$, $TiO_2$ | B9 temperature | 220°C [46] |
| catalyst wt% | 5% [9] | B9 pressure | 0.1 bar [46] |

## 6.2.2 Mass and energy balance

The conventional hydrolysis route (Process 1), was simulated as the baseline scenario. From an initial WPLA feedstock of 20,000 kg/h, the hydrolysis step with DPP

catalyst yields a 96.8% LA solution at a flow rate of 21,449 kg/h[47]. Following a series of downstream separation and purification steps, the LA is converted to LD, with a final composition of 82.35% L-LD and 14.52% meso-LD. An analysis of this route shows that while the two-step synthesis achieves a higher overall conversion to LD compared to the one-step methods, it suffers from lower selectivity for the desired L-LD isomer. The reduced selectivity is attributed to racemization during the process and combined with the hygroscopic nature of the LD intermediate, which presents significant challenges for the purification stages required to obtain high-purity L-LD. The total annual production of PLA from this baseline process is calculated to be 59,542 tonnes.

In contrast, the alcoholysis pathways, which are Processes 2 and 3, begin with the transesterification of the 20,000 kg/h WPLA feedstock into a 95.3% MLA solution, which is produced at a rate of 29,368.39 kg/h with $Sn(Oct)_2$ catalyst. A comparative analysis of the subsequent gas-phase conversion of MLA to LD (Table 6.4) reveals significant performance differences among the various catalysts. For the non-recycle scenarios, Process 2a (using $TiO_2/SiO_2$) yields the highest annual L-LD production at 69,332 tonnes, outperforming both Process 2a ($TiO_2$/ $SiO_2$) and 2b ($TiO_2$). The catalytic performance is linked to the robust catalytic activity of $TiO_2$ supported on amorphous silica, which provides a high turnover frequency and results in over 90% selectivity with minimal racemization[7].

The introduction of a recycle loop for unreacted MLA in Process 3 is shown to increase the overall MLA conversion rate. However, this optimization came at the expense of a slight reduction in L-LD selectivity when comparing catalyst performance between Process 2 and Process 3 (e.g., 2a vs. 3a). Across all scenarios, the $TiO_2$ catalyst (Process 2b) results in the lowest LD yield. The yield of LD is only marginally improved

by the MLA recycle in Process 3b, a result attributes to the lower number or reduced activity of surface-active sites on the unsupported catalyst[9].

For the final conversion of LD to PLA, all seven scenarios employed $Sn(Oct)_2$ as the catalyst for the ROP with benzyl alcohol as an initiator, a combination known to produce high molecular weight polymers efficiently[13]. The final calculated annual PLA production rates for each scenario are as follows: 59,542 tonnes/year for Process 1; 63,828 and 25,899 tonnes/year for Processes 2a and 2b, respectively; and 95,188 and 32,718 tonnes/year for Processes 3a and 3b, respectively. The difference in the PLA production rates demonstrates that the $TiO_2/SiO_2$ catalyst (Process 3a) in the modified recycle process achieves the highest production.

Table 6.4 The mass balance of different processes and scenarios

| Process | Flow rate of stream in various reaction steps (kg/h) | | | |
|---|---|---|---|---|
| | WPLA | MLA/LA | LD | PLA |
| 1 | 20000.0 | 21472.5 | 7313.9 | 6797.0 |
| 2a | 20000.0 | 28020.0 | 7507.7 | 7286.4 |
| 2b | 20000.0 | 28020.0 | 3029.2 | 2956.5 |
| 3a | 20000.0 | 27991.0 | 11357.7 | 10866.3 |
| 3b | 20000.0 | 27991.0 | 8199.6 | 3931.5 |

Figure 6.5 compares the annual energy demand of the different process scenarios. Process 1 is the most energy consumption case, drawing about 2.75 × 10^12 Wh per year, Process 2b requires only 1.42 × 10^12 Wh per year, which is the lowest of all cases. In all scenarios, purification and cooling duties account for up to 30% of total utility costs. In the two-step LD synthesis route, these same operations typically make up just over 15 %, which pushes the overall energy cost above that of the alternative options. As a result, the 'WPLA–MLA–LD–PLA' process offers a more energy-efficient performance. A direct

comparison between Process 2 and Process 3 further shows that Process 2 is the more economical of the two, because it relies on fewer pieces of equipment.

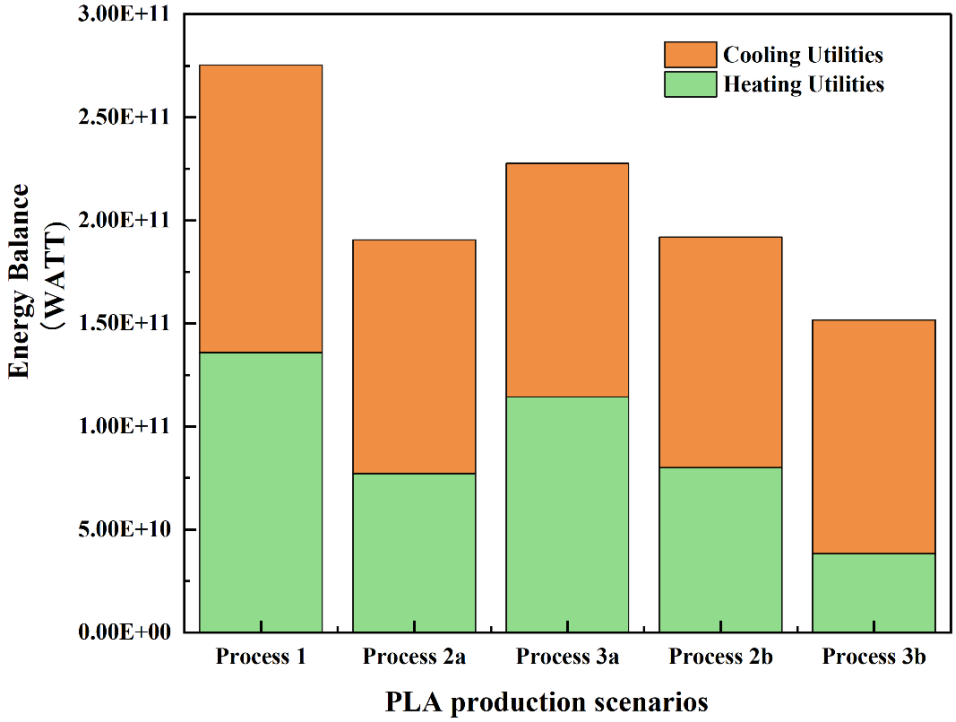


Figure 6.5 Energy balance of all PLA production scenarios

## 6.2.3 Capital cost

A detailed breakdown of the capital costs for each scenario, including the FCI and working capital, is presented in Figure 6.6. A clear distinction emerges when comparing the equipment expenses. The conventional Process 1 exhibits significantly higher annual costs for both equipment purchase ($43.57/tonne PLA) and installation ($83.54/tonne PLA) compared to the alcoholysis routes. For instance, Process 2a has corresponding costs of $33.77 and $62.85 per tonne PLA, while Process 3a is even lower at $30.37 and $53.75 per tonne PLA. This cost disparity is primarily due to the two-step lactide synthesis in Process 1, which requires more process units. A major contributor to the

equipment costs across all scenarios is purification, which accounted for 30% of the total equipment cost. A purification cost contribution of 30% is notably higher than the typical 15% reported for conventional LD synthesis, reinforcing the conclusion that Process 1 requires a more intensive and costly refinement stage to achieve high-purity L-LD[16 48]. Other capital costs, such as land and construction, are calculated based on established literature percentages[11]. To cover the cost of the initial plant, such as raw materials, maintenance, management, employee training, and equipment testing, working capital was assumed to be 15% of the FCI.

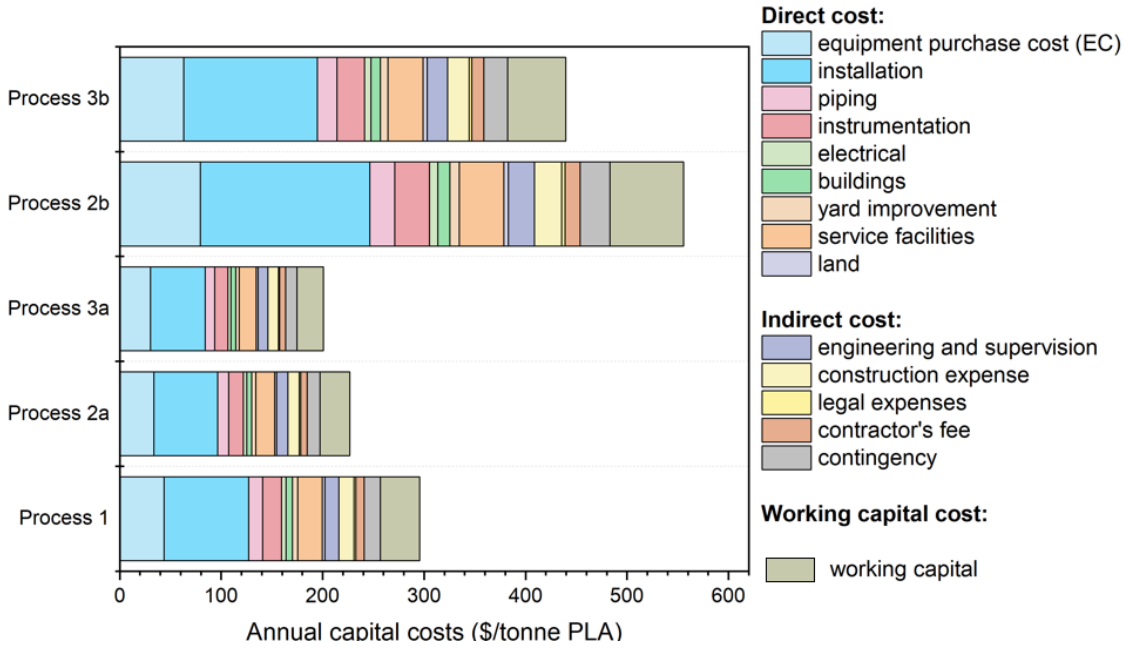


Figure 6.6 Capital costs and its breakdown for all the PLA production scenarios

## 6.2.4 Operation cost

A detailed breakdown of the estimated annual operating costs for each of the seven scenarios is presented in Figure 6.7. For a standard operational year of 8322 hours, the total calculated costs are around $113.3 million (Process 1), $105.5 million (Process 2a), $121.7 million (Process 2b), $154.1 million (Process 3a) and $1422.0 million (Process

3b). An analysis of the cost distribution for the baseline Process 1 shows that costs were dominated by raw materials (34.31%) and utilities (41.26%). The high utility demand, particularly for high-pressure steam, is a direct consequence of the two-step synthesis LD route, which requires more extensive equipment and procedures than the one-step process routes. Consequently, the single reactor design of Process 2a benefits from a significant reduction in utility costs. However, the additional of a separator and recovery loop into Process 3a increases the mass flow of material requiring purification, resulting in higher utility costs compared to the non-recovery Process 2a.

The difference in raw material costs between the alcoholysis scenarios (2a/b and 3a/b) is the catalyst cost for the MLA-to-LD conversion. The $TiO_2/SiO_2$ catalyst used in Processes 2a and 3a is the most economical, at \$182 and \$156 per tonne of LD, respectively. In contrast, the $TiO_2$ catalyst cost for Processes 2b and 3b is identical at \$544, a consequence of its low conversion efficiency and the fixed amount of catalyst loaded in the reactor.

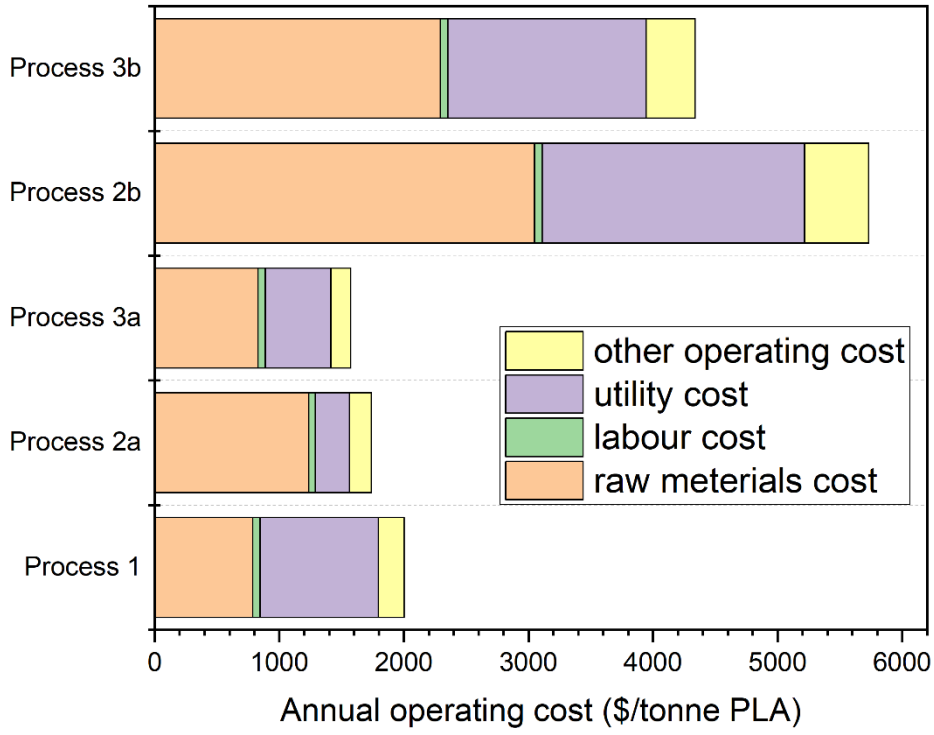


Figure 6.7 Operating Costs and its breakdown for all the PLA production scenarios

## 6.2.5 Production cost

Achieving a circular plastics economy, which depends on continued progress in recycling technologies and process design. The cost comparisons summarised in Figure 6.8 show that scenarios 2b and 3b give the most expensive PLA, because their raw material and utility requirements are higher than other options. The reference conventional route (Process 1) produces PLA at roughly US $2,299/tonne. By contrast, scenario 3a delivers the most favourable economics, lowering the PLA production cost to US $1,773/tonne, which represents a reduction of 22.88%, relative to the benchmark. Output also rises in two scenarios: Process 3a lifts annual production from 59,542 to 95,188 tonnes/year (≈ 60% increase), while in Process 3b pushes it to 98,081 tonnes/year (≈ 65% increase).

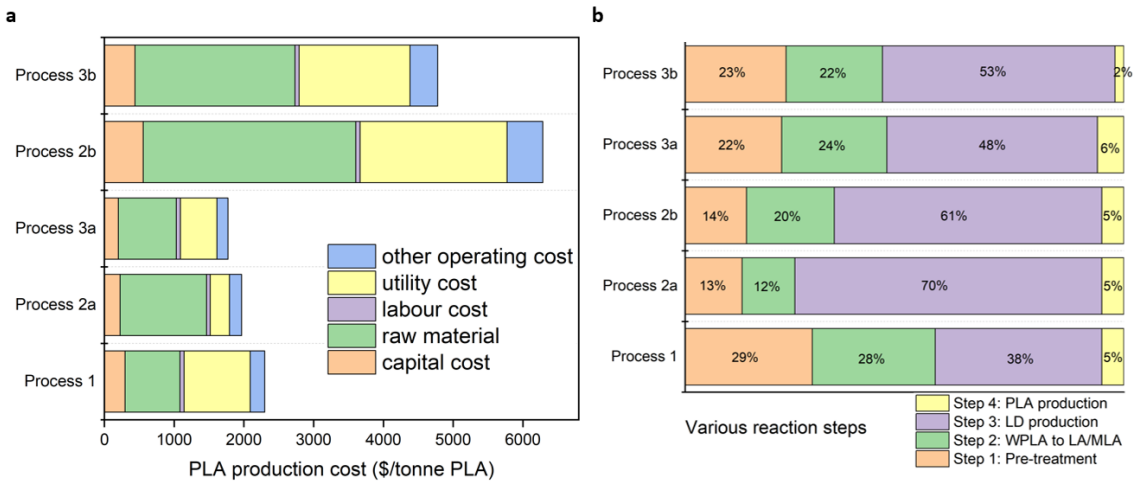


Figure 6.8 (a) PLA production cost and its breakdown for various scenarios; (b)Breakdown of the PLA production cost by various reaction steps

*note: Process 1 (the traditional industrial approach) is considered as the benchmark

## 6.2.6 Sensitivity analysis

Following the identification of Process 3a as the most promising option is based on economic analysis, the sensitivity analysis is conducted to evaluate the robustness of this conclusion against key parameter uncertainties, such as capital cost and operating cost. The analysis involves systematically varying input parameters by ±10% from their baseline values. To quantify the resulting impact on process outputs, a sensitivity ratio is calculated for each variation according to Eq6.3.

$$\text{Sensitivity ratio} = \frac{\frac{\Delta \text{result}}{\text{intial result}}}{\frac{\Delta \text{parameter}}{\text{intial parameter}}} \tag{6.3}$$

The results of this analysis are presented in Figure 6.9. For PLA unit production cost, the feedstock flow rate is identified as the most critical parameter among the eight tested. A ±10% change in feed flow yielded significant sensitivity ratios of 1.61 (for a -10% change) and 2.97 (for a +10% change), indicating a significant impact on product

cost. In contrast, other factors, such as catalyst price, exerted a negligible influence, with sensitivity ratios of only 0.01.

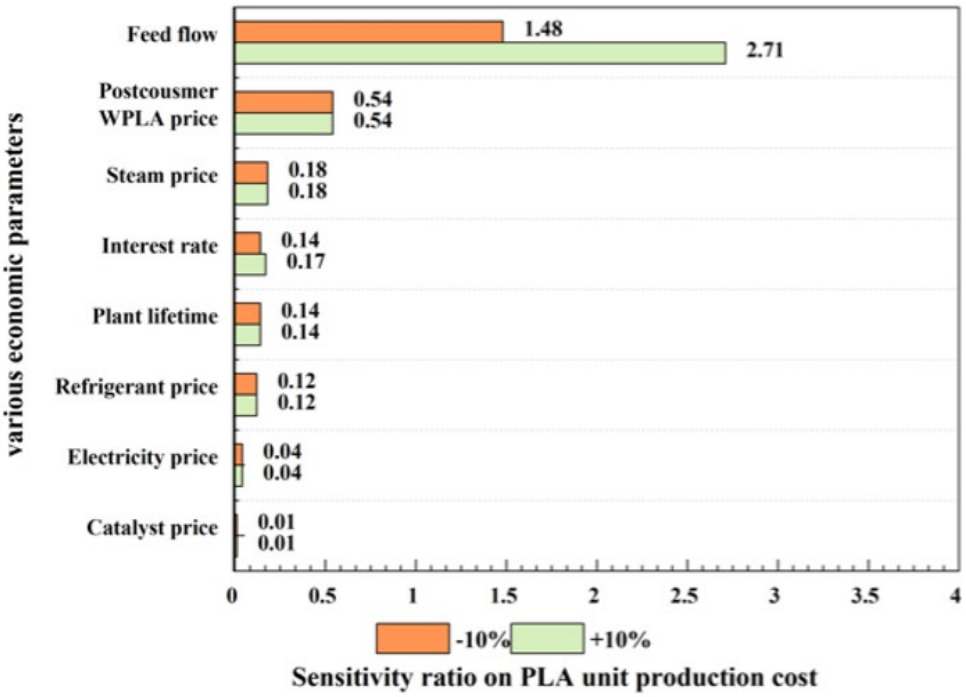


Figure 6.9 Sensitivity analysis of the PLA production cost

# 6.3 Conclusions

In this chapter, the WPLA recycling simulations are evaluated through three processes method across five operating scenarios. Process 3a, a one-step LD synthesis with $TiO_2/SiO_2$ catalyst, which is the most positive option. Relative to the benchmark conventional process, annual PLA output rises from $5.96 \times 10^4$ tonnes to $9.04 \times 10^4$ tonnes (≈ 60% increase), while the production cost falls by 22.9% to US$1773/tonne. Sensitivity analysis of the key parameters indicates that the amount of catalyst added, the feedstock flow rate, and raw material prices all have significant impacts on PLA production cost. It can be concluded that converting PLA into value-added chemicals offers a multifaceted approach that addresses urgent environmental challenges posed by plastic waste while

creating economic opportunities. By promoting the transition to a circular plastics economy, a more sustainable plastics industry can be achieved, one that coexists harmoniously with the environment and contributes to global goals of waste reduction and resource conservation.

# References


(1) Maga, D.; Hiebel, M.; Thonemann, N. Life Cycle Assessment of Recycling Options for Polylactic Acid. Resour. Conserv. Recycl. 2019, 149, 86–96. https://doi.org/10.1016/j.resconrec.2019.05.018.

(2) Vogt, B. D.; Stokes, K. K.; Kumar, S. K. Why Is Recycling of Postconsumer Plastics so Challenging? ACS Appl. Polym. Mater. 2021, 3 (9), 4325–4346. https://doi.org/10.1021/acsapm.1c00648.

(3) Lange, J.-P. Managing Plastic Waste—Sorting, Recycling, Disposal, and Product Redesign. ACS Sustain. Chem. Eng. 2021, 9 (47), 15722–15738. https://doi.org/10.1021/acssuschemeng.1c05013.

(4) Paiva, R.; Aznar, M.; Wrona, M.; De Lima Batista, A. P.; Nerín, C.; Cruz, S. A. Biobased Polymer Recycling: A Comprehensive Dive into the Recycling Process of PLA and Its Decontamination Efficacy. ACS Appl. Polym. Mater. 2024, 6 (19), 12154–12163. https://doi.org/10.1021/acsapm.4c02230.

(5) Hu, Y.; Daoud, W. A.; Fei, B.; Chen, L.; Kwan, T. H.; Ki Lin, C. S. Efficient ZnO Aqueous Nanoparticle Catalysed Lactide Synthesis for Poly(Lactic Acid) Fibre Production from Food Waste. J. Clean. Prod. 2017, 165, 157–167. https://doi.org/10.1016/j.jclepro.2017.07.067.

(6) Upare, P. P.; Yoon, J. W.; Hwang, D. W.; Lee, U.-H.; Hwang, Y. K.; Hong, D.-Y.; Kim, J. C.; Lee, J. H.; Kwak, S. K.; Shin, H.; Kim, H.; Chang, J.-S. Design of a Heterogeneous Catalytic Process for the Continuous and Direct Synthesis of Lactide from Lactic Acid. Green Chem. 2016, 18 (22), 5978–5983. https://doi.org/10.1039/C6GC02405J.

(7) Román-Ramírez, L. A.; Mckeown, P.; Jones, M. D.; Wood, J. Poly(Lactic Acid) Degradation into Methyl Lactate Catalyzed by a Well-Defined Zn(II) Complex. ACS Catal. 2019, 9 (1), 409–416. https://doi.org/10.1021/acscatal.8b04863.

(8) Román-Ramírez, L. A.; McKeown, P.; Jones, M. D.; Wood, J. Kinetics of Methyl Lactate Formation from the Transesterification of Polylactic Acid Catalyzed by Zn(II) Complexes. ACS Omega 2020, 5 (10), 5556–5564. https://doi.org/10.1021/acsomega.0c00291.

(9) De Clercq, R.; Dusselier, M.; Poleunis, C.; Debecker, D. P.; Giebeler, L.; Oswald, S.; Makshina, E.; Sels, B. F. Titania-Silica Catalysts for Lactide Production from Renewable Alkyl Lactates: Structure–Activity Relations. ACS Catal. 2018, 8 (9), 8130–8139. https://doi.org/10.1021/acscatal.8b02216.

(10) Mo, L.; Shao-Tong, J.; Li-Jun, P.; Zhi, Z.; Shui-Zhong, L. Design and Control of Reactive Distillation for Hydrolysis of Methyl Lactate. Chem. Eng. Res. Des. 2011, 89 (11), 2199–2206. https://doi.org/10.1016/j.cherd.2011.03.001.

(11) Anbreen, A.; Ramzan, N.; Faheem, M. A Heat-Integrated Reactive Distillation Process for Methyl Lactate Hydrolysis. Chem. Eng. Process. - Process Intensif. 2022, 170, 108695. https://doi.org/10.1016/j.cep.2021.108695.

(12) Getino, L.; Martín, J. L.; Chamizo-Ampudia, A. A Review of Polyhydroxyalkanoates: Characterization, Production, and Application from Waste. Microorganisms 2024, 12 (10), 2028. https://doi.org/10.3390/microorganisms12102028.

(13) Wu, D.; Lv, Y.; Guo, R.; Li, J.; Habadati, A.; Lu, B.; Wang, H.; Wei, Z. Kinetics of Sn(Oct)2-Catalyzed Ring Opening Polymerization of ε-Caprolactone. Macromol. Res. 2017, 25 (11), 1070–1075. https://doi.org/10.1007/s13233-017-5148-z.

(14) Yang, R.; Xu, G.; Dong, B.; Hou, H.; Wang, Q. A "Polymer to Polymer" Chemical Recycling of PLA Plastics by the "DE–RE Polymerization" Strategy. Macromolecules 2022, 55 (5), 1726–1735. https://doi.org/10.1021/acs.macromol.1c02085.

(15) Horváth, T.; Marossy, K.; Szabó, T. J. Ring-Opening Polymerization and Plasticization of Poly(L-Lactic)Acid by Adding of Glycerol-Dioleate. J. Therm. Anal. Calorim. 2022, 147 (3), 2221–2227. https://doi.org/10.1007/s10973-020-10540-1.

(16) Shokrollahi, M.; Teymouri, N.; Ashrafi, O.; Navarri, P.; Khojasteh-Salkuyeh, Y. Methane Pyrolysis as a Potential Game Changer for Hydrogen Economy: Techno-Economic Assessment and GHG Emissions. Int. J. Hydrog. Energy 2024, 66, 337–353. https://doi.org/10.1016/j.ijhydene.2024.04.056.

(17) Kwan, T. H.; Hu, Y.; Lin, C. S. K. Techno-Economic Analysis of a Food Waste Valorisation Process for Lactic Acid, Lactide and Poly(Lactic Acid) Production. J. Clean. Prod. 2018, 181, 72–87. https://doi.org/10.1016/j.jclepro.2018.01.179.

(18) Heo, S.; Park, H. W.; Lee, J. H.; Chang, Y. K. Design and Evaluation of Sustainable Lactide Production Process with an One-Step Gas Phase Synthesis Route. ACS Sustain. Chem. Eng. 2019, 7 (6), 6178–6184. https://doi.org/10.1021/acssuschemeng.8b06383.

(19) Weyand, J.; Habermeyer, F.; Dietrich, R.-U. Process Design Analysis of a Hybrid Power-and-Biomass-to-Liquid Process – An Approach Combining Life Cycle and Techno-Economic Assessment. Fuel 2023, 342, 127763. https://doi.org/10.1016/j.fuel.2023.127763.

(20) Mairizal, A. Q.; Sembada, A. Y.; Tse, K. M.; Haque, N.; Rhamdhani, M. A. Techno-Economic Analysis of Waste PCB Recycling in Australia. Resour. Conserv. Recycl. 2023, 190, 106784. https://doi.org/10.1016/j.resconrec.2022.106784.

(21) Mairizal, A. Q.; Sembada, A. Y.; Tse, K. M.; Haque, N.; Rhamdhani, M. A. Techno-Economic Analysis of Waste PCB Recycling in Australia. Resour. Conserv. Recycl. 2023, 190, 106784. https://doi.org/10.1016/j.resconrec.2022.106784.

(22) Aryan, V.; Maga, D.; Majgaonkar, P.; Hanich, R. Valorisation of Polylactic Acid (PLA) Waste: A Comparative Life Cycle Assessment of Various Solvent-Based Chemical Recycling Technologies. Resour. Conserv. Recycl. 2021, 172, 105670. https://doi.org/10.1016/j.resconrec.2021.105670.

(23) Kwan, T. H.; Hu, Y.; Lin, C. S. K. Techno-Economic Analysis of a Food Waste Valorisation Process for Lactic Acid, Lactide and Poly(Lactic Acid) Production. J. Clean. Prod. 2018, 181, 72–87. https://doi.org/10.1016/j.jclepro.2018.01.179.

(24) Su, C.-Y.; Yu, C.-C.; Chien, I.-L.; Ward, J. D. Plant-Wide Economic Comparison of Lactic Acid Recovery Processes by Reactive Distillation with Different Alcohols. Ind. Eng. Chem. Res. 2013, 52 (32), 11070–11083. https://doi.org/10.1021/ie303192x.

(25) Gujjala, L. K. S.; Won, W. Process Development, Techno-Economic Analysis and Life-Cycle Assessment for Laccase Catalyzed Synthesis of Lignin Hydrogel. Bioresour. Technol. 2022, 364, 128028. https://doi.org/10.1016/j.biortech.2022.128028.

(26) Clercq, R.; Dusselier, M.; Makshina, E.; Sels, B. F. Catalytic Gas-Phase Production of Lactide from Renewable Alkyl Lactates. Angew. Chem. Int. Ed. 2018, 57 (12), 3074–3078. https://doi.org/10.1002/anie.201711446.

(27) Piemonte, V.; Gironi, F. Kinetics of Hydrolytic Degradation of PLA. J. Polym. Environ. 2013, 21 (2), 313–318. https://doi.org/10.1007/s10924-012-0547-x.

(28) Wu, W.; Zhai, H.; Wu, K.; Wang, X.; Rao, W.; Ding, J.; Yu, L. Cheap Organocatalyst Diphenyl Phosphate for Efficient Chemical Recycling of Poly(Lactic Acid), Other Polyesters and Polycarbonates. Chem. Eng. J. 2024, 480, 148131. https://doi.org/10.1016/j.cej.2023.148131.

(29) Cappello, V.; Sun, P.; Zang, G.; Kumar, S.; Hackler, R.; Delgado, H. E.; Elgowainy, A.; Delferro, M.; Krause, T. Conversion of Plastic Waste into High-Value Lubricants: Techno-Economic Analysis and Life Cycle Assessment. Green Chem. 2022, 24 (16), 6306–6318. https://doi.org/10.1039/D2GC01840C.

(30) Gironi, F.; Frattari, S.; Piemonte, V. PLA Chemical Recycling Process Optimization: PLA Solubilization in Organic Solvents. J. Polym. Environ. 2016, 24 (4), 328–333. https://doi.org/10.1007/s10924-016-0777-4.

(31) Dolzhenko, A. V. Ethyl Lactate and Its Aqueous Solutions as Sustainable Media for Organic Synthesis. Sustain. Chem. Pharm. 2020, 18, 100322. https://doi.org/10.1016/j.scp.2020.100322.

(32) Wu, L.; Ding, J. In Vitro Degradation of Three-Dimensional Porous Poly(d,l-Lactide-Co-Glycolide) Scaffolds for Tissue Engineering. Biomaterials 2004, 25 (27), 5821–5830. https://doi.org/10.1016/j.biomaterials.2004.01.038.

(33) Heo, S.; Park, H. W.; Lee, J. H.; Chang, Y. K. Design and Evaluation of Sustainable Lactide Production Process with an One-Step Gas Phase Synthesis Route. ACS Sustain. Chem. Eng. 2019, 7 (6), 6178–6184. https://doi.org/10.1021/acssuschemeng.8b06383.

(34) Yoo, D. K.; Kim, D.; Lee, D. S. Reaction Kinetics for the Synthesis of Oligomeric Poly(Lactic Acid). Macromol. Res. 2005, 13 (1), 68–72. https://doi.org/10.1007/BF03219017.

(35) Tsuji, H.; Kondoh, F. Synthesis of Meso-Lactide by Thermal Configurational Inversion and Depolymerization of Poly( l -Lactide) and Thermal Configurational Inversion of Lactides. Polym. Degrad. Stab. 2017, 141, 77–83. https://doi.org/10.1016/j.polymdegradstab.2017.05.016.

(36) More, N.; Avhad, M.; Utekar, S.; More, A. Polylactic Acid (PLA) Membrane—Significance, Synthesis, and Applications: A Review. Polym. Bull. 2023, 80 (2), 1117–1153. https://doi.org/10.1007/s00289-022-04135-z.

(37) Zhang, L.; He, Y.; Jiang, L.; Shi, Y.; Hao, L.; Huang, L.; Lyu, M.; Wang, S. Plastic Additives as a New Threat to the Global Environment: Research Status, Remediation Strategies and Perspectives. Environ. Res. 2024, 263, 120007. https://doi.org/10.1016/j.envres.2024.120007.

(38) Mo, L.; Shao-Tong, J.; Li-Jun, P.; Zhi, Z.; Shui-Zhong, L. Design and Control of Reactive Distillation for Hydrolysis of Methyl Lactate. Chem. Eng. Res. Des. 2011, 89 (11), 2199–2206. https://doi.org/10.1016/j.cherd.2011.03.001.

(39) Madhavan Nampoothiri, K.; Nair, N. R.; John, R. P. An Overview of the Recent Developments in Polylactide (PLA) Research. Bioresour. Technol. 2010, 101 (22), 8493–8501. https://doi.org/10.1016/j.biortech.2010.05.092.

(40) Mohamed, B. A.; O'Boyle, M.; Li, L. Y. Co-Pyrolysis of Sewage Sludge with Lignocellulosic and Algal Biomass for Sustainable Liquid and Gaseous Fuel Production: A Life Cycle Assessment and Techno-Economic Analysis. Appl. Energy 2023, 346, 121318. https://doi.org/10.1016/j.apenergy.2023.121318.

(41) Van Wouwe, P.; Dusselier, M.; Vanleeuw, E.; Sels, B. Lactide Synthesis and Chirality Control for Polylactic Acid Production. ChemSusChem 2016, 9 (9), 907–921. https://doi.org/10.1002/cssc.201501695.

(42) Akpan, E. D.; Ojwach, S. O.; Omondi, B.; Nyamori, V. O. Zn( II ) and Cu( II ) Formamidine Complexes: Structural, Kinetics and Polymer Tacticity Studies in the Ring-Opening Polymerization of ε-Caprolactone and Lactides. New J. Chem. 2016, 40 (4), 3499–3510. https://doi.org/10.1039/C5NJ03159A.

(43) Pomalaza, G.; De Clercq, R.; Dusselier, M.; Sels, B. How Substituent Effects Influence the Thermodynamics and Kinetics of Gas-Phase Transesterification of Alkyl Lactates to Lactide Using TiO2/SiO2. Appl. Catal. B Environ. 2022, 300, 120747. https://doi.org/10.1016/j.apcatb.2021.120747.

(44) De Clercq, R.; Dusselier, M.; Makshina, E.; Sels, B. F. Catalytic Gas‐Phase Production of Lactide from Renewable Alkyl Lactates. Angew. Chem. Int. Ed. 2018, 57 (12), 3074–3078. https://doi.org/10.1002/anie.201711446.

(45) Egiazaryan, T. A.; Makarov, V. M.; Moskalev, M. V.; Razborov, D. A.; Fedushkin, I. L. Synthesis of Lactide from Alkyl Lactates Catalyzed by Lanthanide Salts. Mendeleev Commun. 2019, 29 (6), 648–650. https://doi.org/10.1016/j.mencom.2019.11.014.

(46) Groot, W. J.; Borén, T. Life Cycle Assessment of the Manufacture of Lactide and PLA Biopolymers from Sugarcane in Thailand. Int. J. Life Cycle Assess. 2010, 15 (9), 970–984. https://doi.org/10.1007/s11367-010-0225-y.

(47) Cunha, B. L. C.; Bahú, J. O.; Xavier, L. F.; Crivellin, S.; de Souza, S. D. A.; Lodi, L.; Jardini, A. L.; Filho, R. M.; Schiavon, M. I. R. B.; Concha, V. O. C.; Severino, P.; Souto, E. B. Lactide: Production Routes, Properties, and Applications. Bioengineering 2022, 9 (4), 164. https://doi.org/10.3390/bioengineering9040164.

(48) Ioannidou, S. M.; Ladakis, D.; Moutousidi, E.; Dheskali, E.; Kookos, I. K.; Câmara-Salim, I.; Moreira, M. T.; Koutinas, A. Techno-Economic Risk Assessment, Life Cycle Analysis and Life Cycle Costing for Poly(Butylene Succinate) and Poly(Lactic Acid) Production Using Renewable Resources. Sci. Total Environ. 2022, 806, 150594. https://doi.org/10.1016/j.scitotenv.2021.150594.

# Chapter 7

# Conclusions

This chapter first concludes the major contributions of the thesis and highlights the broader impact. It then reviews current constraints of the thesis and outlines promising directions for future investigation.

# 7.1 Findings

This thesis explores the urgent need for a circular economy for post-consumer PLA. Employing a cross-scale framework of "material comparison → reaction process → catalyst improvement → system-level evaluation", the work systematically explores the circular economy potential of post-consumer PLA.

A multi-criteria decision analysis covering mechanical, thermal, chemical and environmental metrics comprehensively compared the differences between PLA and other polymers, including HDPE, LDPE, PET, PP, PVC, PS, PC, PCL, PBAT, PBS, PLA, PHBV, TPS, CA, bio-based PA, bio-PET, and bio-PBS. PLA combines renewable raw materials, a significant and growing market, material properties with strong mechanical properties (e.g. high tensile strength), and a clear set of challenges - notably brittleness and the urgent need for efficient closed-loop recycling systems.

Experiments and DFT calculations were then performed for the core step of PLA recycling (MLA → LD). A one-pot liquid-phase process route with titanium-based catalysts (Titania-silica and $TiO_2$) is developed to convert MLA into LD. Across 170–220 °C, Titania-silica consistently outperforms $TiO_2$, achieving 62 % MLA conversion and 49 % LD selectivity at 220 °C, whereas anatase remains below 35 % MLA conversion and 13 % LD selectivity. The superior activity is attributed to atomically dispersed Ti(III)–O–Si sites, supported by XPS (~6 % Ti(III)) and STEM–EDS. Reaction performance is governed by methanol management: two methanols are released, and their accumulation shifts the equilibrium backwards and promotes secondary alcoholysis to $M_2MP$, especially above 200 °C. DFT calculations support the experiments: dimerization of two MLA molecules has a moderate barrier ($\Delta G^{\neq}$ = 0.63 eV), whereas the ring-closing

step to LD is slower ($\Delta G^{\neq}$= 1.82 eV) and therefore controls the rate. The model also predicts the release of two methanol molecules; if they accumulate, they reverse the equilibrium. Continuous methanol removal and pore designs that allow fast product release should thus push the yield still higher.

In order to improve the performance of the catalysts, the influence of the valence and silica support of the catalysts was investigated more deeply by DFT calculations. The study examines the adsorption effects of titanium valence and catalyst support, comparing Ti(IV) catalysts (TiOH/$SiO_2$(IV), TiO/$SiO_2$(IV), and $TiO_2$(IV)) with Ti(III) catalysts (TiOH/$SiO_2$(III), Ti/$SiO_2$(III), and $TiO_2$-Ov(III)). Results reveal that Ti(III) in Titania-Silica catalysts exhibits superior adsorption capacity compared to Ti(IV), with Ti/SiO2(III) showing the highest adsorption energy of -1.69 eV. Charge density difference analysis demonstrates that $SiO_2$ support minimizes electron loss from Ti to deeper support layers. The adsorption mechanism on Ti/$SiO_2$(III) is found to be a synergistic effect of hydrogen bonding, Ti-O σ-bonding and π-backbonding. In contrast, $TiO_2$ and $TiO_2$-Ov catalysts show lower adsorption energies (< -0.77 eV), even with Ti(III) active sites, due to charge transfer extending to the subsurface. These findings highlight the potential of Ti/$SiO_2$(III) catalysts for the transesterification of MLA to LD, a crucial step in PLA recycling.

Techno-economic analysis of the closed-loop circular economy of PLA was carried out by constructing three complete sets of recycling flow diagrams in Aspen Plus software and benchmarking them under five operating scenarios to convert laboratory findings into industrial applications. Process 1 shows the conventional hydrolysis route (waste PLA → LA → two-step industrial LD synthesis), while Process 2 combines the direct alcoholysis route with a one-step gas-phase transesterification reaction (waste PLA

→ MLA → one-step industrial LD synthesis). Process 3 is based on Process 2 and optimises the alcoholysis process by recycling.

The results reveal that a novel recycling pathway using a $TiO_2/SiO_2$ catalyst (Process 3a) offers significant advantages over conventional industrial methods. This innovative approach achieves a remarkable 59.87% enhancement in PLA yield while simultaneously reducing process costs by 22.87%. Specifically, the annual PLA output increases from $5.96 \times 10^4$ tonnes to $9.04 \times 10^4$ tonnes, with production costs decreasing to US $1773/tonne. The superior performance of this recycling method is primarily attributed to the specific catalytic system employed, which plays a pivotal role in governing the activity and selectivity of the gas-phase transesterification of MLA into LD. Sensitivity analysis highlighted that catalyst loading, feed rate, and raw material pricing exert the strongest influence on unit cost, underscoring the importance of optimizing these parameters. This research not only presents a financially attractive and sustainable strategy for PLA value-added application but also directly addresses the need for environmentally technologies in the plastics industry. It emphasizes the central role of catalyst design in creating an efficient circular economy for PLA. This approach offers a promising pathway for the sustainable waste PLA management.

# 7.2 Limitations and Future Research Directions

Despite demonstrating a complete "molecule-to-system" workflow for closing the PLA loop, the study still rests on several simplifying assumptions and practical constraints. Recognising these limitations is essential for building the future work.

## 7.2.1 Reaction Set-up Constraints

The current set-up lacks two critical features that limit both performance and mechanistic insight. Firstly, even under a continuous $N_2$ flow, methanol is not quantitatively removed: each MLA → LD step releases two molecules of methanol that persist in the flask, hereby sustaining the reverse movement towards equilibrium. Moreover, methanol could drive the alcoholysis of MLA to by-products such as $M_2MP$. The selectivity of LD reported here is lower. To eliminate these bottlenecks, the next generation of experiments should incorporate an inert-gas sweep coupled to staged condensation. A low flow of nitrogen introduced above the liquid surface will carry volatile species out of the reactor. The vapour stream first encounters a 110–120 °C condenser, where MLA and LD are condensed, while methanol passes through to a second, ice-cooled condenser (0–5 °C) that traps it. Because the boiling point gap between methanol and the other species is still large in this temperature window, loss of product will be minimal.

Secondly, MLA is added by manual pipetting before the run begins. Viscous losses along the glassware walls, small weighing errors, and evaporation at 170–220 °C make the exact feed amount uncertain, complicating attempts to close material balances or compare runs quantitatively. Adding the reactants drop by drop will also increase the contact area of the reactants with the catalyst and improve the performance of the catalyst. In future, we will employ metered syringes to replace manual addition. These syringes deliver MLA at a constant rate and record the volume dispensed.

## 7.2.2 Catalyst Lifetime and Operation tests

The present study is based exclusively on $TiO_x/SiO_2$ catalyst in 0.5 h batch experiments conducted at 170–220 °C. Such short run tests are invaluable in quickly

screening catalytic activity, saving both feedstock and catalyst. However, it is this very high efficiency, which may stem from the very short test times, that also means that the true lifetime of the catalyst is still unknown. A half-hour run cannot capture the slow oxidation or coking processes that often emerge only after tens or hundreds of hours running. Moreover, because no recycle or regeneration cycles were attempted, we do not yet know whether the isolated Ti(III)–O–Si sites that drive high MLA conversion will persist, re-oxidise to Ti(IV), sintering or agglomerate into less active $TiO_2$ phase under repeated thermal swings. In the future, we plan operate the catalyst for over 100h with online GC monitoring conversion and selectivity and combine with X-ray absorption spectroscopy (XAS) traces the evolution of Ti(III) to Ti(IV) and possible coke deposition, sintering.

### 7.2.3 DFT Modelling Simplifications

To isolate the electronic role of titanium valence and the charge transfer effect of the silica support, the DFT work treated the catalyst as a single Ti atom loaded on the $SiO_2$ surface. This simplification makes the mechanism clearer but unavoidably deviates from the structural richness of the real material. The $TiO_x/SiO_2$ sample synthesised for this study shows no $TiO_2$ diffraction peaks in XRD, ruling out large crystalline domains, yet the data do not distinguish single atoms from nano clusters. STEM-EDS elemental mapping (~ 1 μm resolution) confirms a uniform Ti distribution but likewise cannot resolve atom-scale dispersion. Consequently, the computed adsorption energies and reaction barriers should be viewed as qualitative indicators rather than exact descriptors of the working catalyst. A more reliable model would load a $TiO_2$ or Ti cluster on silica, allowing explicit treatment of metal–metal interactions and coverage effect. Incorporating

such cluster ensembles into future DFT will narrow the gap between theory and experiment and sharpen catalyst design.